Universitat Politècnica de València
Departamento de Máquinas y Motores Térmicos

Experimental study of the effect of nozzle geometry on the performance of direct-injection diesel sprays for three different fuels

Doctoral Thesis
by:
Mr. Juan Pablo Viera Sotillo
Thesis supervisor:
PhD. Raul Payri Marin

Valencia, March 2017

DOCTORAL THESIS

EXPERIMENTAL STUDY OF THE EFFECT OF NOZZLE GEOMETRY ON THE PERFORMANCE OF DIRECT-INJECTION DIESEL SPRAYS FOR THREE DIFFERENT FUELS

By

JUAN PABLO VIERA SOTILLO

Submitted to the

DEPARTAMENTO DE MÁQUINAS Y MOTORES TÉRMICOS
UNIVERSITAT POLITÈCNICA DE VALÈNCIA

In partial fulfillment of the requirements for the degree of

DOCTOR OF PHILOSOFY

Valencia, March 2017

DOCTORAL THESIS

EXPERIMENTAL STUDY OF THE EFFECT OF NOZZLE GEOMETRY ON THE PERFORMANCE OF DIRECT-INJECTION DIESEL SPRAYS FOR THREE DIFFERENT FUELS

By:	Mr. Juan Pablo Viera Sotillo
Supervisor:	Dr. Raul Payri Marin

DOCTORAL EXAMINATION BOARD:

1. Dr. José María Desantes
2. Dr. Francisco Vicente Tinaut Fluixa
3. Dr. Francesco Concetto Pesce

DOCTORAL REVIEWING BOARD:

1. Dr. Ramachandra Diwakar
2. Dr. Christine Mounaïm-Rousselle
3. Dr. Francisco Vicente Tinaut Fluixa

Valencia, March 2017

Resumen

La clave para reducir la formación de contaminantes, emisiones y aumentar la eficiencia en los motores de inyección directa diésel radica en entender y tener la capacidad de predecir los procesos de inyección, mezcla, evaporación y combustión. Con este objetivo, los distintos grupos de investigación y desarrollo de motores han intentado, durante décadas, comprender y describir mejor los fundamentos de estos procesos, incluyendo combustibles alternativos y estrategias de combustión novedosas. Los chorros de inyección, caracterizados principalmente por fenómenos físicos complejos e intrínsicamente estocásticos, presentan un reto significativo para los investigadores de motores y combustión. De igual manera, el alcance completo del efecto de la geometría de la tobera sobre un espectro grande de condiciones de inyección (incluyendo distintos combustibles) y variables de respuesta, no está completamente definido, a pesar de haber sido estudiado anteriormente.

En esta tesis se estudia la influencia del flujo interno sobre un amplio espectro de condiciones y diagnósticos experimentales. Se realizaron experimentos para dos geometrías de tobera—toberas cilíndrica y cónica de un único orificio—y tres combustibles. Dos de los combustibles son puros—n-heptano y n-dodecano—mientras el tercero es un combustible sustituto que consiste en una mezcla de tres componentes que busca representar mejor las propiedades físicas y químicas del diesel. Las medidas incluyen una caracterización hidráulica completa, compuesta por tasa de inyección y cantidad de movimiento instantáneas; una visualización de alta velocidad del chorro líquido isotermo; una visualización de alta velocidad del chorro inerte evaporativo, con captura simultánea de las fases líquida y vapor y, finalmente, una visualización del chorro reactivo a alta temperatura, con captura de la fase vapor y la quimioluminiscencia del radical OH* para cada evento de inyección. Todos los diagnósticos en condiciones de alta temperatura fueron realizados en una maqueta de alta presión y temperatura de flujo constante que permite controlar con precisión un rango amplio de condiciones termodinámicas (hasta 1000 K y 15 MPa).

La tobera cilíndrica, con un diámetro de salida 8.6 % mayor que el de la cónica, presenta una penetración de chorro más lenta, a pesar de tener una tasa de inyección y flujo de cantidad de movimiento mayores en la parte estabilizada de la inyección. El ángulo del chorro mostró ser inversamente proporcional a la penetración. Este ángulo es principalmente determinado por la geometría de la tobera y la densidad del ambiente al que se inyecta. Por otro lado, tanto para el chorro isotermo como para el evaporativo inerte, los chorros producidos por la tobera cilíndrica presentan mayores fluctuaciones en el contorno detectado, lo cal, en el caso evaporativo, es cierto para las fases líquida y vapor.

En el caso del chorro isotermo, la presión en el raíl mostró tener una pequeña influencia en el ángulo de chorro cercano y una influencia despreciable en las fluctuaciones de dicho ángulo. El n-heptano mostró las penetraciones más lentas mientras que el n-dodecano y el combustible sustituto mostraton comportamientos similares para variaciones de presión de inyección y ambiente.

Para el chorro inerte evaporativo, la fase líquida fue detectada a través de una configuración óptica de iluminación trasera difusa pulsada, mientras que la fase vapor fue detectada con un arreglo óptico de Schlieren con diafragma. Para una densidad ambiente particular, la penetración de la fase líquida está controlada principalmente por la temperatura ambiente y las propiedades del combustible, mientras que la penetración de la fase vapor está controlada por la presión de inyección. La tobera cilíndrica consistentemente produjo longitudes líquidas más cortas. El n-heptano mostró las longitudes líquidas más cortas, seguido del n-dodecano y finalmente, el combustible sustituto. No se encontraron diferencias significativas en la penetración de vapor entre combustibles, a diferencia de lo visto para el chorro líquido isotermo. Los comportamientos encontrados para las longitudes líquidas presentan las respuestas esperadas frente a cambios paramétricos de la temperatura y densidad ambiente. Se presentaron dos modelos predictivos empíricos, que a su vez se utilizaron para analizar la influencia de las propiedades del combustible en la longitud líquida. La volatilidad del combustible mostró ser el factor primario que controla la longitud líquida entre los combustibles estudiados

Los chorros reactivos mostraron penetraciones más rápidas que los chorros inertes, debido a la aceleración inducida por la combustión después de la ignición. Un aumento en la concentración de oxígeno y en la temperatura ambiente aumenta la reactividad y por tanto acelera la penetración del chorro. La presión de inyección, al no afectar significativamente la reactividad, influye en la penetración únicamente modificando la cantidad de movimiento—similar al caso inerte. Tanto el retardo del auto-encendido como la longitud de levantamiento de llama son más cortas para el n-dodecano y más largas para el n-heptano, mientras los valores correspondientes al combustible sustituto se ubican en el medio de los anteriores. Un aumento en la concentración de oxígeno, temperatura o densidad ambiente, reducen tanto el retardo del auto-encendido como la longitud de levantamiento de llama. La tobera cilíndrica mostró aumentar el retardo del auto-encendido en comparación a la cónica, a pesar de producir longitudes de levantamiento de llama más cortas. Esto podría ser debido a su mayor ángulo de chorro. El mayor retardo del auto-encendido también indica posibles tasas de mezcla más pobres en el momento de la ignición.

Los resultados experimentales y la gran base de datos obtenida en este trabajo (disponible en: http://www.cmt.upv.es/DD01.aspx), podrían ser utilizados para validar modelos CFD detallados que podrían ayudar a la comunidad científica a entender mejor los mecanismos fundamentales que producen los resultados observados.

Resum

La clau per reduïr la formació de contaminants, emissions i augmentar l'eficiència en motors d'injecció directa dièsel està a entendre i tenir la capacitat de predir els processos d'injecció, mescla, evaporació i combustió. Amb aquest objectiu, els diferents grups d'investigació i desenvolupament de motors han tractat, per dècades, de comprendre i descriure millor els fonaments d'aquests processos, incloent combustibles alternatius i noves estratègies de combustió. Els dolls d'injecció, caracteritzats principalment per fenòmens físics complexos i intrínsicamente estocàstics, presenten un repte significatiu per als investigadors de motors i combustió. D'igual manera, l'abast complet de l'efecte de la geometría de la tovera sobre un espectre gran de condicions d'injecció (incloent diferents combustibles) i variables de resposta, no està completament definit, encara que haja sigut estudiat amb anterioritat.

Aquesta tesi estudia la influència del flux intern sobre un gran espectre de condicions i diagnòstics experimentals. Es van realitzar experiments per a dos geometries de tovera—toveres cil·líndrica i cónica amb un únic orifici—i tres combustibles. Dos dels combustibles són purs—n-heptà i n-dodecà— mentre el tercer combustible consisteix en una mescla de tres components que formen un combustible substitut que busca representar millor les propietats físiques i químiques del dièsel. Les mesures inclouen una caracterització hidràulica completa, composta per taxa d'injecció i quantitat de moviment instantanis; visualització d'alta velocitat del doll líquid isoterme; visualització d'alta velocitat del doll inert evaporatiu, capturant simultàniament les fases líquid i vapor i, finalment, una visualització del doll reactiu a alta temperatura, capturant la fase vapor i la quimioluminiscència del radical OH per a cada esdeveniment d'injecció. Tots els diagnòstics en condicions d'alta temperatura van ser realitzats en una instal·lació d'alta pressió i temperatura amb flux constant que permet controlar amb precisió un ampli rang de condicions termodinàmiques (fins a 1000 K i 15 MPa).

La tovera cil·líndrica, amb un diàmetre d'eixida un 8.6 % més gran que la cònica, presenta una penetració de doll més lenta, malgrat tenir una taxa d'injecció i un flux de quantitat de moviment majors en la part estabilitzada de la injecció. L'angle del doll va mostrar ser inversament proporcional a la penetració. Aquest angle és principalment determinat per la geometria de la tovera i la densitat ambient. D'altra banda, tant per al doll isoterm com per a l'evaporatiu inert, els dolls produïts per la tovera cil·líndrica presenten majors fluctuacions en el contorn detectat, el cas evaporativo incloent fases líquida i vapor.

En el cas del doll isoterm, la pressió al raïl va mostrar tenir una xicoteta influència en langle de doll proper i una influència menyspreable en les fluctuacions d'aquest angle. L'n-heptà mostrà les penetracions més lentes mentre que

el n-dodecà i el combustible substitut mostraren comportaments similars per a variacions de pressió d'injecció i ambient.

Per al doll inert evaporatiu, la fase líquida va ser detectada a través d'una configuració òptica d'il·luminació posterior difusa premuda, mentre que la fase vapor va ser detectada amb un arranjament òptic de Schlieren amb diafragma. Per a una densitat ambient particular, la penetració de la fase líquida està controlada principalment per la temperatura ambient i les propietats del combustible, mentre que la penetració de la fase vapor está controlada per la pressió d'injecció. La tovera cil·líndrica consistentment va produir longituds líquides més curtes. L'n-heptà va mostrar les longituds líquides més curtes, seguit del n-dodecà i, finalment, el combustible substitut. No es van trobar diferències significatives entre combustibles pel que fa a la penetració de vapor. Això no va ser l'oposat per al doll líquid isoterm. Les longituds líquides presenten les respostes esperades front a canvis paramètrics de temperatura i densitat ambient. Es van presentar dos models predictius empírics, que al seu torn es van utilitzar per tal d'analitzar la influència de les propietats del combustible en la longitud líquida. La volatilitat del combustible mostrà ser el factor primari que controla la longitud líquida entre els combustibles estudiats.

Els dolls reactius mostraren penetracions més ràpides que els dolls inerts, a causa de l'acceleració induïda per la combustió després de la ignició. Augmentar la concentració d'oxígen i la temperatura ambient augmenta la reactivitat i per tant accelera la penetració del doll. La pressió d'injecció no afecta la reactivitat significativament i per tant solamnet afecta la penetració a través de la quantitat de moviment—similar al cas inert. Tant el retard a l'autoencés com la longitud d'aixecament de flama són menors per a l'n-dodecà i majors per a l'n-heptà, quedant el combustible substitut en un punt intermedi. Augmentar la concentració d'oxígen, la temperatura o la densitat ambient redueix tant el retard a l'autoencés com la longitud d'aixecament de flama. La tovera cil·líndrica mostrà augmentar el retard a l'autoencés, malgrat produïr longituds d'aixecament de flama més curtes. Això podria deure's a la seu millor atomització i major angle de doll. El major retard a l'autoencés també indica possibles taxes de mescla més pobres al moment de la ignició.

Els resultats experimentals i la gran base de dades obtinguda en aquest treball (disponible a la web en: `http://www.cmt.upv.es/dd01.aspx`), podrien ser utilitzats per tal de validar models CFD detallats que podrien ajudar a la comunitat científica a entendre millor els mecanismes fonamentals que produeixen aquestes observacions.

Abstract

Understanding and properly predicting fuel injection, mixing, evaporation and combustion processes are the key to reducing pollutant formation and improve efficiency of direct injection diesel engines. To this end, engine research and development groups have been trying for decades to better comprehend and describe the fundamentals of these processes, including alternative fuels and combustion strategies. Fuel sprays, being primarily characterized by physically complex phenomena and intrinsically stochastic behavior, are remarkably challenging to engine and combustion researchers. Accordingly, even though it has been studied before, the full extent of the effect nozzle geometry over a wide span of operating conditions (including fuels) and response variables is not yet fully understood.

This thesis studies the influence of internal nozzle flow characteristics over a large spectrum of experimental conditions and diagnostics. Experiments were carried out for two nozzle geometries—cylindrical and conical single hole nozzles—and three different fuels. Two of the fuels are pure components—n-heptane and n-dodecane—while the third fuel consists of a three-component surrogate to better represent the physical and chemical properties of diesel fuel. Measurements include a complete hydraulic characterization consisting of instantaneous injection rate and spray momentum flux measurements; a high-speed visualization of isothermal liquid spray; a high-speed visualization of the evaporative inert spray, imaging liquid and vapor phases simultaneously and finally, a high-speed visualization of the high temperature reactive spray, imaging vapor phase and OH* chemiluminescence for each injection event. All high-temperature diagnostics were performed in a continuous flow test chamber that allows an accurate control on a wide range of thermodynamic conditions (up to 1000 K and 15 MPa).

The cylindrical nozzle with 8.6 % larger diameter, in spite of higher stabilized mass flow rate and momentum flux, shows slower spray tip penetration when compared to the conical nozzle, in all diagnostics. The spreading angle is found to be inversely proportional to the spray tip penetration. The spreading angle is largely influenced by the nozzle geometry and the ambient density. Also, for both the isothermal and evaporative inert spray, the spray produced by the cylindrical nozzle exhibits larger line-of-sight contour fluctuations, including liquid and vapor phases in the evaporative case.

For the isothermal spray, rail pressure was found to have weak influence on the near-field spreading angle and no influence on the standard deviation of the spreading angle. n-Heptane spray shows slowest penetration rates while n-dodecane and the surrogate fuel mixture show very similar spray behavior for variations in injection pressure and back pressure.

In the evaporative inert spray, the liquid phase is captured by a fast-pulsed diffused back illumination setup, while the vapor phase is captured by a single-pass Schlieren setup with diaphragm. For a fixed ambient density, the liquid penetration is controlled by ambient temperature and fuel characteristics while the vapor penetration rate is controlled by injection pressure. The cylindrical nozzle consistently produced shorter liquid lengths. n-Heptane spray shows the shortest liquid lengths, followed by n-dodecane and finally the Surrogate. No significant difference in vapor penetration rates was found between fuels, confirming that the vapor spray is controlled by momentum, which is independent of fuel. This was not the case for the non-evaporative isothermal sprays. Liquid lengths show the expected responses to parametric variations of ambient temperature and density. Two empirical predictive models are presented and utilized to analyze the influence of fuel properties on the liquid length. The primary factor controlling the liquid length between fuels is found to be their volatility.

The reactive spray is found to penetrate faster than non-reacting spray due to combustion induced acceleration after ignition. Higher oxygen concentration, and ambient temperature enhance the reactivity leading to higher spray tip penetration. Injection pressure does not affect the reactivity significantly and hence, influences spray penetration through momentum—similar to a non-reacting spray. Both ignition delay and lift-off length are found to be shortest and longest for n-dodecane and n-heptane, respectively, while the surrogate fuel falls in-between the two pure component fuels. Both ignition delay and lift-off length are found to decrease with an increase in oxygen concentration, ambient temperature, and density. The cylindrical nozzle, in spite of shorter lift-off length is found to have longer ignition delay, when compared to the conical nozzle. This could be due to better atomization leading to larger spread angle and evaporative cooling from the cylindrical nozzle compared to a conical nozzle. The longer ignition delay also leads to leaner equivalence ratios at the time of ignition.

The experimental findings from this work, and the large database obtained (available for download at: `http://www.cmt.upv.es/DD01.aspx`), could be used to validate CFD models that could help the community understand the fundamental driving mechanisms behind these observations.

To my parents.

There are no words to describe my gratitude to all people that helped me get here in any way. First of all, I thank Raul for being a great tutor and mentor, for trusting me to be his student, bringing out the best in me through these years, and for always driving all of us to the limit at the injection research group. Especially for proving everyone, over and over, that limits are what you set them to be. I thank Jaime, who I admire and consider bright, so good at communicating and listening to ideas. I thank him for being so patient and open to all my questions and doubts. The amount of work he has done for the group into doing things properly in terms of test procedures and data processing is inmense; I have learned so much from him and without all his work, this thesis would not be even close to what it is and I have learned so much from him. I would also like to thank Javi, Joaquin, Pedro and the rest of the injection research group, for always being so open to questions, and positive to help out in any way. In this group I always felt at home, and always felt that I could count on anyone that could help me with something. I will really miss our Wednesday meetings and our "almuerzos" together. I cannot thank the injection team without thanking CMT Motores Térmicos as well, in particular Francisco Payri and José María Desantes for giving me the opportunity to be part of this amazing research group, and guiding us all to excellence.

Now we go down to the labs, where the fun stuff happens. Thanks to José Enrique, who I think is hilarious in his own unbearable—for many—way, but also very organized, detailed and nice to work with at the labs, thanks for all the help with the test rigs, my inventions, and for the great times at the labs. I definitely have to say huge thanks to Jose "El Turner", for helping me out so many times with little custom parts and things "for yesterday", but also for being a great friend and someone to hang out and joke around at the labs. Here I would also thank all my lab "panchos", Frenchy (Guillaume), Croissant (Wilfried), Adele, Mari Carmen, Rex, Sergio and Pedro, for so much help and for the good times hanging out too.

I feel really grateful to the fuel sprays team at Argonne National Laboratory, Chris, Alan, Daniel and Andrew, such a great group of people who welcomed me during my thesis part appointment there, were so patient explaining everything and trusted me with the experiments. It was a great and enlightening experience that I will never forget.

Regarding my friends at CMT, I definitely thank Michele, for teaching me so much when I arrived and all through his days at CMT, but also being such a good friend and colleague to hang around with, as is Leo my south american panita. Oscar and Gaby for being great friends and also such good examples of dedication and effort. Dani, a great and funny friend who, to this day, keeps helping me a lot with my thesis. Guillermo, for helping me out with the characterization of fuels and being great to hang out with. I greatly thank Marcos, my twin student at injection, for

all his help every time I needed it, for the good times, and also being a great model of dedication and hard work. Thanks to the whole injection crew not mentioned so far: Sebas, Mary, Jesús, Santiago, David and Omar for all the "almuerzos" and the good times. Thanks to Abian, Armando and Mario for taking the time to review this thesis. I cannot conclude this part without especially thanking Dani and Manu, who were the ones constantly encouraging me to come to study my PhD. at CMT.

I thank my family, for always supporting me and just being awesome. Finally, I thank Jeanik for all her love and for coping with my dedication and commitment through the hardest years of my PhD. story, and for accompanying me along this path.

Contents

List of Figures

List of Tables

Nomenclature

Acronyms

CFD	Computational fluid dynamics
DBI	Diffused back illumination
ECN	Engine Combustion Network
FOV	Field of view
ICCD	Intensified Charge Coupled Device
ID	Ignition delay
LED	Light-emitting diode
LOL	Lift-off length
PAH	Polycyclic aromatic hydrocarbon
RMSE	Root-mean-square error
SoCF	Start of cool flames
SOE	Start of energizing
SOI	Start of injection
SSI	Second stage ignition

Greek

μ_f	Fuel dynamic viscocity
ρ	Ambient density
ρ_f	Fuel density
σ	Standard deviation
τ	Optical thickness

θ	Vapor spray spreading angle

Latin

A	Density ratio
B	Specific energy ratio
C_a	Area coefficient
$C_{p,liq}$	Liquid phase constant pressure specific heat capacity
d_o	Orifice nominal diameter
d_{eff}	Orifice effective diameter
h_{vap}	Specific enthalpy of vaporization
I	Pixel intensity
k	Proportioning constant
P_b	Back pressure
P_r	Rail pressure
T_a	Ambient temperature
T_b	Boiling temperature
T_f	Fuel temperature at the orifice
T_{90}	Temperature at 90 % evaporation
x_{liq}	Predicted liquid length
Y	Mass fraction
$k0$	Cylindrical nozzle
$k15$	Conical nozzle

Chapter 1

Introduction

This chapter introduces the motivation for studying the effect of nozzle geometry over the complete spectrum of direct-injection spray performance. First, the context where this thesis contributes to the community is described. Following, the purpose and significance that this study attempts to reach are exposed. Then, a summary of the subsequent chapters of this thesis is portrayed.

1.1 Background and context

Internal combustion engines have defined and shaped the world since their introduction approximately a century ago. Over the last three decades, performance, fuel consumption and exhaust emissions have been significantly improved. Nonetheless, increasing concerns in pollutant emissions demand a critical and detailed evaluation of the combustion process, which is largely influenced by fuel-air mixing [1–5].

Fuel sprays, being primarily characterized by physically complex phenomena and intrinsically stochastic behavior, are remarkably challenging to comprehend by engine and combustion researchers. Over the last three decades, experimental researchers have studied fuel sprays thoroughly in search for a better understanding of these phenomena and also for supporting data that enables validation of detailed numerical models [6]. To this end, computational fluid dynamics (CFD) models offer unmatched advantages over experimental approaches due to the large amount of temporal and spatial information they are able to provide. The predictive capability of validated CFD models can cut final product costs and times dramatically. Nevertheless, current state-of-the-art models still require high-fidelity experimental data for validation and accurate bounding of the problem.

Among all challenges presented by the physics of fuel sprays injected in-cylinder, the effect of nozzle geometry on the formation, mixing and combustion of the diesel spray is still of interest to the research community and the automotive industry [7–9]. Even though it has been studied before, the full extent of the nozzle geometry effects over a wide span of operating conditions (including fuels) and response variables is not yet fully understood. The majority of current spray models employ initial and boundary conditions at the nozzle exit as an indirect coupling to the flow inside the nozzle [10–13]. Such methods often dampen or lead to loss of smaller scale nozzle flow characteristics. Hence, the computed spray development using the indirect coupling is mainly dictated by momentum, aerodynamics, and mixing. In support of such methods, BADOCK et al. [14] and later GANIPPA et al. [15] presented results claiming that nozzle flow characteristics have negligible influence over the spray formation and that momentum is the only controlling variable for mixing. Contrasting these studies, several authors show that the flow inside the nozzle influences the near-nozzle region of the spray in terms of liquid-phase break-up, liquid length, and spray angle [16–24]. Many other studies also evidence the effects of nozzle flow characteristics over the macroscopic spray [10, 11, 13, 18, 25–28]. This contrast, along with the remaining uncertainty on the effect of nozzle geometry on entrainment, combustion, and pollutant formation, leave room for fundamental questions on the subject.

These fundamental questions could be addressed from the information provided by computational fluid dynamic (CFD) models, which output a large amount of temporal and spatial data that the experimental approach is unable to acquire [6]. Recently, a few authors have published computational models that employ a full grid comprising the nozzle internal geometry and the spray [29–34]. It is important to point out that the work presented by DESANTES et al. [29] and DESANTES et al. [34] and XUE et al. [32, 33] have been benefited significantly by the considerable size and good quality of the Engine Combustion Network (ECN) open database and efforts (`http://www.sandia.gov/ecn/`, [35]), which allowed access to very high resolution tomographies of the internal nozzle geometry, along with extensive experimental data from different institutions around the world. However, the effects of nozzle geometries on spray formation, and to some extent, fuel properties, were still out of the scope of these studies and so these publications do not answer the questions raised about the effects of nozzle flow and fuel characteristics over the macroscopic spray. These type of models could provide significantly more detail to the mechanisms and physics that control the relationship between nozzle flow, cavitation, and spray development, but they still need large amounts of experimental data for validation and bounding of the problem.

Fully predictive CFD models demand minimal uncertainties in physical and chemical fuel properties. The development of surrogate fuels is one way to achieve this while providing detailed chemical kinetic mechanisms [36–38] further reduced to computable sizes [37, 39] that can be employed in a fully reactive spray model. Surrogate fuels are often carefully tailored to mimic the behavior of real diesel fuel over the diagnostic being performed [37, 40, 41]. For some years, the surrogate of choice for diesel fuel has been a single-component species n-heptane. More than a hundred studies of diesel combustion have used n-heptane as a convenient surrogate. There have been two important reasons for this choice. First, n-heptane has a Cetane number of 56 that is reasonably close to the Cetane number of common diesel fuel, so its ignition is similar to that of diesel fuel which is suitable for ignition or heat release studies [11, 36, 39, 42, 43]. Second, a detailed kinetic reaction mechanism for n-heptane was published by CURRAN et al. [36] in 1998 with all of the detail required to carry out thorough combustion studies. Recently, it has become apparent that n-heptane is not sufficient as a diesel surrogate, for instance, IDICHERIA and PICKETT [44] showed that the n-heptane flame produces considerably less soot than a #2 diesel flame at similar conditions, and the soot distribution within the flame was also found to be quite different. Therefore, richer surrogates containing aromatics and other species that are important components in diesel fuels must also be represented in the surrogate selected for this study.

Different fuels will present different behaviors regarding nozzle flow characteristics. SOM et al. [45] studied the effects of fuel properties on cavitation characteristics and nozzle-outlet turbulence kinetic energy, similar to the experimental micro-visualization work presented by PAYRI et al. [46] and later JIANG et al. [47]. However, neither of these studies show the influences that different cavitation regimes found for each fuel may have on spray formation. CHEN et al. [48] presented a study analyzing the effects of diesel and four alternate fuels on droplet diameters, spray penetration and cone angle. Nonetheless, the effects of cavitation and nozzle flow characteristics are not contrasted with fuels in the paper. On this context, although the link between nozzle flow characteristics and macroscopic spray formation has been partially studied—especially linking the effects of nozzle geometry and cavitation to the spray formation—little to no information is found in the literature regarding the effects of fuel properties on nozzle flow and the corresponding macroscopic spray development, especially combining these with cavitating regimes.

This study is a contribution to the current understanding of the effects of nozzle flow characteristics over the macroscopic spray development, considering a wide span of experimental conditions and different fuels.

1.2 Objectives of the thesis

The present thesis was born from a research project in collaboration with General Motors R&D, specifically the Diesel Engine Systems Group at the Propulsion Systems Research Laboratory. The project was based on the acquisition of experimental spray data of different nozzles and fuels, with the purpose of CFD model validation. CMT Motores Térmicos added an additional fuel and more experimental conditions, widening the span of the analysis performed and the size of the data gathered, giving birth to this thesis.

The effect of nozzle geometry over the complete diesel spray development is not yet completely understood and additional studies are still presently carried out on the subject [49, 50]. It has been long known that cylindrical nozzle geometries produce a very steep pressure drop inside the nozzle, which causes cavitation given the conditions, and in more extreme cases, a collapse of the mass flow rate is observed [49, 51]. Conical or convergent nozzle geometries produce smooth pressure gradients that inhibits cavitation, this allows for smaller orifices to reach higher mass flow rates at these extreme conditions, while at the same time producing a thinner and easier to break-up liquid core. For this reason, conical nozzles have become widely popular in the industry. Nevertheless, recent studies have identified vibrations derived from cavitation as the main inhibitors of the coking process (the formation of carbon derived particles within the nozzle orifice) [52, 53]. Moreover, the increasing computational capacity and therefore, the detail and quality of CFD models, has brought back a lot of interest in this topic, since properly calibrated CFD models provide a lot of detailed information on the physics and events that link internal nozzle flow with spray development. On this context and considering what was previously stated in section 1.1 of this chapter, this thesis follows two main objectives:

- To contribute to the current understanding of the effects of nozzle geometry over the direct injection diesel spray development considering different fuels, by collecting and performing extensive data and experimental analyses, respectively.
- To acquire experimental data using state-of-the-art equipment and experimental techniques, in order to gather a large database with the purpose of publishing it online for the scientific community.

Note that both objectives are very much in line with the main guidelines of the ECN, contributing to the community with quality data that serves for direct analysis but also provides support for model validation. However, by the time this project was planned and the experiments were performed, different fuels and nozzle geometries were still out of the scope of the ECN.

Taking advantage from the technology, equipment and facilities available at CMT Motores Térmicos, different aspects of the injection process were thoroughly studied. In particular, the experiments performed can be divided in four main groups basing on their specific target:

- Hydraulic characterization of the fuel flow inside the nozzles.
- Isothermal liquid spray characterization.
- Evaporative inert spray characterization, considering both liquid and vapor phases.
- Reactive spray characterization, considering ignition and combustion.

All experiments were performed for two different nozzle geometries and three fuels. Two of the fuels are pure components—n-heptane and n-dodecane—while the third fuel consists of a three-component surrogate to better represent the physical and chemical properties of diesel fuel. The experimental campaign consisted in a complete hydraulic characterization—instantaneous injection rate and spray momentum flux measurements—followed by a high-speed visualization of the isothermal liquid spray, through a diffuse back-illumination technique that employs a fast pulsed light source. After, the evaporative spray was studied by simultaneous imaging of the liquid and vapor phases in high temperature and high density conditions, through two separate optical setups synchronized to capture the same injection event. Finally, combustion performance is assessed by studying ignition performance and lift off length of reactive sprays in high temperature and high density conditions with varying oxygen concentration. State-of-the-art experimental techniques, facilities and equipment were employed in order to ensure highest quality of data acquired and reported. It is important to remark that all experimental data presented in this study are available for download at `http://www.cmt.upv.es/DD01.aspx`.

1.3 About this thesis

With the objective of guaranteeing the correct comprehension of the work developed, methodology used, results, analysis, and conclusions, this thesis has been divided in 7 different chapters.

In the present chapter, **Chapter 1**, a brief description of the background and context of this work is presented. Several studies and scientific conclusions that give way to this work are discussed, along with the ever-growing numerical modeling capacity, which also relies in high quality experimental data for validation. The objectives and aims of this work are also described here.

In **Chapter 2**, the experimental tools, equipment and facilities are expounded. The nozzle geometries considered are presented and specified, along with the three fuels of interest to this work. Fuel properties relevant to this study are also given.

Through **Chapter 3**, the hydraulic characterization results are presented and discussed. Fuel rate of injection and momentum flux measurements are reported both in their time-resolved signal form but also as their steady-state values, for easier comparison of all experimental conditions. The results and conclusions from this chapter are also published in a journal paper titled “The effect of nozzle geometry over internal flow and spray formation for three different fuels” [54].

Chapter 4 presents and discuss results from the isothermal liquid spray visualization experiments. The experimental hardware, optical setup and technique, image processing algorithm, data averaging technique and test plan are described. Results are given in terms of spray tip penetration, near field spreading angle, and contour fluctuation maps. A specific analysis of the results obtained for the n-dodecane sprays was first published in a journal paper titled “Experimental analysis on the influence of nozzle geometry over the dispersion of liquid n-dodecane sprays” [55]. Later, full results and a wider analysis of the data in this chapter was also published in the same journal paper previously cited for the hydraulic results [54].

Chapter 5 discusses results from the evaporative inert spray visualization experiments. The experimental hardware, optical setup and technique, image processing algorithm, data averaging technique and test plan are also detailed. A full description of the evaporative spray development is given with the support of images containing simultaneous contours detected for the vapor and liquid sprays. Results are presented in terms of spray tip penetration, spreading angle, liquid length (both experimental and fitted models) and contour fluctuation maps. The results and conclusions presented in this chapter are also published in a journal paper titled “The effect of nozzle geometry over the evaporative spray formation for three different fuels” [56].

In **Chapter 6**, results from the reactive spray visualization are analyzed. The experimental hardware, optical setup and technique, image processing algorithm, data averaging technique and test plan are also described. A full description of the ignition process is given with the support of spray images containing contours detected for the vapor spray, showing the different stages of the ignition process. Results are presented in terms of spray tip penetration, lift-off length and ignition delays. The results and conclusions presented in this chapter are also published in a journal paper titled “The effect of nozzle geometry over ignition delay and flame lift-off of reacting direct-injection sprays for three different fuels” [57].

The conclusions extracted from the test results and the discussion sections are stated in **chapter 7**. In addition, proposed future work is laid out from the expertise and knowledge acquired during the development of this thesis.

References

[1] DIWAKAR, R. and SINGH, S. "NOx and soot reduction in diesel engine premixed charge compression ignition combustion: a computational investigation". *International Journal of Engine Research* 9.3 (2008), pp. 195–214.

[2] IDICHERIA, C. A. and DIWAKAR, R. "Design of an optimum combustion chamber across multiple speed/load points for a heavy-duty diesel engine: analytical design and experimental validation". *International Journal of Engine Research* 12.2 (2011), pp. 123–143.

[3] MAGNO, A., MANCARUSO, E., and VAGLIECO, B. M. "Experimental investigation in an optically accessible diesel engine of a fouled piezoelectric injector". *Energy* 64 (2014), pp. 842–852.

[4] DESANTES, J. M., GARCÍA-OLIVER, J. M., PASTOR, J. M., and RAMIREZ-HERNANDEZ, J. G. "Influence of nozzle geometry on ignition and combustion for high-speed direct injection diesel engines under cold start conditions". *Fuel* 90.11 (2011), pp. 3359–3368.

[5] HERFATMANESH, M. R., LU, P., ATTAR, M. A., and ZHAO, H. "Experimental investigation into the effects of two-stage injection on fuel injection quantity, combustion and emissions in a high-speed optical common rail diesel engine". *Fuel* 109 (2013), pp. 1–11.

[6] FANSLER, T. D. and PARRISH, S. E. "Spray measurement technology: a review". *Measurement Science and Technology* 26.1 (Jan. 2015), p. 012002.

[7] HUANG, S., DENG, P., HUANG, R., WANG, Z., MA, Y., and DAI, H. "Visualization research on spray atomization, evaporation and combustion processes of ethanol-diesel blend under LTC conditions". *Energy Conversion and Management* 106 (2015), pp. 911–920.

[8] YAO, C., GENG, P., YIN, Z., HU, J., CHEN, D., and JU, Y. "Impacts of nozzle geometry on spray combustion of high pressure common rail injectors in a constant volume combustion chamber". *Fuel* 179 (Sept. 2016), pp. 235–245.

[9] PAYRI, R., SALVADOR, F. J., GIMENO, J., and DE LA MORENA, J. "Effects of nozzle geometry on direct injection diesel engine combustion process". *Applied Thermal Engineering* 29.10 (2009), pp. 2051–2060.

[10] NING, W., REITZ, R. D., DIWAKAR, R., and LIPPERT, A. M. "A Numerical Investigation of Nozzle Geometry and Injection Condition Effects on Diesel Fuel Injector Flow Physics". *SAE Technical Paper 2008-01-0936* (2008).

[11] Som, S., Ramírez, A. I., Longman, D. E., and Aggarwal, S. K. "Effect of nozzle orifice geometry on spray, combustion, and emission characteristics under diesel engine conditions". *Fuel* 90.3 (2011), pp. 1267–1276.

[12] Battistoni, M., Grimaldi, C., and Mariani, F. "Coupled Simulation of Nozzle Flow and Spray Formation Using Diesel and Biodiesel for CI Engine Applications". *SAE Technical Paper 2012-01-1267* (2012).

[13] Montanaro, A., Migliaccio, M., Allocca, L., Fraioli, V., Lee, S.-y., Zhang, A., and Naber, J. "Schlieren and Mie Scattering Visualization for Single- Hole Diesel Injector under Vaporizing Conditions with Numerical Validation". *SAE Technical Paper 2014-01-1406* 2014-01-14 (2014).

[14] Badock, C., Wirth, R., and Tropea, C. "The influence of hydro grinding on cavitation inside a diesel injection nozzle and primary break-up under unsteady pressure conditions". *Proc. 15th ILASS-Europe 99, Toulouse, July 5-7*. Toulouse (France), 1999.

[15] Ganippa, L. C., Andersson, S., Chomiak, J., and Matsson, A. "Combustion characteristics of diesel sprays from equivalent nozzles with sharp and rounded inlet geometries". *Combustion Science and Technology* 175.6 (2003), pp. 1015–1032.

[16] Koo, J. Y., Hong, S. T., Shakal, J. S., and Goto, S. "Influence of fuel injector nozzle geometry on internal and external flow characteristics". *SAE Technical Paper 970354* (1997).

[17] Han, J.-s., Lu, P.-h., Xie, X.-b., Lai, M.-c., and Henein, N. A. "Investigation of Diesel Spray Primary Break-up and Development for Different Nozzle Geometries". *SAE Technical Paper* 2002-01-27 (2002).

[18] Blessing, M., König, G., Krüger, C., Michels, U., and Schwarz, V. "Analysis of flow and cavitation phenomena in diesel injection nozzles and its effects on spray and mixture formation". *SAE Technical Paper 2003-01-1358* (2003).

[19] Suh, H. K. and Lee, C. S. "Effect of cavitation in nozzle orifice on the Diesel fuel atomization characteristics". *International Journal of Heat and Fluid Flow* 29.4 (2008), pp. 1001–1009.

[20] Som, S., Ramírez, A. I., Aggarwal, S., Kastengren, A. L., El-Hannouny, E., Longman, D. E., Powell, C. F., and Senecal, P. K. "Development and validation of a primary breakup model for diesel engine applications". *SAE Technical Paper 2009-01-0838* (2009).

[21] SOM, S. and AGGARWAL, S. K. “Modeling Diesel Spray Flame Lift-off using Detailed Chemistry and a New Primary Breakup Model”. *47th AIAA Aerospace Sciences Meeting including The New Horizons Forum and Aerospace Exposition*. 2009, pp. 1–14.

[22] SOM, S. and AGGARWAL, S. K. “Effects of primary breakup modeling on spray and combustion characteristics of compression ignition engines”. *Combustion and Flame* 157.6 (2010), pp. 1179–1193.

[23] LIU, Z., IM, K.-S., WANG, Y., FEZZAA, K., WANG, J., XIE, X.-B., and LAI, M.-C. “Near-Nozzle Structure of Diesel Sprays Affected by Internal Geometry of Injector Nozzle: Visualized by Single-Shot X-ray Imaging”. *SAE Technical Paper 2010-01-0877* (2010).

[24] WANG, Y., QIU, L., REITZ, R. D., and DIWAKAR, R. “Simulating cavitating liquid jets using a compressible and equilibrium two-phase flow solver”. *International Journal of Multiphase Flow* 63 (2014), pp. 52–67.

[25] MORGAN, R., WRAY, J., KENNAIRD, D. A., CRUA, C., and HEIKAL, M. R. “The Influence of Injector Parameters on the Formation and break-Up of a Diesel Spray”. *SAE Technical Paper 2001-01-0529* (2001).

[26] PAYRI, F., BERMÚDEZ, V., PAYRI, R., and SALVADOR, F. J. “The influence of cavitation on the internal flow and the spray characteristics in diesel injection nozzles”. *Fuel* 83.4-5 (2004), pp. 419–431.

[27] PAYRI, R., SALVADOR, F. J., GIMENO, J., and ZAPATA, L. D. “Diesel nozzle geometry influence on spray liquid-phase fuel penetration in evaporative conditions”. *Fuel* 87.7 (2008), pp. 1165–1176.

[28] ZHANG, A., MONTANARO, A., ALLOCCA, L., NABER, J., and LEE, S.-Y. “Measurement of Diesel Spray Formation and Combustion upon Different Nozzle Geometry using Hybrid Imaging Technique”. *SAE Technical Paper 2014-01-1410* (2014).

[29] DESANTES, J. M. J. M., PAYRI, R., GIMENO, J., and MARTÍ-ALDARAVÍ, P. “Simulation of the First Millimeters of the Diesel Spray by an Eulerian Spray Atomization Model Applied on ECN Spray A Injector”. *SAE Technical Paper 2014-01-1418* (Apr. 2014).

[30] BATTISTONI, M., XUE, Q., SOM, S., and POMRANING, E. “Effect of Off-Axis Needle Motion on Internal Nozzle and Near Exit Flow in a Multi-Hole Diesel Injector”. *SAE International Journal of Fuels and Lubricants* 7.1 (Apr. 2014), pp. 2014–01–1426.

[31] SALVADOR, F. J., GIMENO, J., PASTOR, J. M., and MARTÍ-ALDARAVÍ, P. "Effect of turbulence model and inlet boundary condition on the diesel spray behavior simulated by an eulerian spray atomization (ESA) model". *International Journal of Multiphase Flow* 65 (2014), pp. 108–116.

[32] XUE, Q., SOM, S., BATTISTONI, M., QUAN, S., SENECAL, P. K., POMRANING, E., and SCHMIDT, D. P. "Eulerian CFD Modeling of Coupled Nozzle Flow and Spray with Validation Against X-Ray Radiography Data". *Int. J. of Engines* 7.2 (2014), pp. 1061–1072.

[33] XUE, Q., BATTISTONI, M., POWELL, C. F., LONGMAN, D. E., QUAN, S., POMRANING, E., SENECAL, P. K., SCHMIDT, D. P., and SOM, S. "An Eulerian CFD model and X-ray radiography for coupled nozzle flow and spray in internal combustion engines". *International Journal of Multiphase Flow* 70 (2015), pp. 77–88.

[34] DESANTES, J. M. et al. "Coupled/decoupled spray simulation comparison of the ECN spray a condition with the Σ-Y Eulerian atomization model". *International Journal of Multiphase Flow* 80 (2016), pp. 89–99.

[35] BARDI, M., PAYRI, R., MALBEC, L. M., BRUNEAUX, G., PICKETT, L. M., MANIN, J., BAZYN, T., and GENZALE, C. L. "Engine Combustion Network: Comparison of Spray Development, Vaporization, and Combustion in Different Combustion Vessels". *Atomization and Sprays* 22.10 (2012), pp. 807–842.

[36] CURRAN, H., GAFFURI, P., PITZ, W. J., and WESTBROOK, C. "A Comprehensive Modeling Study of n-Heptane Oxidation". *Combustion and Flame* 114.1-2 (1998), pp. 149–177.

[37] FARRELL, J. T., CERNANSKY, N. P., DRYER, F. L., LAW, C. K., FRIEND, D. G., HERGART, C. A., MCDAVID, R. M., PATEL, A. K., MUELLER, C. J., and PITSCH, H. "Development of an Experimental Database and Kinetic Models for Surrogate Diesel Fuels". *SAE Technical Paper 2007-01-0201* (Apr. 2007).

[38] BATTIN-LECLERC, F. "Detailed chemical kinetic models for the low-temperature combustion of hydrocarbons with application to gasoline and diesel fuel surrogates". *Progress in Energy and Combustion Science* 34 (2008), pp. 440–498.

[39] RAJU, M., WANG, M., SENECAL, P. K., SOM, S., and LONGMAN, D. E. "A reduced diesel surrogate mechanism for compression ignition engine applications". *Proceedings of the ASME 2012 Internal Combustion Engine Division Fall Technical Conference ICEF2012*. Vancouver: American Society of Mechanical Engineers, 2012.

[40] NATELSON, R. H., KURMAN, M. S., CERNANSKY, N. P., and MILLER, D. L. "Experimental investigation of surrogates for jet and diesel fuels". *Fuel* 87 (2008), pp. 2339–2342.

[41] PITZ, W. J. and MUELLER, C. J. "Recent progress in the development of diesel surrogate fuels". *Progress in Energy and Combustion Science* 37.3 (2011), pp. 330–350.

[42] PITSCH, H., BARTHS, H., and PETERS, N. "Three-dimensional Modeling of NOx and soot formation in DI-diesel engines using detailed chemistry based on the interactive flamelet approach". *SAE Technical Paper 962057* (1996).

[43] LUO, J., YAO, M., LIU, H., and YANG, B. "Experimental and numerical study on suitable diesel fuel surrogates in low temperature combustion conditions". *Fuel* 97 (2012), pp. 621–629.

[44] IDICHERIA, C. A. and PICKETT, L. M. "Soot formation in Diesel combustion under high-EGR conditions". *SAE Technical Paper 2005-01-3834* (2005).

[45] SOM, S., AGGARWAL, S. K., EL-HANNOUNY, E. M., and LONGMAN, D. E. "Investigation of nozzle flow and cavitation characteristics in a diesel injector". *Journal of Engineering for Gas Turbines and Power* 132.4 (2010), p. 042802.

[46] PAYRI, R., SALVADOR, F. J., GIMENO, J., and VENEGAS, O. "Study of cavitation phenomenon using different fuels in a transparent nozzle by hydraulic characterization and visualization". *Experimental Thermal and Fluid Science* 44 (2013), pp. 235–244.

[47] JIANG, G., ZHANG, Y., WEN, H., and XIAO, G. "Study of the generated density of cavitation inside diesel nozzle using different fuels and nozzles". *Energy Conversion and Management* 103 (2015), pp. 208–217.

[48] CHEN, P.-C., WANG, W.-C., ROBERTS, W. L., and FANG, T. "Spray and atomization of diesel fuel and its alternatives from a single-hole injector using a common rail fuel injection system". *Fuel* 103 (2013), pp. 850–861.

[49] QIU, T., SONG, X., LEI, Y., DAI, H., CAO, C., XU, H., and FENG, X. "Effect of back pressure on nozzle inner flow in fuel injector". *Fuel* 173 (2016), pp. 79–89.

[50] HE, Z., GUO, G., TAO, X., ZHONG, W., LENG, X., and WANG, Q. "Study of the effect of nozzle hole shape on internal flow and spray characteristics". *International Communications in Heat and Mass Transfer* 71 (2016), pp. 1–8.

[51] Payri, R., Garcia-Oliver, J. M., Salvador, F. J., and Gimeno, J. “Using spray momentum flux measurements to understand the influence of diesel nozzle geometry on spray characteristics”. *Fuel* 84.5 (2005), pp. 551–561.

[52] Argueyrolles, B., Dehoux, S., Gastaldi, P., Grosjean, L., Levy, F., Michel, A., and Passerel, D. “Influence of injector nozzle design and cavitation on coking phenomenon”. *SAE Technical Paper 2007-01-1896* (2007).

[53] Tang, J., Pischinger, S., Lamping, M., Körfer, T., Tatur, M., and Tomazic, D. “Coking Phenomena in Nozzle Orifices of Dl-Diesel Engines”. *SAE International Journal of Fuels and Lubricants* 2.1 (Apr. 2009), pp. 2009–01–0837.

[54] Payri, R., Viera, J. P., Gopalakrishnan, V., and Szymkowicz, P. G. “The effect of nozzle geometry over internal flow and spray formation for three different fuels”. *Fuel* 183 (Nov. 2016), pp. 20–33.

[55] Payri, R., Salvador, F. J., Gimeno, J., and Viera, J. P. “Experimental analysis on the influence of nozzle geometry over the dispersion of liquid n-dodecane sprays”. *Frontiers in Mechanical Engineering* 1 (2015), pp. 1–10.

[56] Payri, R., Viera, J. P., Gopalakrishnan, V., and Szymkowicz, P. G. “The effect of nozzle geometry over the evaporative spray formation for three different fuels”. *Fuel* 188 (2017), pp. 645–660.

[57] Payri, R., Viera, J. P., Gopalakrishnan, V., and Szymkowicz, P. G. “The effect of nozzle geometry over ignition delay and flame lift-off of reacting direct-injection sprays for three different fuels”. *Fuel* 199 (2017), pp. 76–90.

Chapter 2

Experimental tools

This chapter briefly expounds the relevant experimental tools and hardware utilized for the different studies carried out in this thesis.

2.1 The fuel injection system

A common-rail injection system consisting of a high pressure pump and a conventional rail with an electronic pressure regulator is used [1]. This system can generate relatively high rail pressures of up to 220 MPa and maintain it at the set value while injecting fuel. The injector body temperature is controlled using a special injector holder designed to have coolant flowing in direct contact with the injector body. The injector's return line is pressurized to 0.6 MPa as required by the injection system to work properly. The entire fuel injection system is electronically controlled and all the settings are introduced digitally.

2.2 Hydraulic characterization equipment

The injection rate measurements were carried out in a standard injection rate discharge curve indicator described in detail by PAYRI et al. [2], illustrated in Figure 2.1. In order to obtain a good estimation of the average behavior, fifty (50) consecutive injections were carried out at each test condition. The maximum dispersion was minimized to approximately 0.3 % after proper calibration of the equipment.

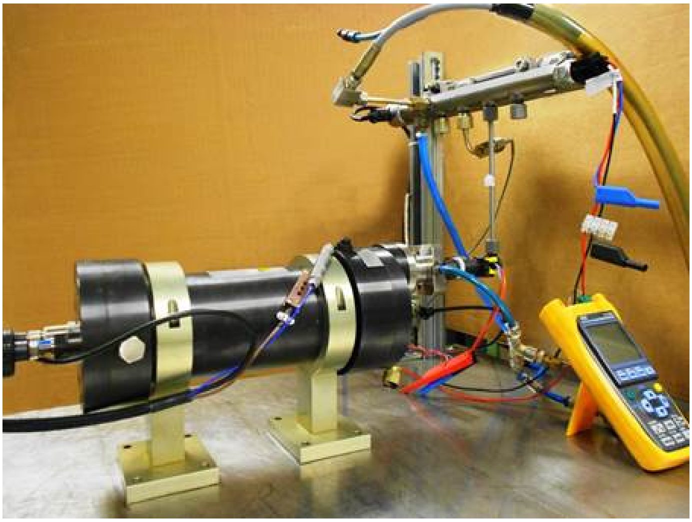

Figure 2.1: Photo of the injection rate discharge curve indicator utilized.

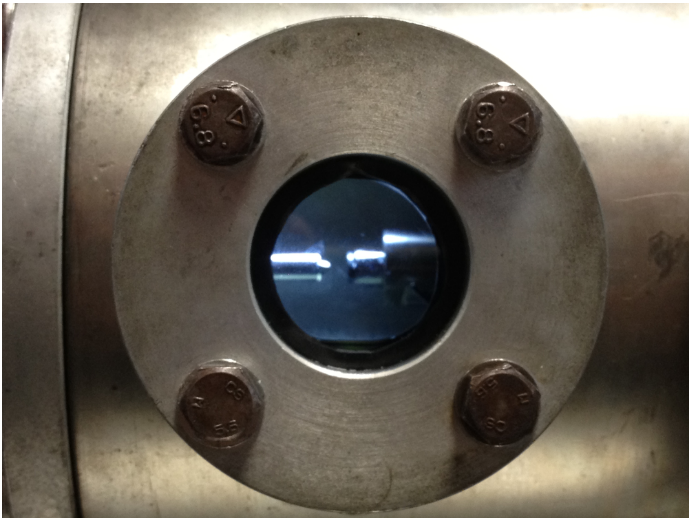

Figure 2.2: Photo of the injector (left) facing the piezoelectric pressure sensor (right) in the single-hole nozzle setup.

The spray momentum, on the other hand, is based on the measurement of the impingement force of a spray on a surface normal to the spray axis. This force represents the spray momentum flux which is measured using the test rig described in detail by Payri et al. [3]. In this test rig, the spray is injected into a chamber which can be pressurized with nitrogen up to 9.5 MPa in order to reproduce the pressure during the injection process inside the chamber. The impact force of the spray is measured with a piezoelectric pressure sensor previously calibrated and placed at 5 mm from the nozzle orifice exit. The location and frontal area of the sensor are carefully chosen to ensure full coverage, i.e., spray impingement area $\ll$ sensor area. Pressure inside the chamber is constant and fuel is assumed to deflect perpendicular to the spray axis after impingement. The force measured at the sensor is equal to the axial momentum flux at the orifice outlet or at any other axial location in the spray [3].

2.3 Isothermal spray visualization test rig

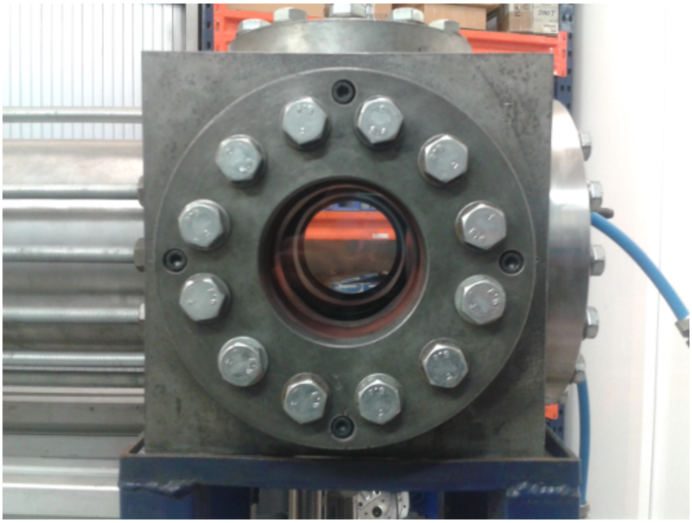

Figure 2.3: Photo of isothermal spray visualization test chamber.

The isothermal spray visualization test rig, shown in Figure 2.3, reproduces both the high gas pressure and density encountered in the diesel engine. It basically consists of a steel cube with a chamber and various connecting flanges machined into it. The design is modular, and ancillaries can be added depending on the required experiment [4]. The rig and ancillaries are designed for a maximum pressure of 90 bar. Continuous flow of nitrogen is maintained to evacuate injected diesel and keep window quality. The test rig operates in ambient temperature conditions thus avoiding fuel evaporation.

2.4 The high temperature and high pressure test rig

Figure 2.4: Photo of the high temperature and high pressure chamber.

High temperature visualization experiments were performed in a constant pressure-flow test chamber, shown in Figure 2.4, capable of mimicking the in-cylinder thermo-dynamic conditions of a diesel engine at the time of injection. This test rig features the unique capability of obtaining nearly quiescent and, compared to other facilities such as constant volume chambers [5], steady thermodynamic conditions within the chamber. This is particularly useful for extensive experimental campaigns with parametric variations of thermodynamic test conditions. The quiescent and steady conditions provide a high test repetition rate—also reducing the effective test time for a given set of test conditions—and enhance the shot-to-shot precision of the tests performed.

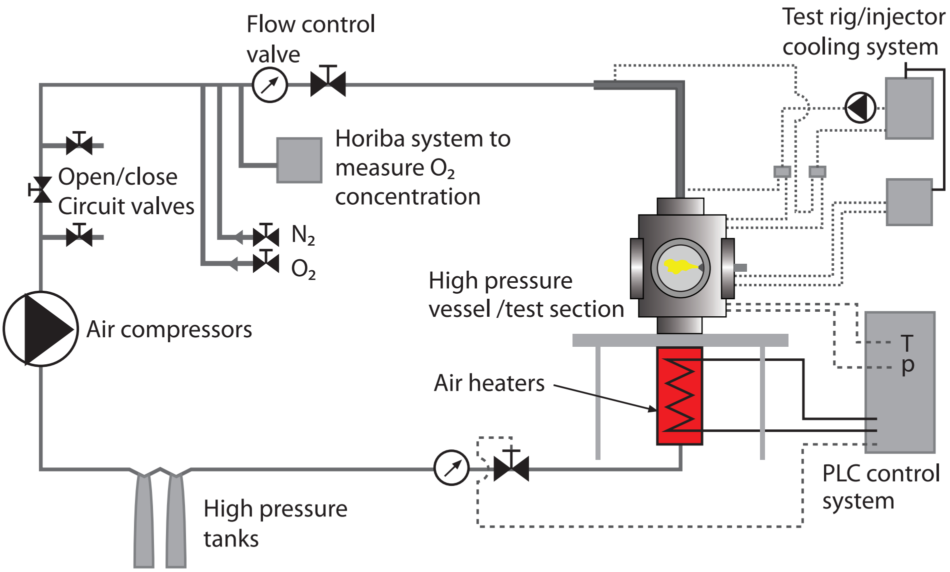

Figure 2.5: Schematic of the high temperature and high pressure installation.

Figure 2.5 provides a schematic of the installation. The high gas temperature is achieved from the heat exchange between the working gas and a set of electrical resistors located inside the inlet pipe that leads to the chamber. The installation is able to produce a maximum ambient temperature and pressure of 1000 K and 15 MPa respectively, in the test chamber. The chamber has three large optical accesses—128 mm in diameter—placed orthogonally in order to have complete optical access to the injection event. BARDI [6] described the test rig in detail in his PhD. dissertation.

2.5 Nozzles

All experiments are performed for two different nozzles, mounted on two independent injector bodies. Table 2.1 summarizes the injectors utilized and their nominal nozzle outlet diameters and geometries. Orifice outlet diameters were measured from the optical microscopy images depicted in Figure 2.6. The injectors are piezo-electrically actuated [7]. The two nozzles are micro-sac type single-hole nozzles, with different conicity (defined in terms of k-factor, as explained by PAYRI et al. [8]) but equal hydro grinding (13.5 % each) and nominal flow rate (124 cm^3/min/10 MPa each). Note that Table 2.1 includes reference

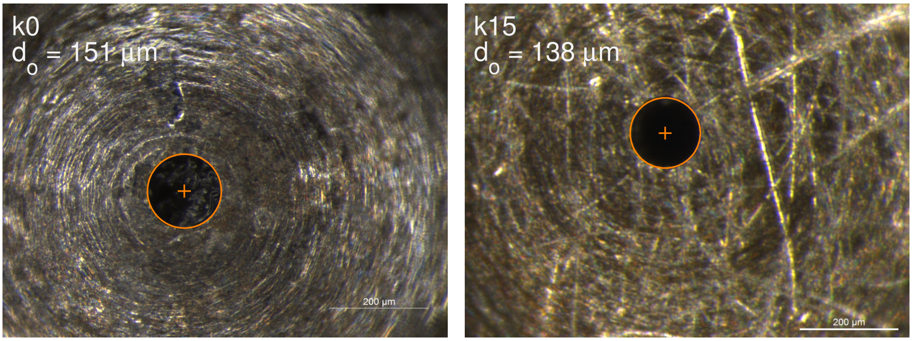

Figure 2.6: Optical microscopy images of the two nozzle outlet orifices.

symbol and color columns which indicate the symbols and/or colors that will be used to distinguish nozzles throughout the manuscript.

Table 2.1: Injector hardware utilized and nominal nozzle geometries.

Nozzle ref.	Nozz. type	d_o [μm]	k-factor	Ref. symbol	Ref. color
k0	micro-sac	151	0	◇	**purple**
k15	micro-sac	138	1.5	○	**green**

2.6 Fuels

All experiments were also performed for three different fuels. The first fuel selected was n-heptane. As stated in the Introduction section, n-heptane has long been utilized as a diesel surrogate to mimic diesel fuels in ignition and/or heat release studies [9–14]. The second fuel selected was n-dodecane, which features similar carbon content and boiling characteristics to those of diesel fuels, so it is expected to better mimic the mixing behavior of diesel fuels. This is one of the reasons n-dodecane was also selected as the primary fuel of study for the main ECN campaign [15], and it has been extensively characterized in the complete spectrum of experimental diagnostics and numerical simulations performed by the group. However, n-dodecane is not expected to be an adequate surrogate for ignition-related behavior, because of its Cetane number (approx. 88). Last, a multi-component diesel surrogate consisting of n-tetradecane (0.5), n-decane (0.25) and α-methylnaphthalene (0.25) was utilized. Numbers in parentheses represent mass fractions. This surrogate—from this point foward simply referred to as “Surrogate”—is expected to better mimic the soot-related behavior of real diesel fuel due to the PAH content and C/H ratio being closer to that of real diesel fuel. The short ignition delays expected due to the large n-tetradecane and n-decane contents (with Cetane numbers close to 96 and 77 respectively) are, at the same time, delayed by the the α-methylnaphthalene content. Fuel properties relevant to this study are summarized in Table 2.2.

Table 2.2: Fuels utilized and their properties at 298 K and 101 kPa. Except for the Surrogate fuel, all properties were extracted from the NIST Chemistry WebBook [16]. For the Surrogate fuel, density, viscosity and surface tension were measured as per ASTM D1298, ASTM D445 and UNE EN 14370 respectively.

Property	Units	n-Heptane	n-Dodecane	Surrogate
Density	kg/m^3	679.7	745.8	802.1
Viscosity	Pa s	5.59e-4	1.36e-3	1.61e-3
Surface tension	N/m	0.020	0.025	0.026
Boiling point	K	372	489	450 to 520
$C_{p,liq}$	J/kg/K	2234	2212	Tab. 2.3
h_{vap}	kJ/kg	359	358	Tab. 2.3
Ref. color	-	**cyan**	**blue**	**magenta**

Table 2.3: Components of the Surrogate fuel and their properties at 298 K and 101 kPa. All properties were extracted from the NIST Chemistry WebBook [16].

Property	Units	n-Tetradecane	n-Decane	α-methylnaphthalene
Boiling point	K	523	447	515
$C_{p,liq}$	J/kg/K	2208	2192	1578
h_{vap}	kJ/kg	361	361	415

The Surrogate distillation curve is presented in Figure 2.7. This Surrogate starts boiling near 450 K, the boiling point of n-decane. On the other hand, it is completely evaporated near 520 K, the boiling point of n-tetradecane, which comprises half of the mass of the Surrogate fuel. Note also that n-heptane features a boiling point considerably lower than the boiling range of the Surrogate, which at the same time includes the boiling point of n-dodecane. From these properties, it would be expected for n-heptane to feature much shorter liquid penetration lengths in comparison to the other two fuels, with the Surrogate fuel showing the longest values, as will be seen in chapter 5.

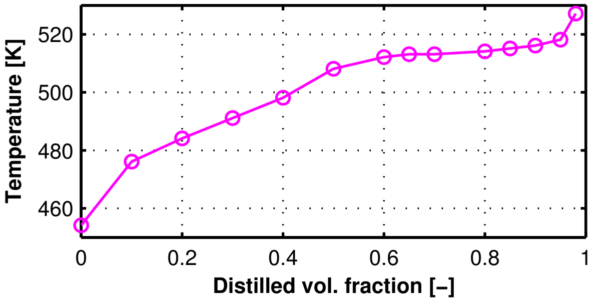

Figure 2.7: Distillation curve for the Surrogate fuel as per ASTM D86.

References

[1] STUMPP, G. and RICCO, M. "Common Rail - An attractive fuel injection system for passenger car DI Diesel engines". *SAE Technical Paper 960870* (1996).

[2] PAYRI, R., SALVADOR, F. J., GIMENO, J., and BRACHO, G. "A new methodology for correcting the signal cumulative phenomenon on injection rate measurements". *Experimental Techniques* 32.February (2008), pp. 46–49.

[3] PAYRI, R., GARCIA-OLIVER, J. M., SALVADOR, F. J., and GIMENO, J. "Using spray momentum flux measurements to understand the influence of diesel nozzle geometry on spray characteristics". *Fuel* 84.5 (2005), pp. 551–561.

[4] DESANTES, J. M., PAYRI, R., SALVADOR, F. J., and SOARE, V. "Study of the influence of geometrical and injection parameters on Diesel Sprays characteristics in isothermal conditions". *SAE Technical Paper 2005-01-0913* (2005).

[5] MEIJER, M. et al. "Engine Combustion Network (ECN): Characterization and comparison of boundary conditions for different combustion vessels". *Atomization and Sprays* 22.9 (2012), pp. 777–806.

[6] BARDI, M. "Partial needle lift and injection rate shape effect on the formation and combustion of the Diesel spray". PhD thesis. Valencia (Spain): Universitat Politècnica de València, Apr. 2014.

[7] SALVADOR, F. J., PLAZAS, A. H., GIMENO, J., and CARRERES, M. "Complete modelling of a piezo actuator last-generation injector for diesel injection systems". *International Journal of Engine Research* 15.1 (Jan. 2014), pp. 3–19.

[8] Payri, R., Salvador, F. J., Gimeno, J., and Zapata, L. D. “Diesel nozzle geometry influence on spray liquid-phase fuel penetration in evaporative conditions”. *Fuel* 87.7 (2008), pp. 1165–1176.

[9] Pitsch, H., Barths, H., and Peters, N. “Three-dimensional Modeling of NOx and soot formation in DI-diesel engines using detailed chemistry based on the interactive flamelet approach”. *SAE Technical Paper 962057* (1996).

[10] Curran, H., Gaffuri, P., Pitz, W. J., and Westbrook, C. “A Comprehensive Modeling Study of n-Heptane Oxidation”. *Combustion and Flame* 114.1-2 (1998), pp. 149–177.

[11] Raju, M., Wang, M., Senecal, P. K., Som, S., and Longman, D. E. “A reduced diesel surrogate mechanism for compression ignition engine applications”. *Proceedings of the ASME 2012 Internal Combustion Engine Division Fall Technical Conference ICEF2012*. Vancouver: American Society of Mechanical Engineers, 2012.

[12] Luo, J., Yao, M., Liu, H., and Yang, B. “Experimental and numerical study on suitable diesel fuel surrogates in low temperature combustion conditions”. *Fuel* 97 (2012), pp. 621–629.

[13] Tinaut, F. V., Giménez, B., Iglesias Hoyos, D., and Lawes, M. “Experimental determination of the burning velocity of mixtures of n-heptane and toluene in engine-like conditions”. *Flow, Turbulence and Combustion* 89.2 (2012), pp. 183–213.

[14] Reyes, M., Tinaut, F. V., Andrés, C., and Pérez, A. “A method to determine ignition delay times for Diesel surrogate fuels from combustion in a constant volume bomb: Inverse Livengood-Wu method”. *Fuel* 102 (2012), pp. 289–298.

[15] Bardi, M., Payri, R., Malbec, L. M., Bruneaux, G., Pickett, L. M., Manin, J., Bazyn, T., and Genzale, C. L. “Engine Combustion Network: Comparison of Spray Development, Vaporization, and Combustion in Different Combustion Vessels”. *Atomization and Sprays* 22.10 (2012), pp. 807–842.

[16] Lemmon, E. W., McLinden, M. O., and Friend, D. G. “Thermophysical Properties of Fluid Systems”. *NIST Chemistry WebBook, NIST Standard Reference Database Number 69*. Ed. by P. J. Linstrom and W. G. Mallard. 2011.

Chapter 3

Hydraulic characterization

One of the first steps towards characterizing a particular nozzle geometry in diesel injectors is to analyze its hydraulic performance. Rate of injection and momentum flux measurements are very important boundary conditions for CFD or 1D model development [1], but also provide valuable data for experimental analysis. The rate of injection—and its profile—are determinant to the combustion performance of a diesel engine [2]. PAYRI et al. [3] describe in detail the hydraulic characterization process. In this case, since the nozzles are single-hole axis-symmetric nozzles, the momentum flux test rig had to be set up for this particular application.

Note that during all tests described and presented in this chapter, energizing times and injector coolant temperature were fixed at 2500 μs and 343 K respectively. The injector body temperature was maintained close to target using a special injector holder designed to have coolant flowing at a controlled temperature in direct contact with the injector body [4].

3.1 Hydraulic characterization test plan

The experimental test plan was designed to evaluate the effect of different internal nozzle flow characteristics over the development of macroscopic spray. The different internal nozzle flow conditions are achieved by varying the rail pressure, chamber (back) pressures, and doing this for three fuels with different properties (Table 2.2). The complete test plan is displayed in Table 3.1. Note that each test point is done for all of the nozzles and fuels. Therefore, a total of **90** different test points were measured. All the experimental results presented in this manuscript are available for download at: `http://www.cmt.upv.es/DD01.aspx`.

Table 3.1: Hydraulic characterization test plan.

Parameter	Value-Type	Units
K-factor	0, 1.5	-
Back pressure (P_b)	3.0, 6.0, 9.0	MPa
Rail pressure (P_r)	30.0, 60.0, 90.0, 150.0, 200.0	MPa
Number of repetitions per test	50	-

3.2 Rate of injection

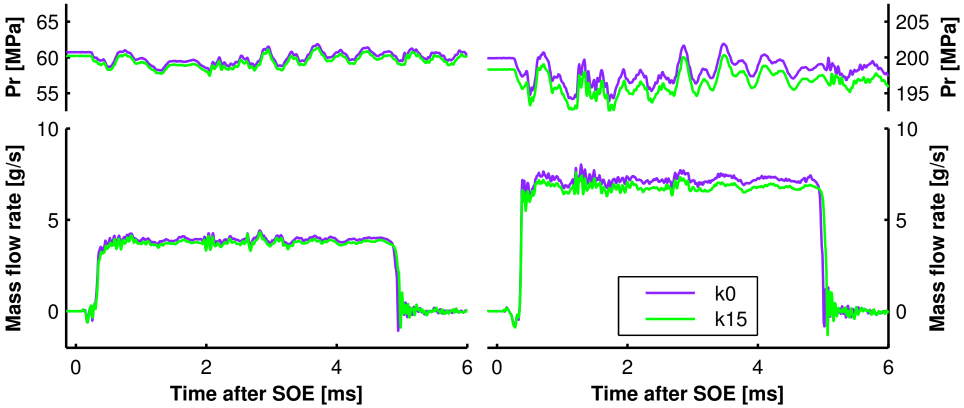

Figure 3.1: Rail pressure (top) and injection rate signals (bottom) measured for the two nozzles at rail pressures of 60.0 MPa (left) and 200.0 MPa (right). In this case, the injected fuel is n-dodecane and the back pressure is 6.0 MPa.

Figures 3.1 through 3.5 depict examples of rate of injection signals comparing nozzles and fuels respectively. The lowest and highest rail pressures are also shown in each case to illustrate its effect for all nozzles and fuels. The rates of injection measured present the expected responses to both rail and back pressure. Consistently throughout the test matrix, nozzle *k15* presented slightly lower stabilized mass flow rates, which is attributed to its smaller diameter. This is also summarized in Figure 3.11, where all test conditions are presented.

Figures 3.4 and 3.5 show a higher rate of injection for the Surrogate fuel, followed by n-dodecane and finally n-heptane. This order is consistent with the

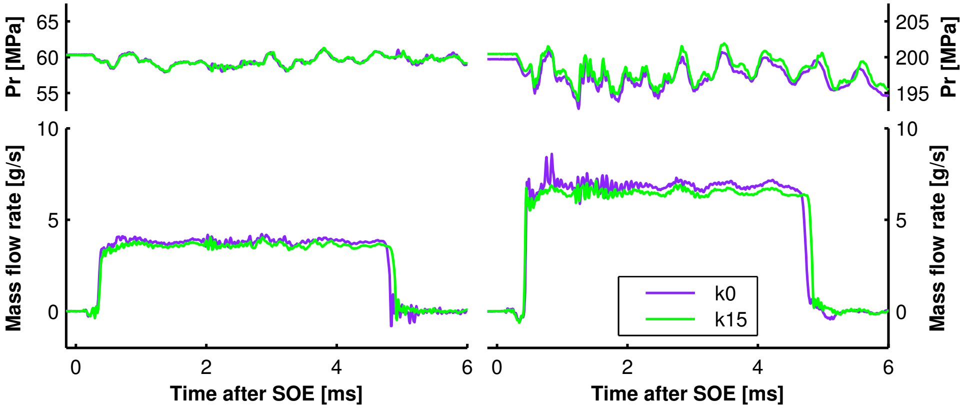

Figure 3.2: Rail pressure (top) and injection rate signals (bottom) measured for the two nozzles at rail pressures of 60.0 MPa (left) and 200.0 MPa (right). In this case, the injected fuel is n-heptane and the back pressure is 6.0 MPa.

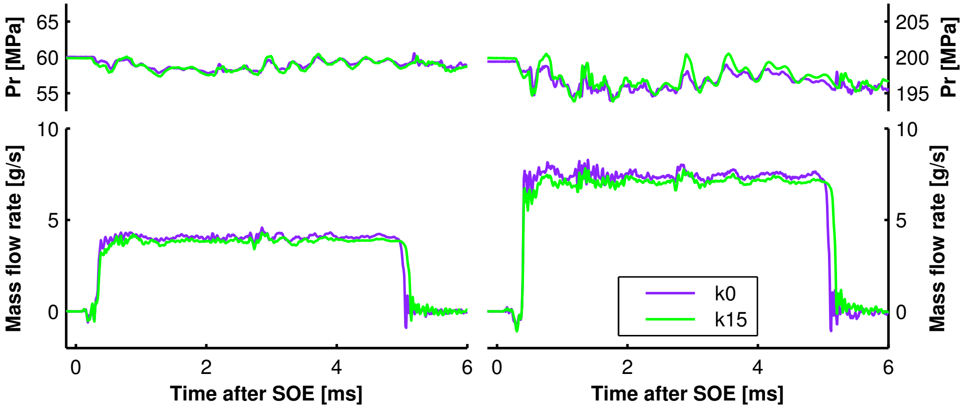

Figure 3.3: Rail pressure (top) and injection rate signals (bottom) measured for the two nozzles at rail pressures of 60.0 MPa (left) and 200.0 MPa (right). In this case, the injected fuel is the Surrogate and the back pressure is 6.0 MPa.

corresponding fuel densities, in agreement with results found in the literature [5–7]. Also, for the same energizing time, different fuels render different effective injection durations. If the energizing time is long enough, the needle lift reaches the mechanical limit which implies that the needle closing time is proportional to the viscosity of the fuel [8].

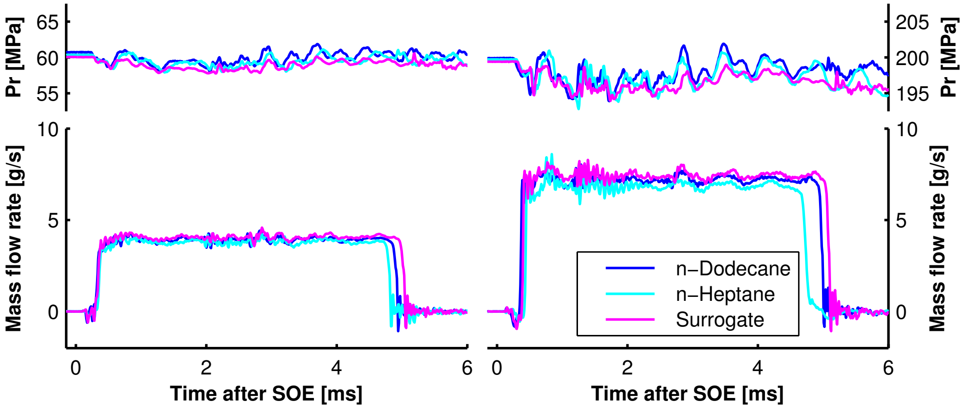

Figure 3.4: Rail pressure (top) and injection rate signals (bottom) measured for the three fuels at rail pressures of 60.0 MPa (left) and 200.0 MPa (right). In this case, the nozzle is k0 *and the back pressure is 6.0 MPa.*

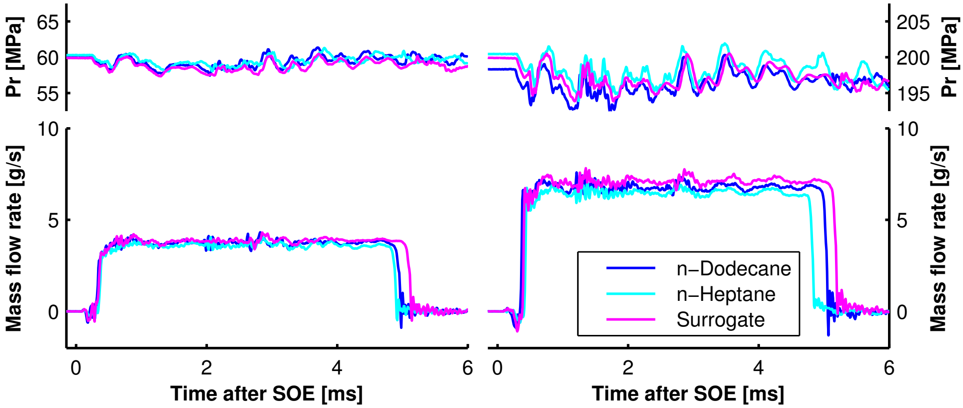

Figure 3.5: Rail pressure (top) and injection rate signals (bottom) measured for the three fuels at rail pressures of 60.0 MPa (left) and 200.0 MPa (right). In this case, the nozzle is k15 *and the back pressure is 6.0 MPa.*

3.3 Spray momentum

Analogous to the rate of injection results, Figures 3.6, 3.7 and 3.8 show that nozzle *k15* presents a lower momentum flux due to its smaller diameter, and this was observed throughout the complete test matrix, as depicted by Figure 3.12. Note how the difference between nozzles increases with rail pressure, since the contribution by the flow area is then amplified by the pressure delta. On the other

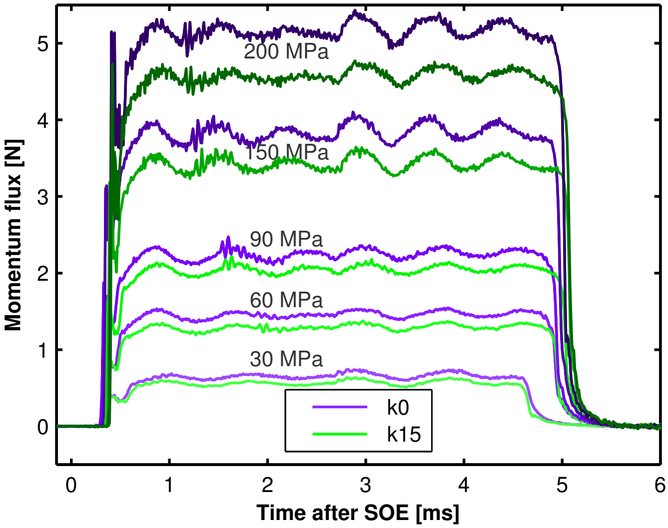

Figure 3.6: Momentum flux signals measured for the two nozzles at all rail pressures. In this case, the fuel is n-dodecane and the back pressure is 6.0 MPa.

.

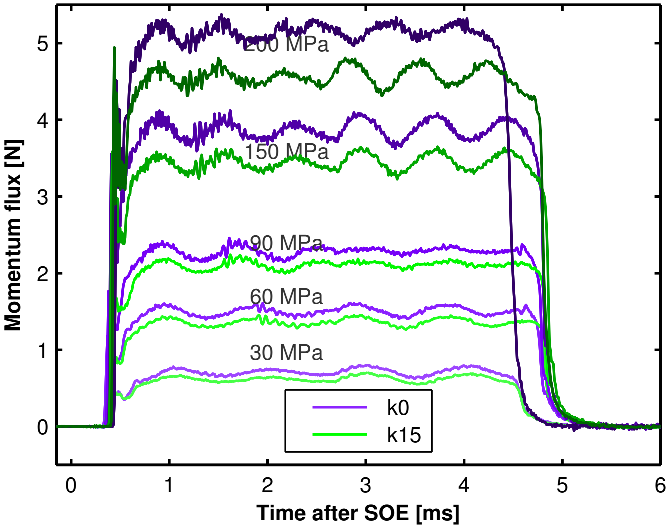

Figure 3.7: Momentum flux signals measured for the two nozzles at all rail pressures. In this case, the fuel is n-heptane and the back pressure is 6.0 MPa.

.

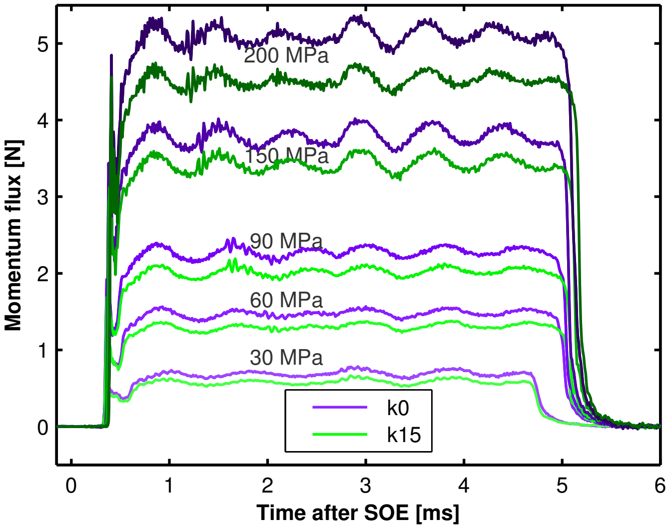

Figure 3.8: Momentum flux signals measured for the two nozzles at all rail pressures. In this case, the fuel is the Surrogate and the back pressure is 6.0 MPa.

.

hand, Figures 3.9 and 3.10 illustrate how the momentum flux is independent of the fuel utilized [5]. Moreover, note how the n-heptane injection is shorter overall, as explained before. In the case of 30 MPa of rail pressure the effective injection duration time is more similar between fuels, which could suggest that the needle is not reaching its mechanical lift limit in neither of these cases, so the effective injection duration is a combination of pressure differentials over the needle, fuel viscosity and fuel density [8].

3.4 Hydraulic analysis

From the signals presented in Figures 3.2 to 3.10, time-averages can be calculated from the stabilized table-top region of each signal. This way, results of the complete test matrix can be condensed into a single figure for particular analysis.

Figure 3.11-top shows stabilized mass flow rates as a function of the square root of the pressure drop through the nozzle. Note how values are ordered with fuel density, and how the conical nozzle *k15* stays lower in absolute mass flow rate values in comparison to the cylindrical nozzle *k0*, as explained in section 3.2. Note that sub-groups of points correspond to each of the rail pressures tested, and within a group, there are three back pressures distinguished by different shades of the corresponding color. Figure 3.11-bottom shows the discharge coefficients,

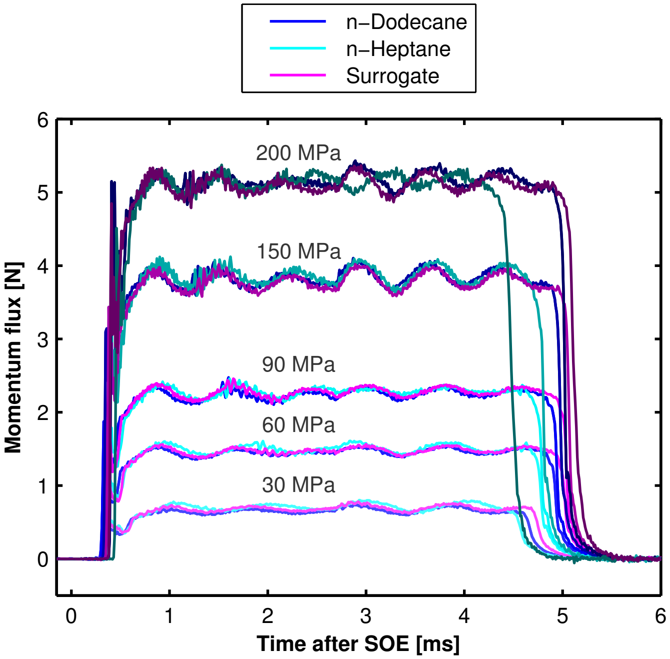

Figure 3.9: Momentum flux signals measured for the three fuels at all rail pressures. In this case, the nozzle is k0 *and the back pressure is 6.0 MPa.*

.

which are normalized by fuel density and nozzle diameter [3]. Here, the cylindrical nozzle shows a strong cavitating behavior, evidenced by the drastic reduction in the discharge coefficient, especially as the pressure difference is increased by reducing back pressure. Note that for high rail pressure cases the flow is completely collapsed for the cylindrical nozzle *k0* (i.e. all discharge coefficient points are grouped closely) while the low rail pressure cases show symptoms of flow collapse only when back pressure is decreased.

Figure 3.12 illustrates stabilized momentum flux measurements as a function of the pressure differential through the nozzle, comparing nozzles and fuels. As seen previously in Figure 3.10, momentum flux is generally independent of the fuel properties. As already commented in Figure 3.6, nozzle *k15* also shows lower momentum flux values due to its smaller diameter, and this difference increases with rail pressure.

Utilizing both the rate of injection and the momentum flux measurements, it is possible to estimate the effective flow velocity and area coefficient at the outlet orifice [3]. Figure 3.13-top shows the effective velocities estimated as a function of

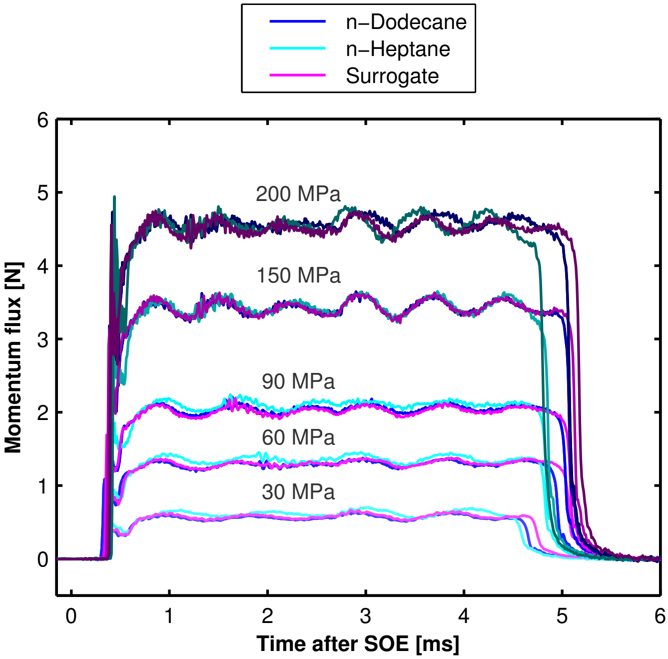

Figure 3.10: Momentum flux signals measured for the three fuels at all rail pressures. In this case, the nozzle is k15 *and the back pressure is 6.0 MPa.*

.

the square root of the pressure drop through the nozzle. Note how effective velocity values are ordered inversely with the fuel density, which is expected from the rate of injection and momentum flux results. Finally, Figure 3.13-bottom shows area coefficients, where the reduction in cross-section originated by cavitation is evidenced for the cylindrical nozzle *k0* [3, 6, 9].

3.5 Conclusions

A complete hydraulic characterization consisting of instantaneous injection rate and spray momentum flux measurements was carried out in combination with cylindrical and conical nozzle configurations [10]. Two of the fuels considered are pure components—n-heptane and n-dodecane—while the third fuel consists of a three-component Surrogate to better represent the physical and chemical properties of diesel fuel.

The fuel rate of injection was found to be strongly dependent on fuel density while the momentum flux is virtually independent of fuel properties, as expected

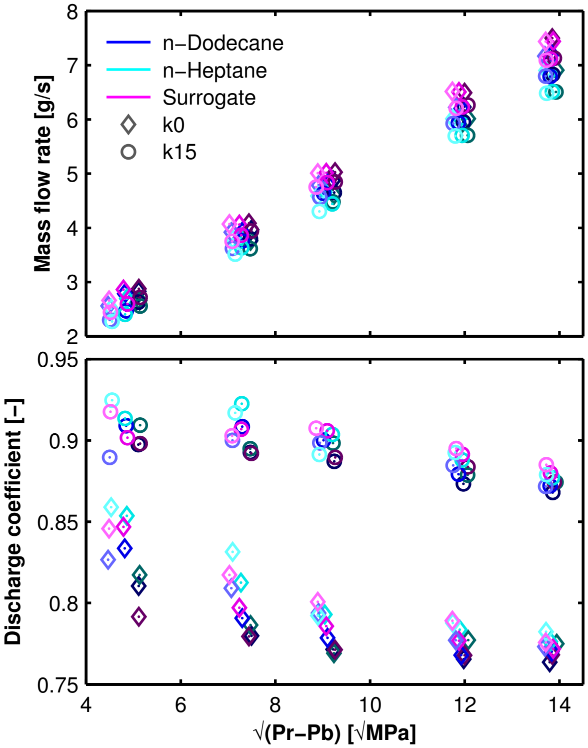

Figure 3.11: Steady rate of injection (top) and discharge coefficient (bottom) as a function of the pressure drop across the injector for all test conditions. Note that fuels are denoted by color while nozzles are indicated by symbols. Sub-groups of points correspond to each of the rail pressures tested, and within a group, there are three back pressures distinguished by different shades of the corresponding color.

from the literature. In general, the cylindrical nozzle *k0* with 8.6 % larger outlet diameter presents higher rate of injection and momentum flux in comparison to the conical nozzle *k15*, and differences between the two nozzles increase with rail pressure. The cylindrical nozzle *k0* presents a significant decrease in the discharge coefficient as injection pressure is increased and, especially, in combination with a decrease in the back pressure, also as expected from the literature. Cylindrical nozzles feature abrupt pressure drops as the fuel enters the nozzle, which incepts cavitation. Cavitation can extend to the point where the mass flow rate collapses which then is reported as a decrease in the discharge coefficient. The conical nozzle *k15*, on the other hand, presented the expected behavior, increasing mass flow rate with the pressure drop across the nozzle. Conical nozzle geometries feature smoother pressure gradients along the nozzle length which keep fuel from

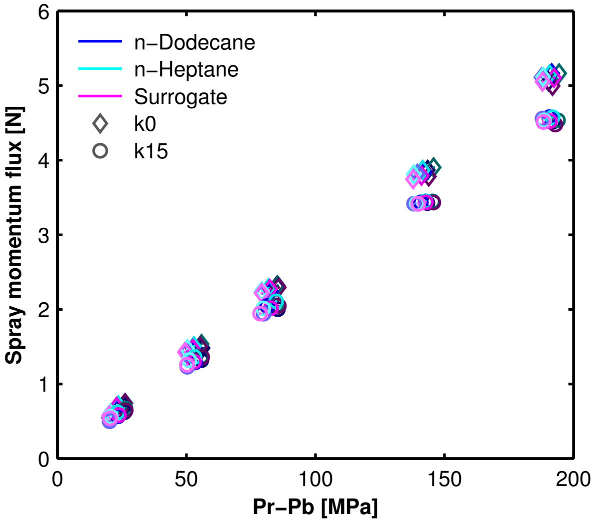

Figure 3.12: Steady momentum flux values as a function of the pressure drop across the injector for all test conditions. Note that fuels are denoted by color while nozzles are indicated by symbols.

cavitating. This allows smaller nozzle diameters to reach larger mass flow rates, which enhances atomization and shear.

The experimental findings from this hydraulic characterization, and the large database obtained (available for download at: `http://www.cmt.upv.es/DD01.aspx`), could be used to validate CFD models that could then be expanded to spray models, invaluable for further understanding of the effects of nozzle geometry and fuel properties on spray development.

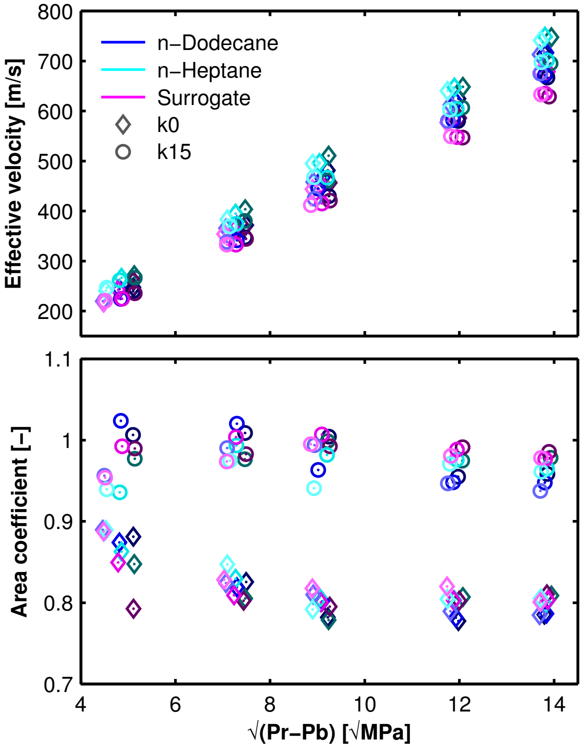

Figure 3.13: Steady effective outlet velocity (top) and area coefficient (bottom) as a function of the pressure drop across the injector for all test conditions. Note that fuels are denoted by color while nozzles are indicated by symbols.

References

[1] SALVADOR, F. J., PLAZAS, A. H., GIMENO, J., and CARRERES, M. “Complete modelling of a piezo actuator last-generation injector for diesel injection systems”. *International Journal of Engine Research* 15.1 (Jan. 2014), pp. 3–19.

[2] LUCKHCHOURA, V., PETERS, N., and DIWAKAR, R. “Computational analysis of injection-rate shapes in a small-bore direct-injection diesel engine”. *International Journal of Engine Research* 12.2 (2011), pp. 145–168.

[3] PAYRI, R., GARCIA-OLIVER, J. M., SALVADOR, F. J., and GIMENO, J. “Using spray momentum flux measurements to understand the influence of diesel nozzle geometry on spray characteristics”. *Fuel* 84.5 (2005), pp. 551–561.

[4] PAYRI, R., GARCÍA-OLIVER, J. M., BARDI, M., MANIN, J., GARCIA-OLIVER, J. M., BARDI, M., and MANIN, J. "Fuel temperature influence on diesel sprays in inert and reacting conditions". *Applied Thermal Engineering* 35.March (Mar. 2012), pp. 185–195.

[5] DESANTES, J. M., PAYRI, R., GARCIA, A., and MANIN, J. "Experimental Study of Biodiesel Blends' Effects on Diesel Injection Processes". *Energy & Fuels* 23.6 (2009), pp. 3227–3235.

[6] PAYRI, R., SALVADOR, F. J., GIMENO, J., and VENEGAS, O. "Study of cavitation phenomenon using different fuels in a transparent nozzle by hydraulic characterization and visualization". *Experimental Thermal and Fluid Science* 44 (2013), pp. 235–244.

[7] DERNOTTE, J., HESPEL, C., FOUCHER, F., HOUILLÉ, S., and MOUNAÏM-ROUSSELLE, C. "Influence of physical fuel properties on the injection rate in a Diesel injector". *Fuel* 96 (2012), pp. 153–160.

[8] PAYRI, R., SALVADOR, F. J., CARRERES, M., and DE LA MORENA, J. "Fuel temperature influence on the performance of a last generation common-rail diesel ballistic injector. Part II: 1D model development, validation and analysis". *Energy Conversion and Management* 114 (Apr. 2016), pp. 376–391.

[9] PAYRI, R., SALVADOR, F. J., GIMENO, J., and ZAPATA, L. D. "Diesel nozzle geometry influence on spray liquid-phase fuel penetration in evaporative conditions". *Fuel* 87.7 (2008), pp. 1165–1176.

[10] PAYRI, R., VIERA, J. P., GOPALAKRISHNAN, V., and SZYMKOWICZ, P. G. "The effect of nozzle geometry over internal flow and spray formation for three different fuels". *Fuel* 183 (Nov. 2016), pp. 20–33.

Chapter 4

Isothermal spray visualization

As a first step towards validating spray models, isothermal liquid spray visualization was selected to characterize the macroscopic spray. It is a relatively simple technique that provides highly useful spatial and temporal information to CFD modelers [1]. Moreover, it is widely known that the liquid isothermal spray penetration is closely related to the vapor spray penetration [2]. It has also been proven that if spray models predict correctly the vapor penetration, they also predict the fuel mixture fraction with adequate accuracy [3]. Thus isothermal liquid spray visualization is a valuable technique that can capture the effects of nozzle flow characteristics, and hence, can also be used to calibrate and evaluate spray models.

During all tests described and presented in this chapter, energizing times and injector coolant temperature were fixed at 2500 μs and 343 K respectively. The injector body temperature was maintained close to target using a special injector holder designed to have a coolant flowing at a controlled temperature in direct contact with the injector body [4].

4.1 Optical technique and setup

Figure 4.1 shows the optical setup that employs a diffused back illumination technique. The light emitted by the source is forced through a diffuser and field lens before going into the chamber. Inside the chamber, the light passes through the liquid core, which features a refractive index much greater than the one of the surrounding gas. This difference in refractive indices deflects light strongly such that the beams entering the liquid core are not captured by the camera which in turn renders dark spots on the image at those corresponding locations. While this technique itself has been long utilized visualizing liquid diesel sprays [5–9], recent introduction of a high speed pulsed light-emitting diode (LED) light source has made this optical setup/technique the best choice for liquid spray visualization for single hole nozzles [10–12]. Current high-speed camera capabilities in combination with a high-speed pulsed light source—with a controlled pulsed duration of 50 ns —produce images significantly sharper than any continuous light source or flash type light source option, and reduces the actual timing uncertainties of the image acquired.

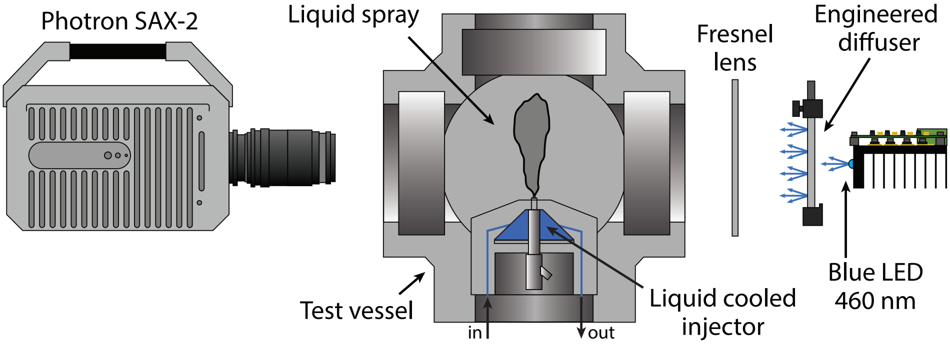

Figure 4.1: Scheme of the diffused back illumination optical setup.

In all visualization experiments performed in this study, the camera frame rate was set to 160 kHz. Sampling rate was a high priority, but it was also desired to have a field of view (FOV) of at least 60 mm with an acceptable spatial resolution. The final setup features and image of 512 pix × 112 pix with a spatial resolution of 7.1 pix/mm. The shutter time duration was set to 2.5 µs, although this is not determinant since the effective exposure timing is given by the LED pulse duration. The effective LED pulse duration was set to 50 ns and the time-phasing between the camera clock signal and the LED pulse signal was fixed at 500 ns, making sure that the complete LED pulse is captured during the exposure window.

4.2 Image processing

Each image is processed using an algorithm that detects the spray boundary and computes its associated properties. The background is calculated as an average of all the images acquired before start of injection (SOI). After the start of injection, this background is subtracted from each image frame and the result is inverted so that the spray appears as a bright object against dark background. Finally, the spray contours are detected by binarizing the image with a pre-selected threshold. The threshold was fixed to 12 % of the dynamic range of the image. The procedures followed by the algorithm after the binarization to complete the contour detection are explained in detail by PAYRI et al. [13].

Note that in this isothermal setup, the background is practically constant during the entire injection event due to absence of large temperature and density gradients. This results in a smooth, diffuse background and since the light pulse duration is short, there is little incertitude in detecting the spray boundary. Thus, a relatively large threshold was preferred to guarantee the quality of the boundary detection and ensure robustness against perturbations that result from partial beam steering or local density gradients in the region right next to the spray. Figure 4.2-top shows an example of a spray boundary detected by the algorithm plotted over the original image, where the dashed line indicates the actual spray axis. Figure 4.2-bottom presents the normalized intensity profile along the spray axis. The steep and sharp intensity drop at the spray tip is the result of combining a high speed pulsed light source, with very short pulse duration, relatively low chamber temperatures (25 °C to 40 °C) and temperature gradients, and good optical quality of the image acquisition setup.

Now it is possible to estimate the spatial uncertainty in spray boundary detection due to the threshold criteria. Figure 4.2-bottom shows the intensity thresholds calculated in that particular image for 12 % (blue dashed line) and 3 % (light gray dash-dot line) of the dynamic range. The points at which these lines intersect the intensity profile near the spray tip correspond to the spray boundary location detected for those threshold criteria. It is important to note that the 12 % blue dashed line crosses the intensity profile near the point where the slope starts to decrease, as the curve starts to become tangent to zero. The objective is to maximize sensitivity by lowering the threshold, but at the same time, to set a value that permits the robust detection of the first real physical trace of the liquid phase and not to pick up artificial signals. If the threshold is not set high enough, background camera sensor noise or beam steering—both which may affect the estimated intensity profile near the bottom-right area—could bias the spray boundary detection, rendering an over-estimated liquid spray penetration. Therefore, a compromise must be met, and evaluated for all test conditions, which resulted in the selection of 12 % as a well suited value. Note that DERNOTTE et al. [14] presented a very similar figure in their paper, which employed continuous light source and 8 μs shutter duration. Their setup would be expected to produce a shallower tip profile—in comparison to this study—because of the continuous light source and relatively long shutter time, both of which render motion blur of the spray tip during that time window. Still, DERNOTTE et al. [14] successfully demonstrate

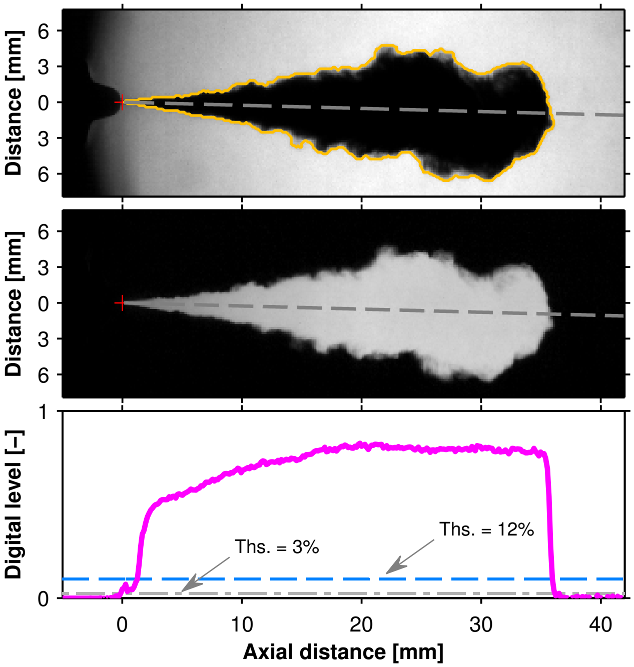

Figure 4.2: Original image with the spray boundary detected (top), actual image as processed (center) and normalized intensity profile along the spray axis (bottom). The image to be processed comes from background subtraction and inversion. The red cross indicates the nozzle outlet location. The particular frame shown is at 534 μs after SOI, the nozzle is k0 *injecting the Surrogate fuel, rail pressure is 200.0 MPa, and back pressure is 6.0 MPa, which corresponds to an ambient density of 66.3 kg/m*^{3}.

the little influence the threshold ends up having over the detected penetration and present well documented and important results from their experiments.

Once the spray contour is detected at a particular frame, spray characteristics are extracted for analysis. Figure 4.3 illustrates a single frame as captured by the camera, with the detected contour plotted over and the spray characteristics indicated. The *spray tip penetration* is the distance measured from the nozzle outlet to the furthest point in the contour detected (Figure 4.3-bottom). The *near field spreading angle* is the angle included between two linear fits performed to the spray contour detected within 1.5 mm and 9 mm axially measured from the outlet orifice. Note that these fitted lines are not forced to go through the nozzle outlet, as illustrated by the top part of Figure 4.3. The *spreading angle* is the angle included between two lines that originate at the outlet orifice and are fitted

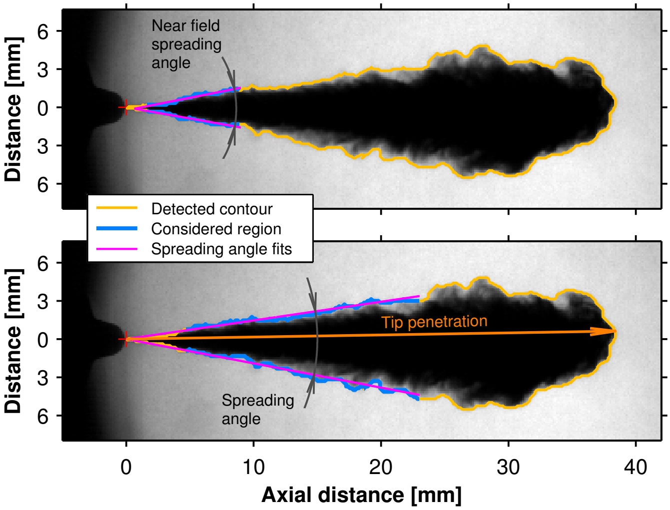

Figure 4.3: Spray characteristics extracted by the image processing algorithm. The top part illustrates the near field spreading angle estimation, while the bottom part depicts the spray tip penetration and spray spreading angle estimation. The red cross indicates the outlet orifice location. The particular frame shown is at 302 µs after SOI, the nozzle is k0 *injecting the Surrogate fuel, rail pressure is 200.0 MPa, and back pressure is 2.0 MPa, which corresponds to an ambient density of 22.8 kg/m^3.*

to the spray contours detected between 12 % and 60 % of the spray tip penetration calculated at that time frame, as indicated by the bottom part of Figure 4.3.

4.3 Test plan

The test plan is presented in Table 4.1, it consists of four rail pressures and three back pressures (thus, ambient densities), for each nozzle. The energizing time was fixed to 2500 µs in order to have an injection event long enough to enable the study of a stabilized spray. A total of 72 different test points were measured in the visualization experiments. Note that high rail pressures (i.e. 150.0 MPa and 200.0 MPa) combined with low back pressures (i.e., 2.0 MPa and 3.0 MPa) are expected to produce conditions that choke the mass flow rate in the cylindrical nozzle *k0* due to strong cavitating regimes [6, 15–18]. Still, this nozzle is expected to cavitate well before the mass flow rate reaches choke conditions [17–19]. All experimental results presented in this chapter are available for download at: `http://www.cmt.upv.es/DD01.aspx`.

Table 4.1: Spray visualization test plan.

Parameter	Value-Type	Units
K-factor	0, 1.5	-
Back pressure (P_b)	2.0, 3.0, 6.0	MPa
Rail pressure (P_r)	60.0, 90.0, 150.0, 200.0	MPa
Number of repetitions per test	8	-

4.4 The effect of nozzle geometry on spray formation

Figures 4.4, 4.5 and 4.6 show subsets of the full test matrix results obtained from the experiments. The effects of injection pressure (top side of each figure), and back pressure (bottom side of each figure) on spray development are shown for two different nozzles. The different test conditions are indicated by symbols. Each curve depicts the spray penetration as a function of time obtained by ensemble averaging multiple consecutive injection events, following the same rolling-average algorithm described by Payri et al. [13], utilizing a window size of 56 µs. The algorithm is very similar to an Savitzky-Golay digital filter but accounting for multiple digital signals (the multiple test repetitions performed).

Thanks to the nozzles being single-hole axial nozzles, the high acquisition rate employed in the experiments, and the short illumination pulse provided by the fast LED, the spray could be precisely detected in the very early stages of the penetration curve; in average, penetrations as low as 0.3 mm were detected. This permitted a good estimation of the SOI timing with respect to the trigger signal (start of energizing, SOE), by performing a linear fit to the raw data set found in the first 5 mm of the penetration curves of all repetitions, for a given set of test conditions. A good estimation of the actual SOI for each test condition facilitates the time-phasing of the penetration curves for comparison.

The top parts of Figures 4.4, 4.5 and 4.6 show that rail pressure impacts spray penetration right from the start of injection, while the bottom part shows that ambient density impacts it only at later stages (time>0.1 ms) of spray where aerodynamic interaction with surrounding gas becomes important. In spite of lower mass flow rate and momentum flux, the conical nozzle *k15* shows faster tip penetration rates in the later stages of the spray (time>0.1 ms) when compared to the cylindrical nozzle *k0*. This occurs because of the turbulent velocity profiles produced by the cylindrical nozzle [20], that enhance spray mixing and momentum exchange which in turn leads to slower tip penetration. Hence, at higher injection pressures and lower ambient density (Figures 4.4, 4.5 and 4.6, top side), where the effect of aerodynamic drag loses importance, the difference in the penetration of sprays

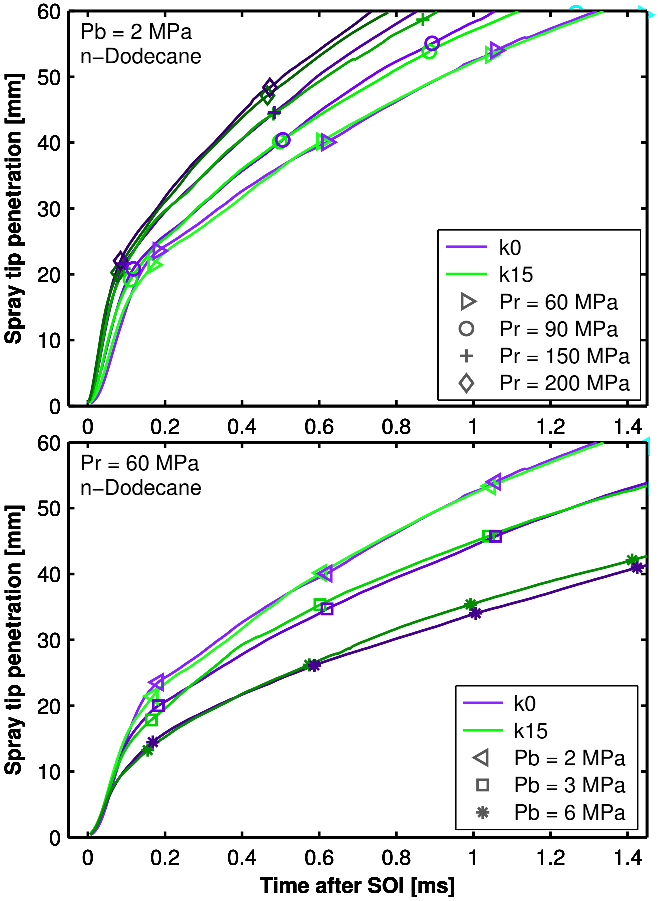

Figure 4.4: The effect of nozzle geometry on spray tip penetration for different rail pressures at a back pressure of 2.0 MPa (top), and different back pressures at a rail pressure of 60.0 MPa (bottom). The three different back pressures result in ambient densities of 22.8 kg/m^3*, 33.0 kg/m*^{3} *and 66.3 kg/m*^{3} *respectively. In this case, the fuel presented is n-dodecane.*

produced by the two nozzles is reduced. This is also due to the increasingly higher momentum flux from nozzle *k0* at higher injection pressures (see Figure 3.12) in comparison to nozzle *k15*. Consequently, higher ambient density cases (shown in the bottom parts of Figures 4.4, 4.5 and 4.6) show greater difference between the two nozzles. These conditions allow time for the aerodynamic interactions to develop, and turbulent velocity profiles in the outlet orifice become more important to the gas entrainment process, liquid break-up is enhanced and the smaller droplets exchange momentum more efficiently with the ambient gas. Note that

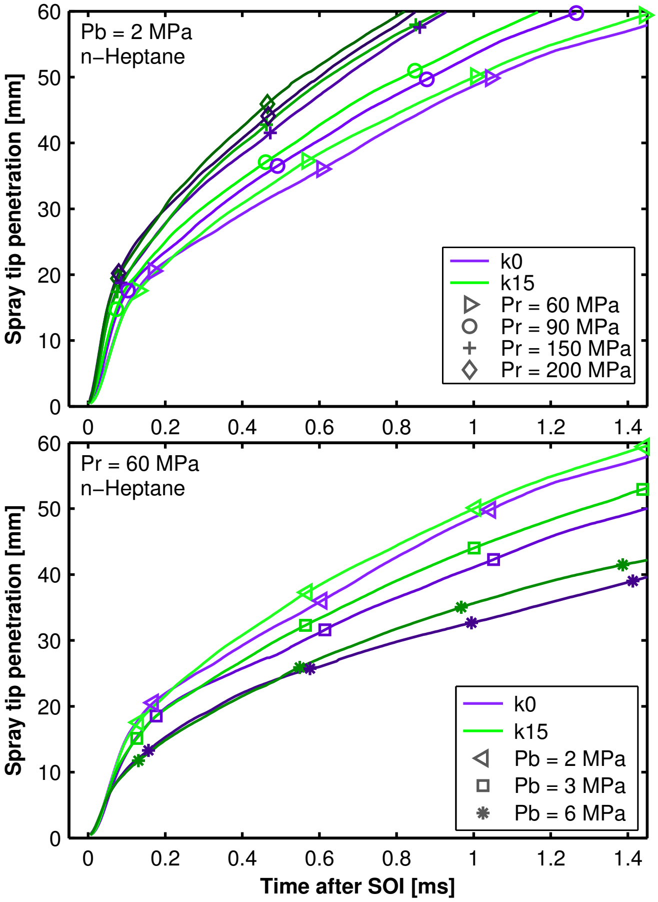

Figure 4.5: The effect of nozzle geometry on spray tip penetration for different rail pressures at a back pressure of 2.0 MPa (top), and different back pressures at a rail pressure of 60.0 MPa (bottom). The three different back pressures result in ambient densities of 22.8 kg/m^3, 33.0 kg/m^3 and 66.3 kg/m^3 respectively. In this case, the fuel presented is n-heptane.

similar results for different nozzles were reported previously [21, 22]. In both studies, authors perform numerical simulations of the liquid spray for cylindrical and conical nozzles, showing that the penetration curves start to diverge after a certain time has passed and aerodynamic interaction has played its part, even though the effect of nozzle geometry is just introduced as boundary conditions at the orifice interface. MONTANARO et al. [22] observed the same trend in their experimental results, presented in the same paper but detailed further by ZHANG et al. [23].

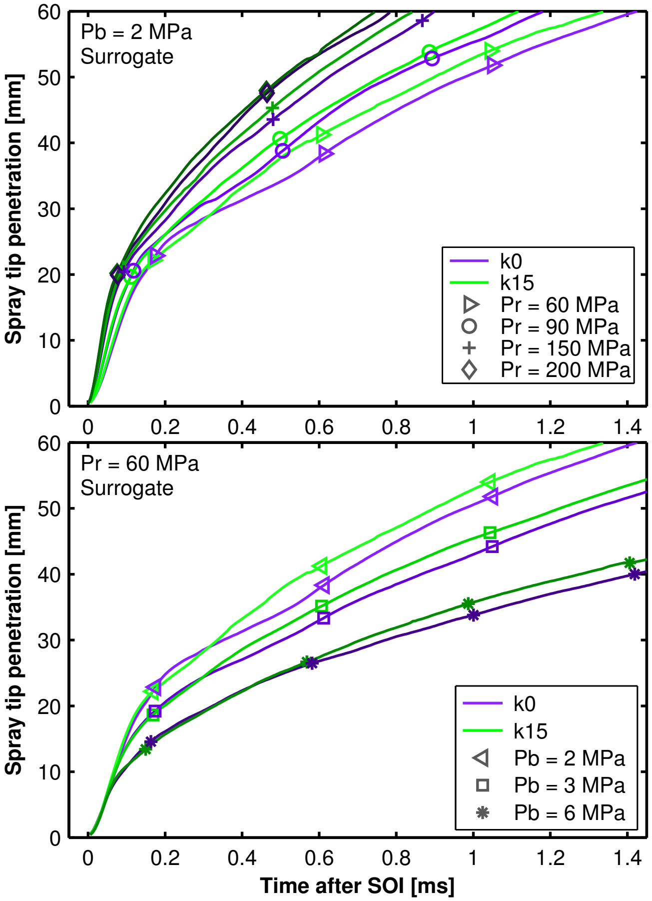

Figure 4.6: The effect of nozzle geometry on spray tip penetration for different rail pressures at a back pressure of 2.0 MPa (top), and different back pressures at a rail pressure of 60.0 MPa (bottom). The three different back pressures result in ambient densities of 22.8 kg/m^3, 33.0 kg/m^3 and 66.3 kg/m^3 respectively. In this case, the fuel presented is the Surrogate fuel.

Further analysis can be made to reach a better understanding of the effects of the nozzle geometry over the spray formation. For example, Figure 4.7 presents the near field spreading angle for two particular test repetitions. The near field spreading angle reported is defined in section 4.2, and illustrated in the top part of Figure 4.3. It is important to point out that the fits are not forced to go through the nozzle outlet. Even though it is common practice when measuring large penetration-scaled angles [6, 8], this approach attenuates local fluctuations, which are intended to be shown in this analysis. Note that in the case of Figure

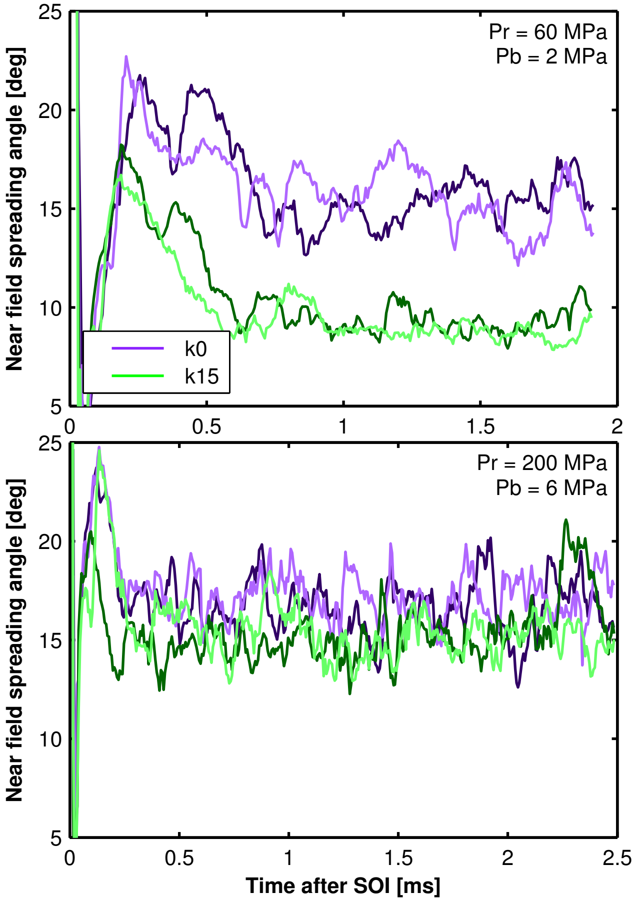

Figure 4.7: The effect of nozzle geometry on the near field spray spreading angle for two particular test repetitions at rail and back pressures of 60.0 MPa and 2.0 MPa (top), and 200.0 MPa and 6.0 MPa (bottom). Two different test repetitions are shown at each test condition, distinguised by color shades of the base nozzle color. The case presented corresponds to the Surrogate fuel.

4.7 no repetition-average behavior is presented, but instead two randomly selected test repetitions are shown. This permits the illustration of steady state trends along with transient effects such as time resolved fluctuations. The steady state behavior of these signals can be summarized in terms of time-averages of spreading angles, and the fluctuations can be quantified in terms of the standard deviation.

Figure 4.7 shows a clear difference in the near field spreading angle behavior produced by the two nozzles. All signals fluctuate significantly, which is the result of the turbulent interaction between the liquid spray and the surrounding gas. In general, the cylindrical nozzle *k0* features larger steady state near field spreading angles and fluctuations throughout the complete test matrix. In particular, the top part of Figure 4.7 shows one of the scenarios where the difference is largest—39.6 % difference between the two nozzles for the steady angles and 50.0 % for the fluctuations—while the bottom part of Figure 4.7 presents one of the cases where the difference is smallest—still, 10.2 % for the steady angles and 17.0 % for the fluctuations. Similar results have been reported previously. HAN et al. [24] studied the effect of nozzle geometry over the microscopic spray development, showing that cylindrical nozzles produce larger fluctuations in spreading angle when compared to conical nozzles. Unfortunately, details on how the angle reported is measured and the repetition-average behavior are not given. BLESSING et al. [25] also presented spreading angles of the microscopic spray, showing that cylindrical nozzles (and also, diverging nozzles) produce larger micro-spreading angles than conical nozzles, but the acquisition rate utilized for the study is not sufficient to properly detect or quantify fluctuations. On the other hand, PAYRI et al. [6] presented penetration-scaled spreading angles showing also that cylindrical nozzles render larger spreading angles in comparison to conical nozzles. Interestingly, both studies also show an effect of the nozzle geometry over the macroscopic spray tip penetration, but since the penetration rates presented are very similar between the different nozzles, and the differences reported are very small, this trend may be strongly influenced by the correct detection of the SOI timing and the time-phasing of each penetration curve, which is more uncertain at the acquisition rates of 20 kHz utilized in both cases. A comparable result was also presented by LIU et al. [26], in which two cylindrical nozzles—with and without hydro-grinding—are compared and their results show larger micro-spreading angles for the nozzle without hydro-grinding. Even though each one of these studies is different, with particular aims, nozzles, and optical techniques, one conclusion remains: turbulent velocity profiles, caused by geometrical features inside the nozzle, indeed affect the liquid spray in terms of dispersion, which includes spreading angle and fluctuations.

Following the analysis of the time-resolved spreading angles, a wider scope analysis can be made if these time-averaged values are synthesized into one single figure. Figure 4.8-top shows the time-averaged spreading angle values for the complete test matrix. The percentage differences reported previously correspond, then, to just two pairs of points within this figure. Note that, the effect of the nozzle geometry is stronger than the effect of a considerable increase in ambient density, which is well known to be a determinant parameter controlling spreading angle [9, 27]. Figure 4.8-top clearly shows that the cylindrical nozzle

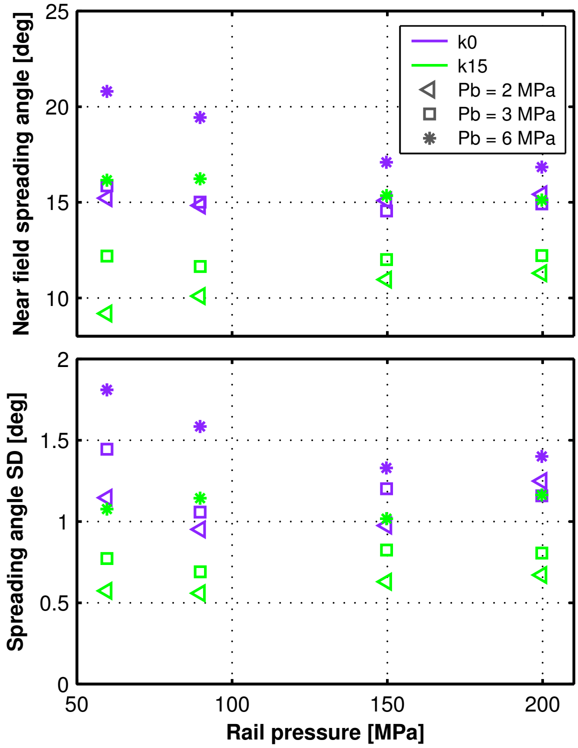

Figure 4.8: Time-averaged near field spray spreading angles (top) and their standard deviation (bottom) for all test conditions, nozzles and the Surrogate fuel. The values reported are calculated by averaging the raw data from all test repetitions from 0.8 ms after SOI to the end of the signals.

k0 renders larger spreading angles throughout the test matrix, as affirmed before. In comparison to the conical nozzle *k15*, the cylindrical nozzle *k0* shows an opposite trend of increase in spreading angle with rail pressure. While the conical nozzle shows a monotonic increase in spreading angle with back pressure (thus, ambient density), the cylindrical nozzle *k0* has two cases with 2 MPa and 3 MPa back pressure, where this monotonicity is not present. In these two cases where the ambient densities are close, cavitation and radial velocity profiles caused by turbulence inside the nozzle may play a more important role in the final spreading angle produced [16, 28, 29] than the actual density. Finally, it must be noted that the rail pressure was not found to significantly influence the overall behavior of the near-field spreading angle reported here, which has also been seen previously by other authors [27, 30–32]. Still, it must be pointed out that in cases such as these, detailed time-resolved numerical simulations of this problematic would surely help to better understand the observed trends, especially when comparing the response of each nozzle to the different pressure differentials.

Similar analysis can be made for the dispersion of the signals from which the time-averaged steady state values presented in Figure 4.8-top are obtained, as depicted in Figure 4.8-bottom. These points are, therefore, measurements of the fluctuations of the near field spreading angle at each test condition and nozzle. The results show that the cylindrical nozzle *k0* presents higher fluctuations around the mean spreading angle values throughout the test matrix. However, its response along the test matrix—both for rail and back pressures—does not show a clear trend. To this end, it must be pointed out that since these sprays are strongly turbulent, this kind of signals are seldom self similar and, therefore, the standard deviation measurements may need longer signal lengths than those utilized here, to better show the trends for the cavitating nozzle *k0*. The behavior of the conical nozzle *k15* seems to be more consistent along the rail and back pressure spectrum: fluctuations do not seem to be strongly affected by rail pressure, while increasing back pressure—mainly, chamber density—indeed increases the fluctuations. Overall, this is a very interesting result because it suggests that, even though outlet velocities increase with rail pressure—and thus, the Reynolds number—it seems to end up not playing a key role in the spray angle magnitude and fluctuations. This is one of the many cases where detailed nozzle-spray numerical simulations can provide valuable information on the fundamental driving mechanisms behind such behavior.

4.5 Spray formation for different fuels

The effect of nozzle geometry also depends on the physical properties of the fuel. Figures 4.9 and 4.10 present results of select test conditions, to illustrate how nozzles *k15* and *k0*, respectively, respond to the different fuels. In general, n-heptane shows slower penetration rates throughout the test matrix, that is expected due to the lower density, viscosity and surface tension, all of which enhance liquid breakup and momentum exchange between fuel and ambient gas, as reported by Crua et al. [33] and later Ding et al. [34] in their microscopic studies. Figure 4.10 shows that for non-cavitating conditions the Surrogate spray penetrates faster than the n-dodecane spray. Featuring slightly higher density and comparable viscosity and surface tension, the Surrogate liquid spray conserves momentum better than the n-dodecane spray. Similar observations were reported by Desantes et al. [35], Dernotte et al. [14] and Park et al. [36] with respect to fuel density. However, that conclusion does not hold for the cylindrical nozzle *k0*, as seen in Figure 4.9. In these conditions, trends between the sprays produced by the two fuels are inverted, and the n-dodecane spray has the fastest tip penetration.

Since the rest of the variables controlling spray tip penetration are kept constant and controlled between nozzles, the different spray tip penetration responses observed for n-dodecane and Surrogate fuels should be reflected in spray spreading angle [8, 9, 14]. Figure 4.11 shows penetration-scaled spreading angles to asses the former conclusion. Reported values correspond to the spray spreading angle defined in section 4.2, and illustrated in the bottom part of Figure 4.3. n-Heptane sprays feature the largest macroscopic spreading angles through the whole test matrix, consistent with the spray penetration curves presented in Figures 4.10 and 4.9, due to its lower density, viscosity and surface tension [33, 34]. Again in agreement with the penetration results, the trends between n-dodecane and Surrogate sprays depend on the nozzle, or the cavitation regime. For the cylindrical nozzle *k0* the Surrogate spray produces larger spreading angles in comparison to the n-dodecane spray, while the opposite holds for nozzle *k15*. Note that for each fuel and nozzle, these spreading angles are ordered with back pressure and thus, ambient density, as found in the literature [2, 9].

4.6 A further analysis on nozzle and fuel effects on spray formation, mixing and fluctuations

Although the macroscopic characteristics of the spray are often quantified as steady state values, the real spray is seldom a steady state process. Even for the fully developed “steady” spray, considerable local fluctuations are still present. These fluctuations are evidence of the strongly turbulent mixing process and therefore, differences registered in spray tip penetration are not only explained by “steady” state spreading angles, but also by fluctuations and turbulence, both of which enhance momentum exchange.

Figure 4.12 shows fluctuation maps of the sprays produced by the two nozzles and three fuels at a particular case of test conditions. The map is calculated as the standard deviation between all binary images of the detected sprays from a given test. Examples of the binary images can be found in the work of PAYRI et al. [13]. This calculation is done past 0.8 ms after SOI to guarantee that the spray is in steady state. Therefore, a black pixel corresponds to non-fluctuating regions: the spray never occupies that pixel or the pixel is always considered to be within the spray during the time window considered. On the other hand, the brighter the pixel the more likely it is for fluctuations to occur at that region (and/or the stronger fluctuations at that region are) and, as expected, this happens near the spray boundary.

Figure 4.12 shows quite a lot of information. First are the different shapes of the sprays produced by each nozzle. The cylindrical nozzle *k0* (Figure 4.12-

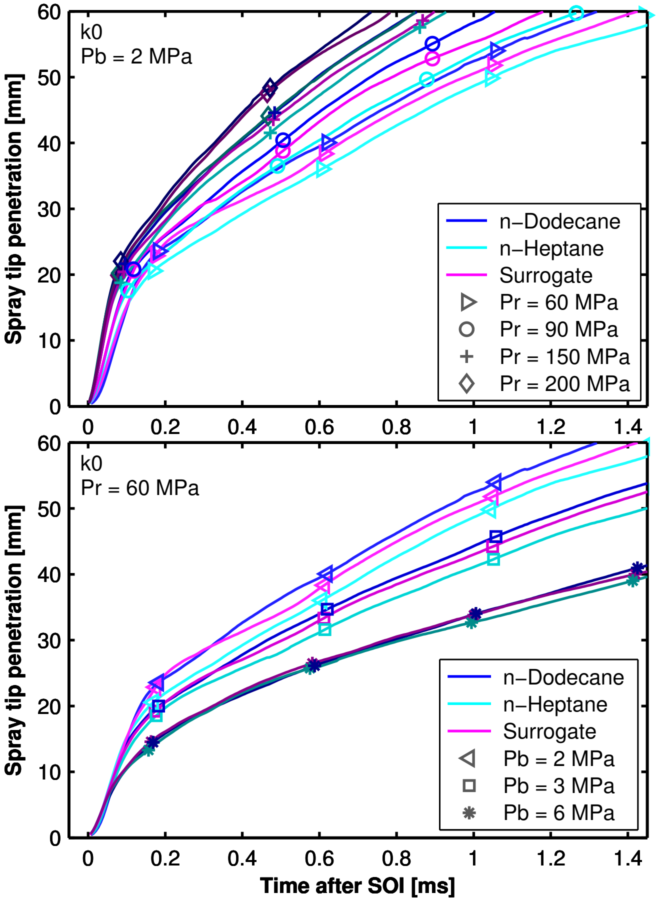

Figure 4.9: Spray tip penetration for all fuels and different rail pressures at a back pressure of 2.0 MPa (top), and different back pressures at a rail pressure of 60.0 MPa (bottom). The three different back pressures result in ambient densities of 22.8 kg/m^3, 33.0 kg/m^3 and 66.3 kg/m^3 respectively. In this case, the nozzle is k0.

left column) produces a spray that spreads quickly after the fuel has just exited the nozzle, while the spray produced by the conical nozzle *k15* (Figure 4.12-right column) spreads progressively but at a lower rate along the longitudinal coordinate. This is directly related to the higher turbulence levels and radial velocity profiles within the nozzle, caused by the cylindrical nozzle geometry, as KOO et al. [37] demonstrate in their fundamental study. This is also what the near field spreading angles presented in Figures 4.7 and 4.8 quantify. In terms of spray width, nozzle *k0* produces a spray that is, on average, wider up to approximately

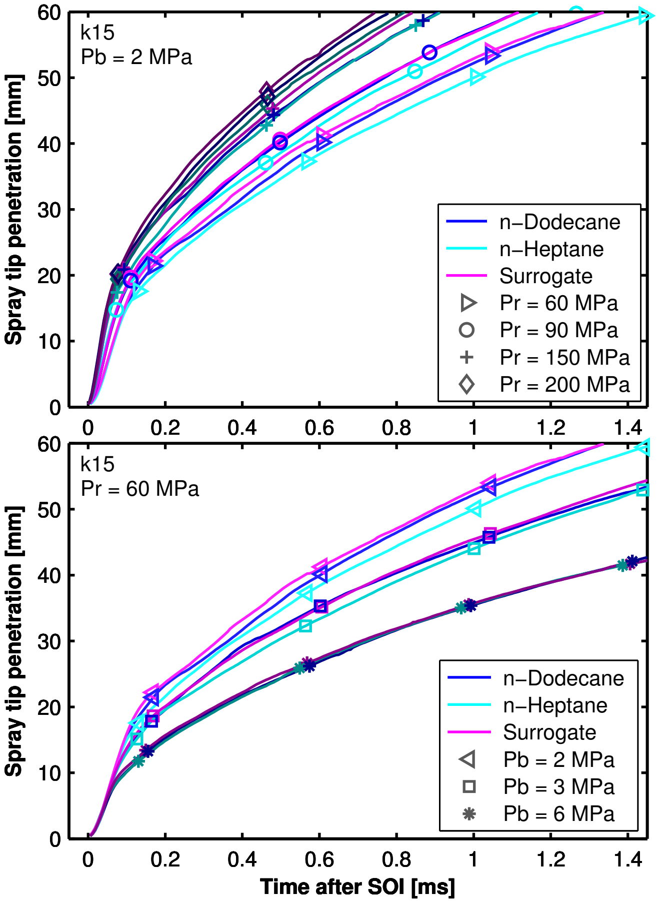

Figure 4.10: Spray tip penetration for all fuels and different rail pressures at a back pressure of 2.0 MPa (top), and different back pressures at a rail pressure of 60.0 MPa (bottom). The three different back pressures result in ambient densities of 22.8 kg/m^3, 33.0 kg/m^3 and 66.3 kg/m^3 respectively. In this case, the nozzle is k15.

15 mm from the nozzle tip, point after which both sprays start to converge to similar widths. The spray width profile along the axial direction for cavitating nozzles was discussed by PAYRI et al. [29], while the shape of sprays that spread progressively has recently been analyzed by PICKETT et al. [12] (note that in this study, the nozzle features a k-Fator of 1.5). These studies, along with the results presented here, provide evidence to the fact that nozzle geometry indeed plays a key role not only in the near field spray formation but also in the macroscopic spray. The nozzle geometry influences the behavior of the steady spray in the first

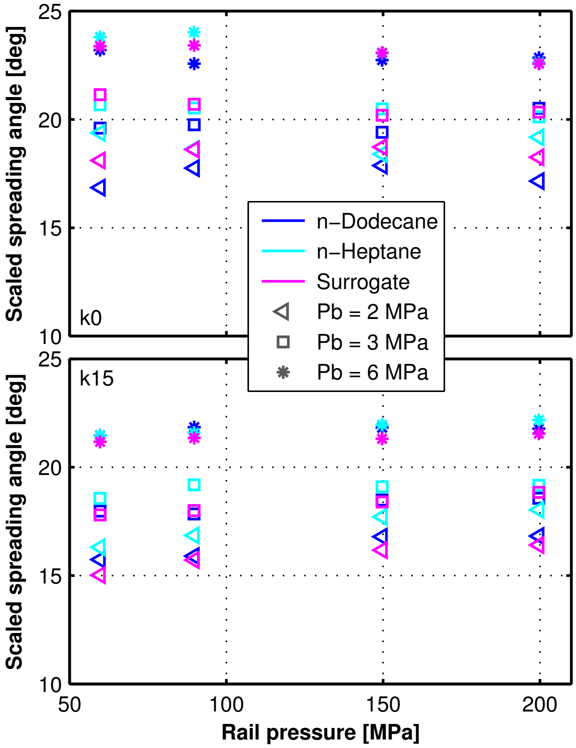

Figure 4.11: Time-averaged penetration-scaled spray spreading angles for all test conditions, nozzles and fuels. Note that the top part shows nozzle k0 *while nozzle* k15 *is presented at the bottom part. The values reported are calculated by averaging the raw data from all test repetitions from 0.8 ms after SOI to the end of the signals.*

millimeters which, in turn, affects the strength of the aerodynamic interactions and momentum exchange downstream.

Moreover, the fluctuation maps presented in Figure 4.12 also give insight to the spray boundary fluctuations, which are also functions of turbulence, velocity profiles within the nozzle [37], and the aerodynamic interaction between the fuel spray and the ambient gas [38]. It is important to note that, even though spreading angle fluctuations (Figure 4.8-bottom) may, at first, seem to be a similar metric to what the fluctuation maps show, they are somewhat independent: it is possible to have a spray with a very diffuse fluctuation map and, at the same time, a spreading angle with negligible standard deviation—i.e., the contour fluctuating over parallels. In average, up to 15 mm from the nozzle tip, the cylindrical nozzle *k0* seems to produce a more diffuse fluctuation map in comparison to the conical

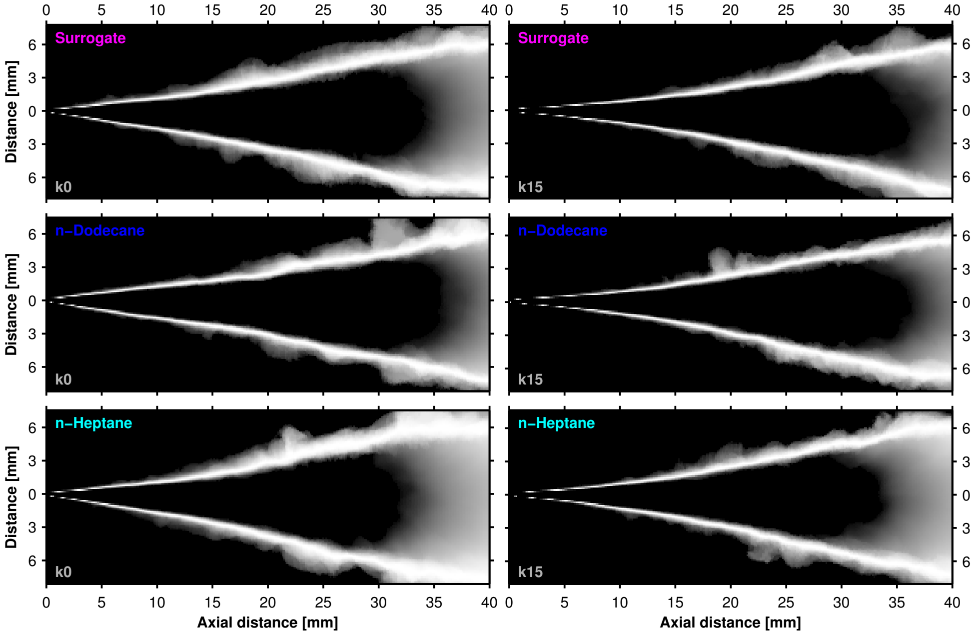

Figure 4.12: Spray fluctuation maps for all nozzles and fuels at a rail pressure of 60.0 MPa and a back pressure of 2.0 MPa. The maps comprise all test repetitions and images from 0.8 ms after SOI to the end of the signals.

nozzle *k15*, which means that its line-of-sight liquid phase spray boundary fluctuates more. Downstream, where the aerodynamic interactions have had time to shape the sprays, the fluctuations are larger and the difference between nozzles, in terms of boundary fluctuations, is reduced. The information given by these maps may imply that the differences in spray tip penetration observed in the later part of the penetration curve (and also observed by SOM et al. [21] and MONTANARO et al. [22]) are originated in the near-nozzle region part of the steady spray—where the spray produced by the cylindrical nozzle exchanges momentum with the ambient gas at a higher rate—but are evidenced later downstream, where the differences in the remaining spray momentum are appreciable.

Figure 4.12 also confirms what has already been discussed: in average throughout the test matrix and for both nozzles, sprays produced by n-heptane feature larger dispersion (both angle and fluctuations) when compared to those of n-dodecane and the Surrogate fuel [33, 34]. Also, the dispersion of the n-dodecane spray is less affected by the nozzle geometry in comparison to the Surrogate spray, and this result is in agreement with the spray tip penetration results presented in Figures 4.10 and 4.9 and penetration-scaled spreading angles presented in Figure 4.11.

4.7 Conclusions

A complete high-speed visualization of the isothermal liquid spray was carried out, extracting spray tip penetration and spray spreading angle from the images acquired [39].

The cylindrical nozzle, *k0*, in spite of higher momentum flux and mass flow rate due to higher flow area, shows slower spray tip penetration and higher spread angle when compared to the conical nozzle *k15*. This is mainly due to highly turbulent nozzle exit conditions caused by cavitation inside the cylindrical nozzle that leads to higher aerodynamic drag on the spray. At higher rail pressure and relatively low ambient/back pressure, where the aerodynamic drag is less dominant, the cylindrical nozzle spray penetration is very close to that of the conical nozzle spray. The spreading angle is found to be inversely proportional to the tip penetration. The spreading angle is dominated by the nozzle geometry followed by the ambient density. The rail pressure on the other hand, was not found to significantly influence the near-field spreading angle and has no influence on the standard deviation of the spreading angle This suggests that, even though outlet velocities increase with rail pressure—and thus, the Reynolds number—it seems not to end up playing a key role in the spray angle magnitude and fluctuations.

n-Heptane shows slowest tip penetration due to its lower density, viscosity and surface tension, all which enhance liquid breakup and momentum exchange between fuel and ambient gas. n-Dodecane and the Surrogate fuel show very similar spray behavior for variations in injection pressure and back pressure. However, the surrogate fuel shows higher penetration than n-dodecane using the conical nozzle *k15* and lower penetration using cylindrical nozzle *k0*, which was found to be in agreement with the near-field spreading angle and spreading angle fluctuations reported.

The experimental findings from this chapter on the macroscopic spray behavior, and the large database obtained (available for download at: `http://www.cmt.upv.es/DD01.aspx`), could be used to validate CFD models that might help the community understand the fundamental driving mechanisms behind these observations.

References

[1] BRULATOUT, J., GARNIER, F., MOUNAI M-ROUSSELLE, C., and SEERS, P. “Calibration strategy of diesel-fuel spray atomization models using a design of experiment method”. *International Journal of Engine Research* 17.7 (Sept. 2016), pp. 713–731.

[2] NABER, J. D. and SIEBERS, D. L. “Effects of Gas Density and Vaporization on Penetration and Dispersion of Diesel Sprays”. *SAE Paper 960034*. Vol. 105. 412. Society of Automotive Engineers, Inc., Warrendale, Pennsylvania, USA, Feb. 1996, pp. 82–111.

[3] PICKETT, L. M., MANIN, J., GENZALE, C. L., SIEBERS, D. L., MUSCULUS, M. P. B., and IDICHERIA, C. A. “Relationship Between Diesel Fuel Spray Vapor Penetration/Dispersion and Local Fuel Mixture Fraction”. *SAE International Journal of Engines* 4.1 (2011), pp. 764–799.

[4] PAYRI, R., GARCÍA-OLIVER, J. M., BARDI, M., MANIN, J., GARCIA-OLIVER, J. M., BARDI, M., and MANIN, J. “Fuel temperature influence on diesel sprays in inert and reacting conditions”. *Applied Thermal Engineering* 35.March (Mar. 2012), pp. 185–195.

[5] MORGAN, R., WRAY, J., KENNAIRD, D. A., CRUA, C., and HEIKAL, M. R. “The Influence of Injector Parameters on the Formation and break-Up of a Diesel Spray”. *SAE Technical Paper 2001-01-0529* (2001).

[6] PAYRI, F., BERMÚDEZ, V., PAYRI, R., and SALVADOR, F. J. “The influence of cavitation on the internal flow and the spray characteristics in diesel injection nozzles”. *Fuel* 83.4-5 (2004), pp. 419–431.

[7] PAYRI, R., MOLINA, S., SALVADOR, F. J., and GIMENO, J. “A study of the relation between nozzle geometry, internal flow and sprays characteristics in diesel fuel injection systems”. *KSME International Journal* 18.7 (2004), pp. 1222–1235.

[8] DESANTES, J. M., PAYRI, R., SALVADOR, F. J., and SOARE, V. “Study of the influence of geometrical and injection parameters on Diesel Sprays characteristics in isothermal conditions”. *SAE Technical Paper 2005-01-0913* (2005).

[9] DESANTES, J. M., PAYRI, R., SALVADOR, F. J., and GIL, A. “Development and validation of a theoretical model for diesel spray penetration”. *Fuel* 85.7-8 (2006), pp. 910–917.

[10] Pickett, L. M., Genzale, C. L., Manin, J., Malbec, L.-M., and Hermant, L. "Measurement Uncertainty of Liquid Penetration in Evaporating Diesel Sprays". *ILASS Americas, 23rd Annual Conference on Liquid Atomization and Spray Systems*. May. Ventura, CA (USA): ILASS-Americas, 2011.

[11] Manin, J., Bardi, M., and Pickett, L. M. "Evaluation of the liquid length via diffused back-illumination imaging in vaporizing diesel sprays". *Comodia*. Fukuoka, 2012.

[12] Pickett, L. M., Manin, J., Payri, R., Bardi, M., and Gimeno, J. "Transient Rate of Injection Effects on Spray Development". *SAE Technical Paper 2013-24-0001* (2013).

[13] Payri, R., Gimeno, J., Viera, J. P., and Plazas, A. H. "Needle lift profile influence on the vapor phase penetration for a prototype diesel direct acting piezoelectric injector". *Fuel* 113 (2013), pp. 257–265.

[14] Dernotte, J., Hespel, C., Houille, S., Foucher, F., and Mounaïm-Rousselle, C. "Influence of Fuel Properties on the Diesel Injection Process in Nonvaporizing Conditions". *Atomization and Sprays* 22.6 (2012), pp. 461–492.

[15] Payri, R., Salvador, F. J., Gimeno, J., and Zapata, L. D. "Diesel nozzle geometry influence on spray liquid-phase fuel penetration in evaporative conditions". *Fuel* 87.7 (2008), pp. 1165–1176.

[16] Desantes, J. M., Payri, R., Salvador, F. J., and De la Morena, J. "Influence of cavitation phenomenon on primary break-up and spray behavior at stationary conditions". *Fuel* 89.10 (2010), pp. 3033–3041.

[17] Qiu, T., Song, X., Lei, Y., Dai, H., Cao, C., Xu, H., and Feng, X. "Effect of back pressure on nozzle inner flow in fuel injector". *Fuel* 173 (2016), pp. 79–89.

[18] He, Z., Guo, G., Tao, X., Zhong, W., Leng, X., and Wang, Q. "Study of the effect of nozzle hole shape on internal flow and spray characteristics". *International Communications in Heat and Mass Transfer* 71 (2016), pp. 1–8.

[19] Payri, R., Salvador, F. J., Gimeno, J., and Venegas, O. "Study of cavitation phenomenon using different fuels in a transparent nozzle by hydraulic characterization and visualization". *Experimental Thermal and Fluid Science* 44 (2013), pp. 235–244.

[20] SUN, Z.-Y., LI, G.-X., CHEN, C., YU, Y.-S., and GAO, G.-X. “Numerical investigation on effects of nozzle’s geometric parameters on the flow and the cavitation characteristics within injector’s nozzle for a high-pressure common-rail DI diesel engine”. *Energy Conversion and Management* 89 (2015), pp. 843–861.

[21] SOM, S., RAMÍREZ, A. I., LONGMAN, D. E., and AGGARWAL, S. K. “Effect of nozzle orifice geometry on spray, combustion, and emission characteristics under diesel engine conditions”. *Fuel* 90.3 (2011), pp. 1267–1276.

[22] MONTANARO, A., MIGLIACCIO, M., ALLOCCA, L., FRAIOLI, V., LEE, S.-Y., ZHANG, A., and NABER, J. “Schlieren and Mie Scattering Visualization for Single- Hole Diesel Injector under Vaporizing Conditions with Numerical Validation”. *SAE Technical Paper 2014-01-1406* 2014-01-14 (2014).

[23] ZHANG, A., MONTANARO, A., ALLOCCA, L., NABER, J., and LEE, S.-Y. “Measurement of Diesel Spray Formation and Combustion upon Different Nozzle Geometry using Hybrid Imaging Technique”. *SAE Technical Paper 2014-01-1410* (2014).

[24] HAN, J.-S., LU, P.-H., XIE, X.-B., LAI, M.-C., and HENEIN, N. A. “Investigation of Diesel Spray Primary Break-up and Development for Different Nozzle Geometries”. *SAE Technical Paper* 2002-01-27 (2002).

[25] BLESSING, M., KÖNIG, G., KRÜGER, C., MICHELS, U., and SCHWARZ, V. “Analysis of flow and cavitation phenomena in diesel injection nozzles and its effects on spray and mixture formation”. *SAE Technical Paper 2003-01-1358* (2003).

[26] LIU, Z., IM, K.-S., WANG, Y., FEZZAA, K., WANG, J., XIE, X.-B., and LAI, M.-C. “Near-Nozzle Structure of Diesel Sprays Affected by Internal Geometry of Injector Nozzle: Visualized by Single-Shot X-ray Imaging”. *SAE Technical Paper 2010-01-0877* (2010).

[27] PAYRI, R., SALVADOR, F. J., GIMENO, J., and GARCIA, A. “Flow regime effects over non-cavitating Diesel injection nozzles”. *Journal of Automobile Engineering* 226 (2011), pp. 133–144.

[28] ANDRIOTIS, A. and GAVAISES, M. “Influence of vortex flow and cavitation on near-nozzle diesel spray dispersion angle”. *Atomization and Sprays* 19.3 (2009), pp. 247–261.

[29] PAYRI, R., SALVADOR, F. J., GIMENO, J., and DE LA MORENA, J. “Analysis of Diesel spray atomization by means of a near-nozzle field visualization technique”. *Atomization and Sprays* 21.9 (2011), pp. 753–774.

[30] DELACOURT, E., DESMET, B., and BESSON, B. “Characterisation of very high pressure Diesel sprays using digital imaging techniques”. *Fuel* 84.7-8 (2005), pp. 859–867.

[31] MOHAN, B., YANG, W., TAY, K. L., and YU, W. “Experimental study of spray characteristics of biodiesel derived from waste cooking oil”. *Energy Conversion and Management* 88 (2014), pp. 622–632.

[32] MOHAN, B., YANG, W., TAY, K. L., and YU, W. “Macroscopic spray characterization under high ambient density conditions”. *Experimental Thermal and Fluid Science* 59 (2014), pp. 109–117.

[33] CRUA, C., HEIKAL, M. R., and GOLD, M. R. “Microscopic imaging of the initial stage of diesel spray formation”. *Fuel* 157 (2015), pp. 140–150.

[34] DING, H., WANG, Z., LI, Y., XU, H., and ZUO, C. “Initial dynamic development of fuel spray analyzed by ultra high speed imaging”. *Fuel* 169 (2016), pp. 99–110.

[35] DESANTES, J. M., PAYRI, R., GARCIA, A., and MANIN, J. “Experimental Study of Biodiesel Blends’ Effects on Diesel Injection Processes”. *Energy & Fuels* 23.6 (2009), pp. 3227–3235.

[36] PARK, Y., HWANG, J., BAE, C., KIM, K., LEE, J., and PYO, S. “Effects of diesel fuel temperature on fuel flow and spray characteristics”. *Fuel* 162 (2015), pp. 1–7.

[37] KOO, J. Y., HONG, S. T., SHAKAL, J. S., and GOTO, S. “Influence of fuel injector nozzle geometry on internal and external flow characteristics”. *SAE Technical Paper 970354* (1997).

[38] WANG, Y., QIU, L., REITZ, R. D., and DIWAKAR, R. “Simulating cavitating liquid jets using a compressible and equilibrium two-phase flow solver”. *International Journal of Multiphase Flow* 63 (2014), pp. 52–67.

[39] PAYRI, R., VIERA, J. P., GOPALAKRISHNAN, V., and SZYMKOWICZ, P. G. “The effect of nozzle geometry over internal flow and spray formation for three different fuels”. *Fuel* 183 (Nov. 2016), pp. 20–33.

Chapter 5

Evaporative inert spray visualization

This chapter describes the evaporative inert spray visualization experiments and observations. Evaporative sprays increase in complexity in comparison to isothermal sprays, since two thermodynamic phases co-exist. Liquid fuel is injected into a hot ambient gas, the jet is atomized by the aerodynamic interaction between the liquid fuel and the dense ambient gas, at the same time the spray is entraining the surrounding hot gas which transfers energy to the liquid fuel to eventually vaporize it completely downstream. It is known that if spray models predict correctly the vapor penetration, they also predict the fuel mixture fraction with adequate accuracy [1], which is essential for combustion analysis. Due to the complexity of this process, quality measurements are essential for model validation and also for direct experimental analysis.

During all tests described and presented in this chapter, energizing times were fixed at 2500 µs. The injector body temperature was maintained close to target using a special injector holder designed to have a coolant flowing at a controlled temperature in direct contact with the injector body [2]. The temperature of the coolant is adjusted in function of the discharge chamber gas temperature and density, to guarantee a constant sac inner wall temperature of approximately 110 °C [2].

5.1 Optical setup

The optical setup is displayed in Figures 5.1 and 5.2 from top and isometric views respectively. The test chamber is cut in both figures to better illustrate the configuration. The setup consisted of two separate cameras and optical arrangements for the visualization of liquid and vapor phases of the fuel spray. Figure 5.1 also contains indications of each component and overall summaries of each setup. Note that even though the cameras' frame rates were not equal, both cameras recorded all injection events simultaneously, triggered by the same command signal sent to the injector.

Liquid phase was visualized through a diffused back illumination (DBI) setup. The recent introduction of a high speed pulsed light-emitting diode (LED) has made this optical setup/technique very convenient for liquid spray visualization of single hole nozzles [3–6]. Current high-speed camera capabilities in combination with a high-speed pulsed light source—with a controlled pulsed duration of 50 ns —produce images significantly sharper than any continuous light source or flash type light source option, and reduce the actual timing uncertainties of the image acquired. In this setup, the light emitted by the source is forced through a diffuser, a field lens and a beam splitter before going into the chamber. Inside the chamber, the light passes through the liquid core which features a refractive index much greater than the one of the surrounding gas. This difference in refractive indices deflects light strongly such that the beams entering the liquid core are not captured by the camera which, in turn, renders dark spots on the image at those corresponding locations. The main trajectory of this light is indicated by the blue arrow in Figure 5.1. Note that since the source light is diffuse, each pixel rendered in the image results from a composition of beams that take different paths through the test chamber, hence, the collection system captures all but highly deflected rays (i.e. those that cross liquid phase), which makes this technique virtually insensitive to small refractive index changes such as local gas temperature fluctuations or the vapor phase of the fuel spray. This is translated into a diffuse, constant and smooth background which is essential for the pixel-wise extinction computation explained later in section 5.2 [3, 4]. A slight effect of the vapor phase is still observable in the instantaneous images (often referred to as "beam steering" [3]) but this is discarded by feeding the segmentation algorithm with the appropriate threshold [3, 7]. The camera utilized for this technique was a Phantom V12, acquiring images of 320 pix × 96 pix at 120 kHz with a spatial resolution of 6.38 pix/mm. This produced a 50 mm field of view (FOV) along the spray axis, and a maximum measurable liquid penetration length of 45 mm, taking into account the location of the nozzle. The actual exposure time was given by the effective LED pulse duration, which was set to 50 ns .

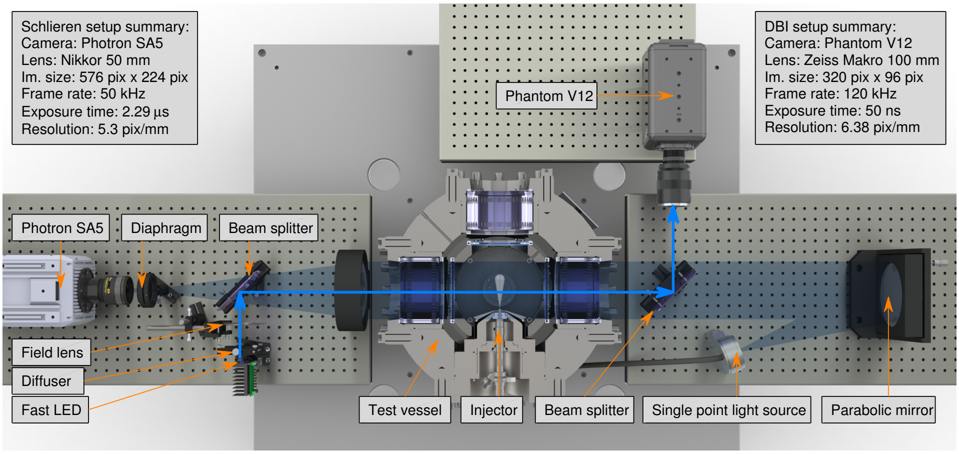

Figure 5.1: Plan view of the optical setup.

Schlieren imaging has been successfully employed by several researchers to identify gradients in refractive indices of transparent media. For vaporizing diesel sprays, this technique is able to capture the line-of-sight boundary between vaporized fuel and ambient gases, as there is an appreciable difference in refractive indices between these [7–9]. Since the rays of light are collimated into a cylindrical beam, small deflections due to refractive index gradients are rendered in the image as shades. In this study, the vapor spray was visualized through a single-pass Schlieren setup [9], which is often applied to axi-symmetrical single hole nozzles. Multi-hole injectors require a two-pass setup and a high temperature mirror as explained by PAYRI et al. [10]. The final setup is very similar to the setups employed for the CMT experiments in [8, 11, 12]. The camera was a Photron SA5, sampling images of 576 pix × 224 pix at 50 kHz with a spatial resolution of 5.3 pix/mm. This produced a FOV along the spray axis of 108 mm, and considering window limits and nozzle location, the maximum vapor penetration length measurable was 96 mm. The exposure time was set to 2.28 µs.

As shown in Figures 5.1 and 5.2, beam splitters were located at either side of the vessel to allow for the light of each technique to travel across the same line-of-sight but in different directions.

5.2 Image processing

Each image was processed using an algorithm that detects the spray boundary and computes its associated properties. The algorithms varied between the two

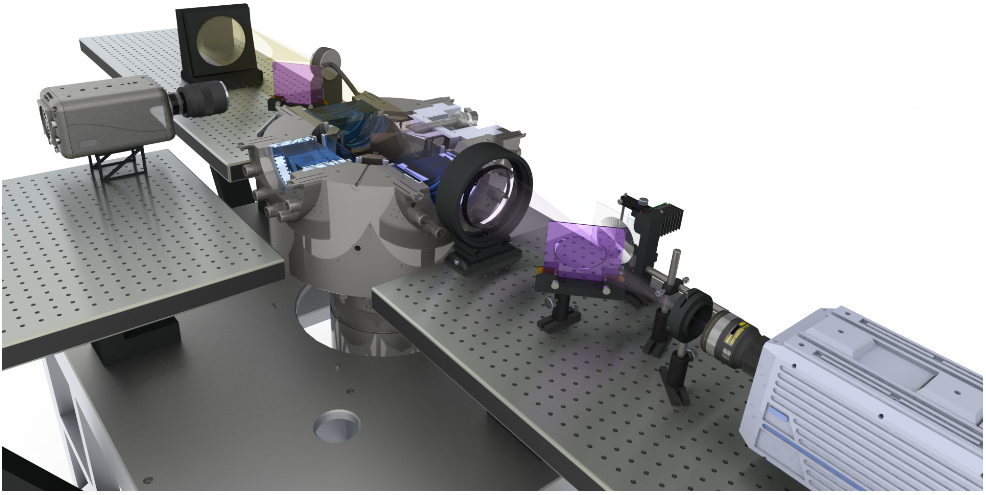

Figure 5.2: Isometric view of the optical setup.

techniques to maximize the detection performance of each setup.

Diffused back illumination (DBI) images were processed with a segmentation algorithm that binarizes a pre-processed image based on absolute threshold. The pre-processed image is a 2D extinction map, obtained by computing the pixel-wise optical thickness (τ) following Beer-Lambert's law:

$$\tau = -\ln(I_i/I_o) \tag{5.1}$$

Where I_i is the digital value of a given pixel at instant i and I_o is the digital value of that same pixel in the reference state, which, in this case is the background image before the injection. The background is calculated as an ensemble average of all the images acquired before start of injection (SOI). The absolute threshold set for the binarization of the resulting extinction map computed from Eq. (5.1) was set to 0.6 [3, 7].

Schlieren images of vapor phase are processed differently. The program consists of two extensively used approaches for the processing of these type of images. Two binarized images are obtained from two different criteria and then merged to maximize sensitivity. The first algorithm was originally developed at Sandia National Laboratories (SNL) and is available for download on the ECN website (`http://www.sandia.gov/ecn/`). The routine detects temporal changes in pixel-wise intensities by taking the temporal derivative of a series of images. This produces a 2D map where pixels with higher intensity represent pixels that are changing their digital values in time. The temporal nature of this algorithm makes it robust to variations between optical setups, and makes it very strong for transparent spray images, for example, of very dilute sprays, low ambient density conditions, light fuels, etc. On the other hand, it does not work properly for spray images with relatively constant intensity levels, for example: images of non-evaporative sprays, diaphragm-cut Schlieren vapor sprays (which are often very dark), combustion-saturated sprays, etc. In these situations, spray tip penetration is still captured correctly while the full spray boundary is not. Therefore, an additional intensity-sensitive algorithm was adapted, explained in detail by PAYRI et al. [10], enhanced with the dynamic background correction detailed by BENAJES et al. [11] and PAYRI et al. [12]. The two binary maps obtained from each algorithm are combined into a single binary image from which the contour is extracted. This approach maximizes sensitivity since it takes advantage of the robustness of the SNL algorithm for the spray tip region—and dilute regions or sprays—but at the same time allows for good contour detection in the near nozzle region, where the liquid core often generates a very dark image.

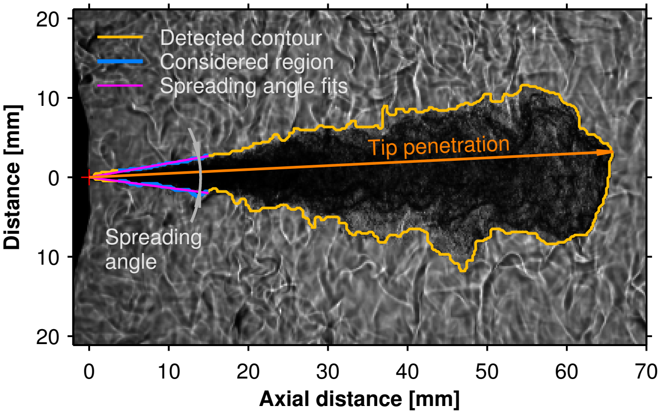

Figure 5.3: Spray tip penetration and spreading angle definitions illustrated over a Schlieren image of nozzle k0*, injecting the Surrogate fuel at 150 MPa, with an ambient temperature of 900 K and an ambient density of 22.8 kg/m*^{3}.

All processing algorithms extract macroscopic characteristics from the detected contours. Figure 5.3 illustrates the definitions for the spray tip penetration and spreading angle utilized in this study. The penetration is calculated as the distance between the outlet orifice and the furthest point in the detected boundary.

The vapor spreading angle is calculated as the angle included between two lines that originate at the outlet orifice and are fitted to the spray contours detected within 3.6 mm and 15 mm axially measured from the nozzle tip.

5.3 Test plan

Table 5.1: Evaporative inert spray visualization test plan, centered on ECN Spray A boundary conditions [8].

Parameter	Value-Type	Units
Ambient density (ρ)	22.8	kg/m^3
Ambient temperature (T_a)	800, 900, 970	K
Rail pressure (P_r)	60, 90, 150, 200	MPa
Number of points	12 per nozzle and fuel	
Ambient density (ρ)	15.2, 30.4	kg/m^3
Ambient temperature (T_a)	800, 900	K
Rail pressure (P_r)	60, 90, 150	MPa
Number of points	12 per nozzle and fuel	
Total number of points	24 per nozzle and fuel	

The test plan, presented in Table 5.1, is centered on ECN Spray A boundary conditions [8], with parametric variations around these. Since the time available for experiments was limited, an additional rail pressure (200 MPa) and ambient temperature (970 K) were performed only at the reference ambient density case (22.8 kg/m^3). Table 5.1 is sub-divided into these two groups of points for easier visualization of the test plan. For all conditions, the vessel was filled with nitrogen and the energizing time was fixed at 2.5 ms. All test points were performed for the two nozzles and three fuels, comprising a total of 144 test points in the high temperature/high pressure test rig. Once more, all experimental results presented in this chapter are available for download at: `http://www.cmt.upv.es/DD01.aspx`.

5.4 Evaporative spray development

Figure 5.4 presents a time sequence of Schlieren images of two independent injection events. This sequence demonstrates the typical behavior of evaporative diesel sprays: fuel is injected into a hot ambient gas, the jet velocity and ambient density shear and atomize the liquid core, the spray entrains the surrounding hot

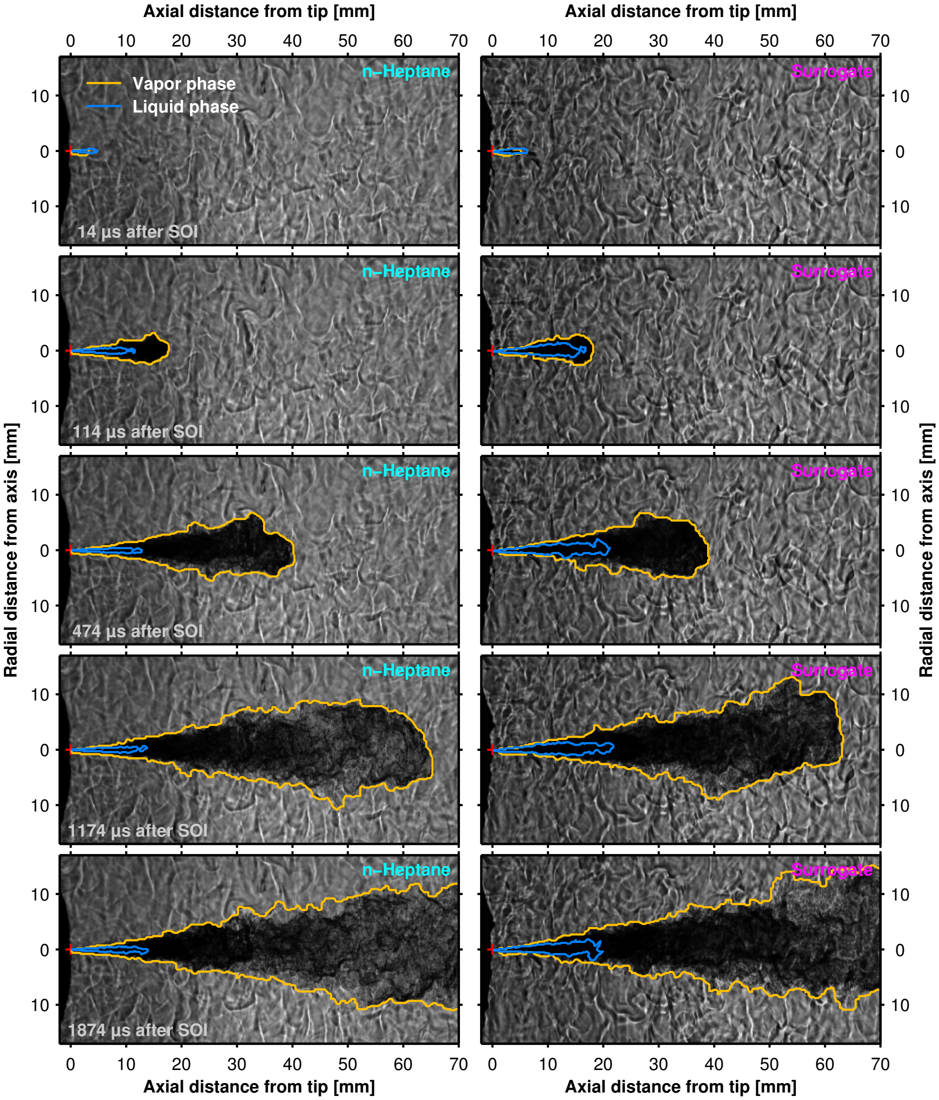

Figure 5.4: Time sequence of Schlieren images of two injection events. Images have been trimmed both in the radial and axial directions from their original size, for better fit in this figure. The contours detected for the liquid and vapor phases are plotted to scale over the original Schlieren images. Note that contours detected for the liquid phase come from DBI images acquired with the other camera. In this case, the nozzle is k15*, rail pressure is 150 MPa, ambient density is 22.8 kg/m^3 and ambient temperature is 800 K*

.

gas which transfers energy to the liquid fuel and, downstream, liquid fuel eventually evaporates completely [13]. Note that this phenomena presents a great challenge to numerical models [14, 15]. The vapor phase continues to penetrate, exchanging momentum with the ambient gas and progressively slowing down.

In Figure 5.4, notice how the liquid core of n-heptane spray is considerably smaller than the Surrogate spray, not only in the axial direction but also in width. The vapor phase of the two fuels, however, present very similar behavior in terms of spray tip penetration and angle. These findings will be analyzed in detail in the following sections.

5.5 Spray tip penetration

This section reports spray tip penetration results. Each curve in figures presented in this section depicts the spray penetration as a function of time obtained by ensemble averaging multiple consecutive injection events, following the same rolling-average algorithm described by PAYRI et al. [10], utilizing an averaging window size of 200 µs. The algorithm is very similar to an Savitzky-Golay digital filter but accounting for multiple digital signals (the multiple test repetitions performed).

The ensemble-averaged signal is then aligned in time with the SOI timing, which is estimated by performing a linear fit to the raw data set found in the first 7 mm of the penetration curves of all repetitions, for a given set of test conditions. A good estimation of the actual SOI for each test condition facilitates the time-phasing of the penetration curves for comparison. In this section, continuous and dashed curves represent the vapor and liquid phases of the spray, respectively, unless specified otherwise.

5.5.1 The effect of ambient temperature and rail pressure

Ambient density (ρ), ambient temperature (T_a) and rail/injection pressure (P_r) are few of the most important parameters, when considering evaporating diesel sprays, that significantly influence the spray and combustion behavior [12, 16]. Ambient density and rail/injection pressure act as a momentum sink and source, respectively while ambient temperature serves as evaporative energy source. Figure 5.5 depicts a particular case of nozzle *k0* injecting n-dodecane fuel at four different rail pressures and three different ambient temperatures. The ambient density is fixed at 22.8 kg/m^3 by increasing the ambient pressure (P_b) from 5.53 MPa to 6.72 MPa compensating for increase in T_a from 800 K to 970 K, respectively. For a fixed ambient density (momentum sink), the liquid penetration

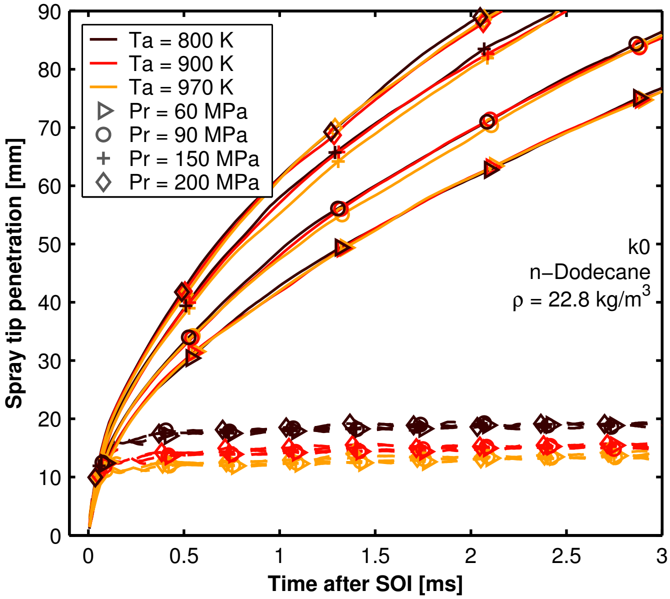

Figure 5.5: The effect of ambient temperature on the vapor and liquid spray development. In this case, the nozzle is k0*, the fuel presented is n-dodecane and ambient density is 22.8 kg/m^3.*

curves (dashed lines) collapse by ambient temperature values while the vapor penetration curves (solid lines) collapse by injection pressure values. Thus the liquid penetration is controlled by ambient temperature (evaporative energy source to vaporize fuel), while the vapor penetration is controlled by injection pressure (momentum source). The liquid penetration length is not influenced by rail pressure. This is typical when there is abundance of evaporative energy available, i.e., the rate of vaporization is influenced by rate of entrainment/mixing. As the fuel injection rate increases with injection pressure, the air entrainment increases proportionately, thus maintaining the energy balance and liquid length as previously observed in literature [13, 17]. Since the vapor spray is momentum-driven, changes in ambient temperature—at constant ambient density—are not expected to affect the vapor spray penetration or spreading angle, as different studies on multi-hole nozzles have previously observed [18, 19]. There is a secondary effect due to the increase in P_b and T_a to maintain constant ρ: the momentum flux of the spray decreases and hence, so does the vapor penetration. However, it is not experimentally observable as a clear trend as the variation of P_b is much less (<1.6 %) than the absolute value of P_r.

5.5.2 Comparing nozzles

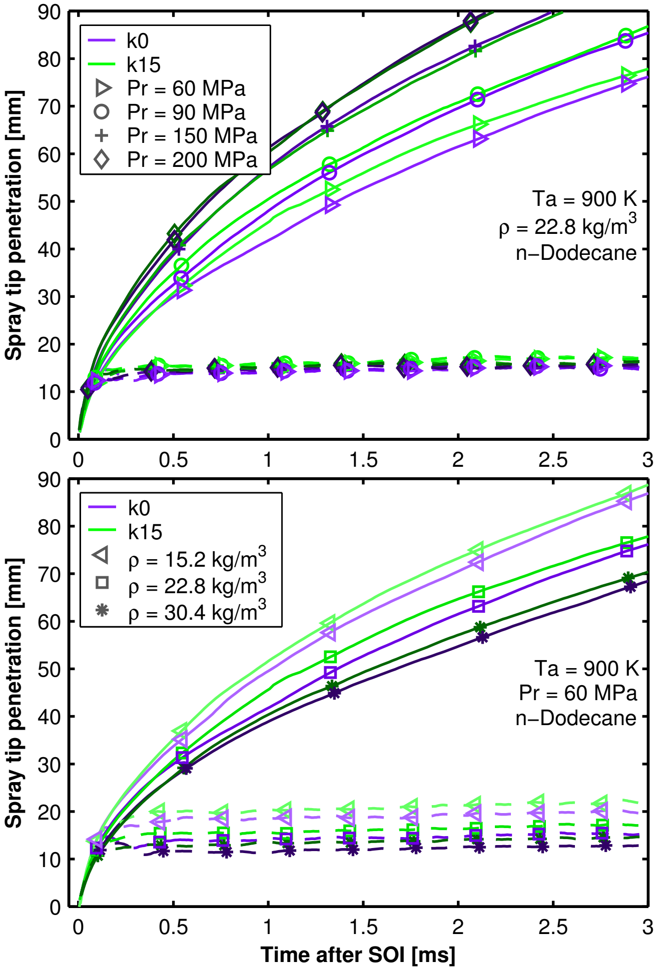

Figure 5.6: The effect of nozzle geometry on spray tip penetration for different rail pressures at an ambient density of 22.8 kg/m^3 (top), and different ambient densities at a rail pressure of 60.0 MPa (bottom). In this case, the fuel presented is n-dodecane and the ambient temperature is 900 K.

Figures 5.6, 5.7 and 5.8 show subsets of the full test matrix results obtained from the experiments. The effect of injection pressure (top of each figure), and ambient density (bottom of each figure) on spray development are shown for the two different nozzles. The different test conditions are indicated by symbols.

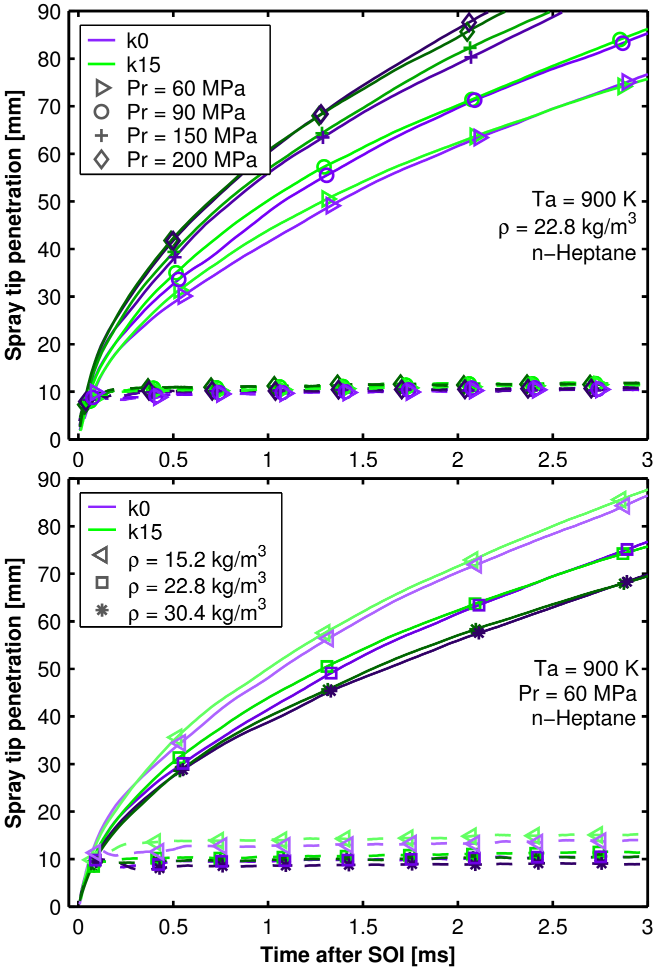

Figure 5.7: The effect of nozzle geometry on spray tip penetration for different rail pressures at an ambient density of 22.8 kg/m^3 (top), and different ambient densities at a rail pressure of 60.0 MPa (bottom). In this case, the fuel presented is n-heptane and the ambient temperature is 900 K.

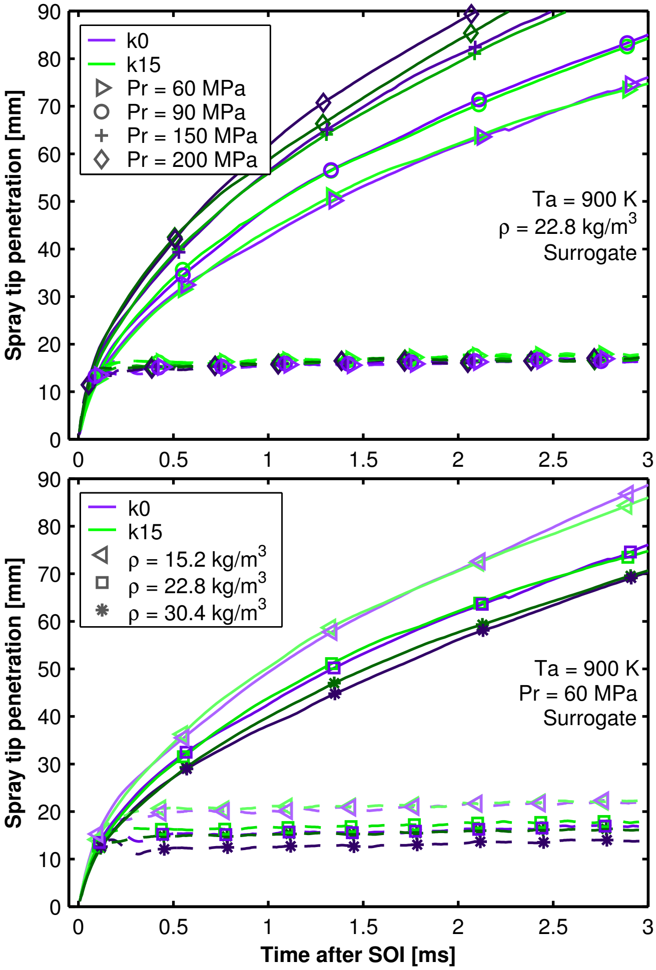

Figure 5.8: The effect of nozzle geometry on spray tip penetration for different rail pressures at an ambient density of 22.8 kg/m^3 (top), and different ambient densities at a rail pressure of 60.0 MPa (bottom). In this case, the fuel presented is the Surrogate and the ambient temperature is 900 K.

Overall, in spite of lower mass flow rate and momentum flux [6], the conical nozzle *k15* shows faster tip penetration rates in the later stages of the spray development (in average, time >0.5 ms in Figures 5.6, 5.7 and 5.8) when compared to the cylindrical nozzle *k0*. This occurs because of the turbulent velocity profiles produced by the cylindrical nozzle [20], that enhance spray mixing and momentum exchange which in turn leads to slower tip penetration. Therefore, at higher rail pressures (top sides of Figures 5.6, 5.7 and 5.8), where the effect of aerodynamic drag loses importance, the difference in the penetration of sprays produced by the two nozzles is reduced. This is also due to the increasingly higher momentum flux from nozzle *k0* at higher rail pressures in comparison to nozzle *k15* [6]. Consequently, the low injection pressure case shown in the bottom parts of Figures 5.6, 5.7 and 5.8 for all densities, marks a clear difference between the penetration rate of the two nozzles, with *k15* being consistently the faster of the two. These conditions allow time for the aerodynamic interactions to develop, and turbulent velocity profiles in the outlet orifice become more important to the gas entrainment process. The higher turbulence at the outlet of the cylindrical orifice *k0* enhances liquid phase break-up, smaller droplets evaporate faster and exchange momentum more efficiently with the ambient gas which reduces the liquid length in the stabilized region. For the vapor phase, the turbulence is carried over, enhancing momentum exchange and thus slowing down the spray in comparison to the conical nozzle.

Similar behavior from comparable experiments and conditions for isothermal non-evaporative sprays of the same nozzles and fuels [5, 6] were also reported in chapter 4. The trends presented in those studies were similar to those presented in this chapter for the vapor phase, not only directly comparing nozzles, but also in how the nozzles responded to ambient density and rail pressure. Similar results—comparing nozzles in both liquid and vapor phase sprays—were also reported previously by SOM et al. [21] and MONTANARO et al. [22]. In both studies, authors performed numerical simulations of isothermal and evaporative sprays for cylindrical and conical nozzles, showing that the penetration curves start to diverge after a certain time has passed and aerodynamic interactions have played its part, even though the effect of nozzle geometry is just introduced as boundary conditions at the orifice interface. Note that MONTANARO et al. [22] observed the same trend in their experimental results, presented in the same paper but discussed in detailed further by ZHANG et al. [23].

In the case of the vapor spray, the comparison between nozzles was similar for all fuels. This was not the case for the isothermal non-evaporative sprays studied previously in chapter 4 [6], which suggests that the vapor spray penetration is mainly controlled by momentum and therefore, independent of fuel. This is discussed in detailed in the next section.

Figures 5.6, 5.7 and 5.8 also show the behavior of the liquid phase penetration (dashed lines). The cylindrical nozzle *k0* consistently showed shorter stabilized liquid penetration lengths when compared to the conical nozzle *k15*, throughout the full test matrix. This is attributed to the increased turbulence at the outlet orifice and the consequent larger near-field spreading angle [5, 6]. Figures 5.6, 5.7 and 5.8 also illustrate, once more, how the stabilized liquid lengths are independent of injection pressures but strongly affected by and inversely proportional to ambient density [13].

5.5.3 Comparing fuels

A similar analysis can be carried out comparing fuels. Figures 5.9 and 5.10 present results of the evolution of the spray tip penetration for select test conditions. Overall, the vapor spray tip penetrations observed were similar for all fuels. This is in agreement with the observations of the nozzle comparisons, where both nozzles responded in similar ways to different fuels. This is also in agreement with the observations of KOOK and PICKETT [24], and confirms that the vapor spray tip penetration is independent of the fuel utilized, keeping the rest of the variables constant, since spray momentum is also independent of fuel [6, 24], even though the rate of injection is affected by fuel density [6, 25]. The top parts of Figures 5.9 and 5.10 confirm, once again, how the liquid length is independent of injection pressure, while the bottom parts show the liquid lengths are inversely proportional to ambient density, as expected [13].

Regarding fuels, n-heptane showed the shortest liquid lengths, followed by n-dodecane, with the Surrogate fuel consistently featuring longer liquid lengths. The stabilized liquid length is determined by the axial location at which the liquid spray has entrained the necessary energy to fully evaporate [13]. This in turn is dictated by the density and boiling point of the fuel along with the spreading angle of the spray. n-Heptane features the lowest density and boiling point of the three fuels. The difference in spreading angle between fuels is not large enough to significantly affect the hot gas energy entrainment, even though n-heptane appears to penetrate slightly slower in the vapor penetration curves. The influence of more specific fuel properties over the stabilized liquid length is analyzed further in section 5.7.

5.6 Spray spreading angle

The spray tip penetration is closely related to the spray spreading angle [5, 6]. Larger spreading angles imply more momentum exchange with the ambient gas which, in turn, renders slower spray tip penetration rates downstream. Figures

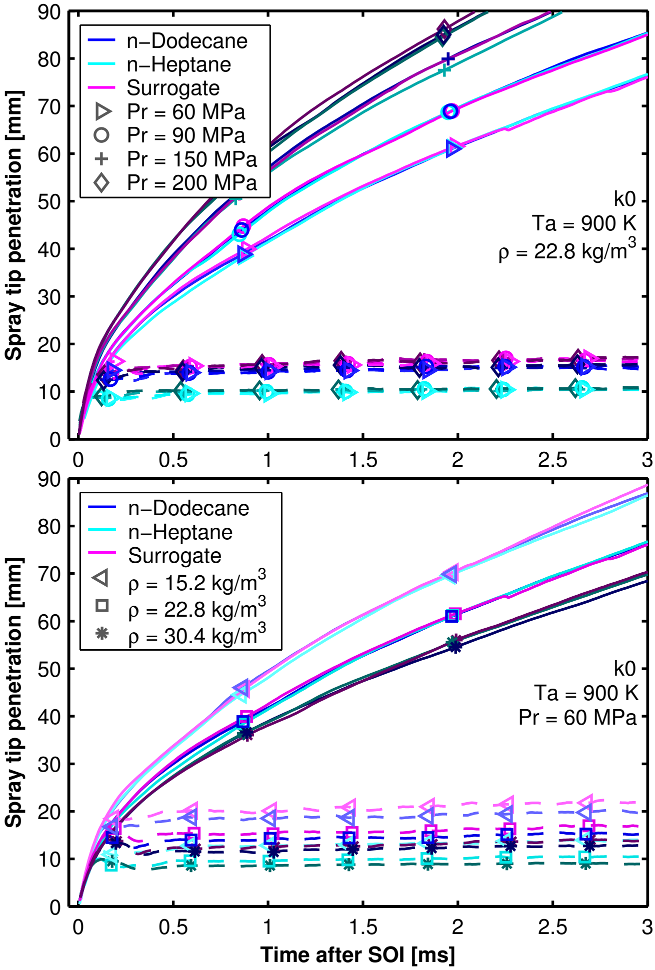

Figure 5.9: Spray tip penetration for all fuels and different rail pressures at an ambient density of 22.8 kg/m^3 (top), and different ambient densities at a rail pressure of 60.0 MPa (bottom). In this case, the nozzle is k0 *and the ambient temperature is 900 K.*

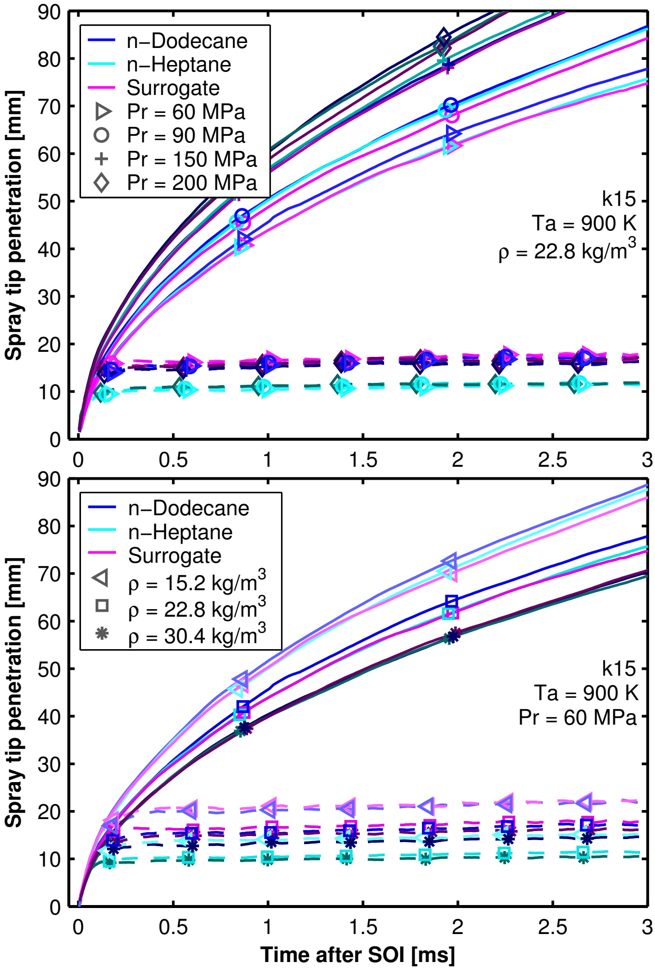

Figure 5.10: Spray tip penetration for all fuels and different rail pressures at an ambient density of 22.8 kg/m^3 (top), and different ambient densities at a rail pressure of 60.0 MPa (bottom). In this case, the nozzle is k15 *and the ambient temperature is 900 K.*

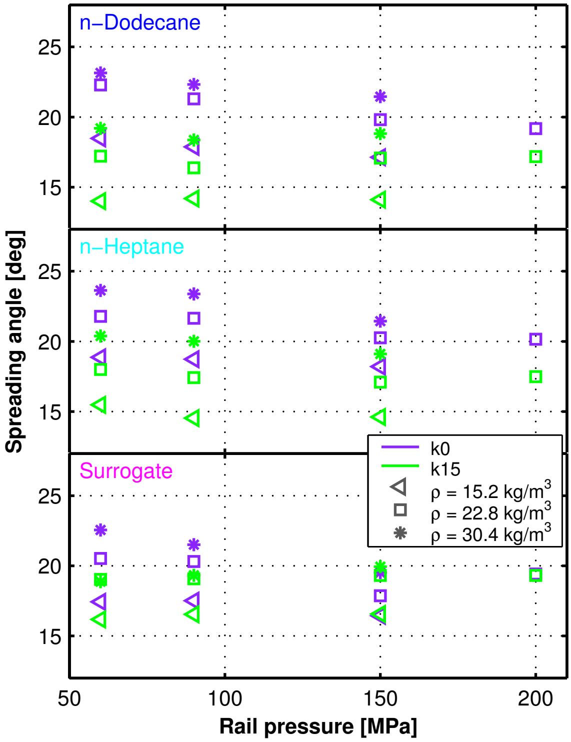

Figure 5.11: Time-averaged spray spreading angles for all test conditions at 900 K.

5.6, 5.7 and 5.8 showed that the sprays produced by the cylindrical nozzle penetrate slower when compared to those produced by the conical nozzle, so larger spreading angles should be expected for the former. Figure 5.11 shows a scatter of vapor spray spreading angle values for all test conditions at 900 K. The spreading angle reported is the angle included between two linear fits performed to the top and bottom halves of the detected spray contour located within 3.6 mm and 15 mm axially measured from the nozzle tip (see Figure 5.3 for an illustration of the angle estimation). The lines fitted are forced to pass through the nozzle outlet. Angle signals from all repetitions are then averaged in the stabilized region of the injection event, from 1 ms to 3 ms after SOI, to obtain a single value per test in order to make comparisons for analysis.

The spreading angle was not found to be significantly affected by the rail pressure, as seen in chapter 4—published in [5, 6]—and also found in the literature [26, 27]. Increasing ambient density, on the other hand, increases spreading angle accordingly. Still, the effect of the nozzle geometry was found to be as significant as the effect of ambient density, with the cylindrical nozzle *k0* showing larger spreading angles along the full test matrix. This result is in line with the previous findings. Moreover, note how fuels do not seem to show clear trends affecting the spreading angle. This is in agreement with the gas jet theory, but contradicts the behavior reported in chapter 4, where n-heptane showed larger spreading angles through the test matrix due to its lower density, viscosity and surface tension. The results of the present study put together with those expounded in chapter 4 for the same nozzles and fuels mark a clear difference between the liquid isothermal non-evaporative spray and the vapor spray.

Even though Figure 5.11 only presents spreading angle results for ambient temperatures of 900 K, the trends found were similar at 800 K and 970 K. All data are available for download at: `http://www.cmt.upv.es/DD01.aspx`.

5.7 Liquid penetration length for different nozzles and fuels

From all time-resolved liquid penetration signals, a time-averaged single value can be extracted to synthesize the liquid length response to the different variables tested into simpler information. From this point forward, all liquid length values presented correspond to those obtained by averaging the liquid penetration signals from 1 ms to 3 ms after SOI. Note that temperatures and densities plotted are not the nominal set points but instead measurements or estimations from the actual during-test conditions.

Figure 5.12 displays a select group of liquid length values for all nozzles and fuels along an ambient temperature sweep, at the central ambient density of 22.8 kg/m^3 and the two limits of rail pressure tested: 60 MPa and 200 MPa. As expected, liquid lengths are inversely proportional to ambient temperature [13], because the hotter ambient gas entrained provides more energy for the vaporization of a given mass of fuel. The cylindrical nozzle *k0* features shorter liquid lengths through the full test matrix, but its effect on liquid length is reduced with increasing injection pressure, as shown by Figure 5.12-top and bottom respectively. This could be explained by the observations of vapor spray tip penetration presented in section 5.5.2 (see Figures 5.6, 5.7 and 5.8), where the effect of nozzle geometry on spray penetration is more important at lower rail pressures because of the longer time needed for the fuel to reach a certain penetration length, and because of the smaller quantity of gas entrained, when compared to very high rail pressure cases. The smaller quantity of gas entrained makes the nozzle outlet conditions more relevant to the momentum exchange, and the longer time needed to reach a certain penetration length allow for the momentum exchange to be amplified by the turbulent velocity profiles at the nozzle outlet, which consequently renders shorter liquid lengths for the cylindrical nozzle *k0*. Note that similar observations—regarding the effect of nozzle geometry and rail pressure over the spray development—were reported in chapter 4 [6].

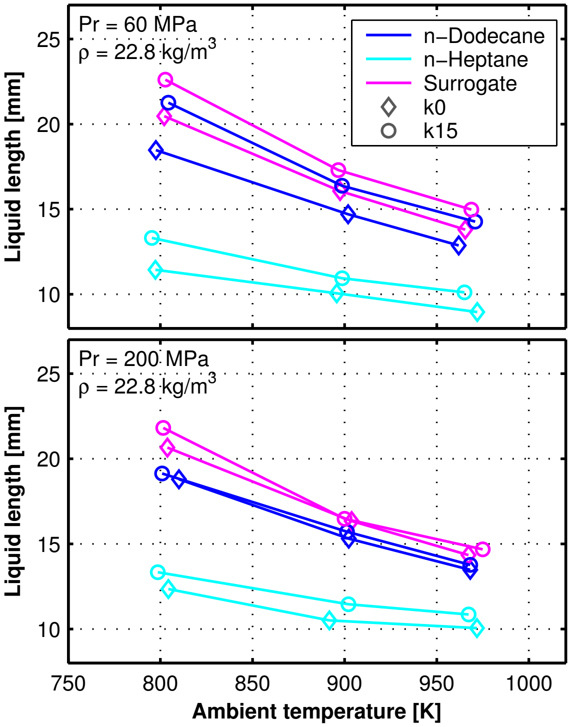

Figure 5.12: Time-averaged liquid length values for all nozzles and fuels along an ambient temperature sweep.

Figure 5.12 also shows a clear separation between the liquid lengths produced by the three fuels tested. In similar conditions, n-heptane produces sprays with considerably shorter liquid lengths than n-dodecane, which at the same time renders shorter liquid lengths than the Surrogate fuel. This was already depicted in Figures 5.4, 5.9 and 5.10 for particular test conditions, synthesized here for a larger data set and is also seen in Figure 5.13 for different ambient densities. The main drivers of these trends are the thermodynamic properties and density of each fuel, with n-heptane featuring lower density and boiling point than n-dodecane and all components of the Surrogate fuel. These results agree with the literature: the liquid length of the Surrogate fuel is controlled by its heavier components, and thus, it results longer than the liquid length of n-dodecane [13, 17, 28], even though the Surrogate starts to evaporate earlier at atmospheric conditions.

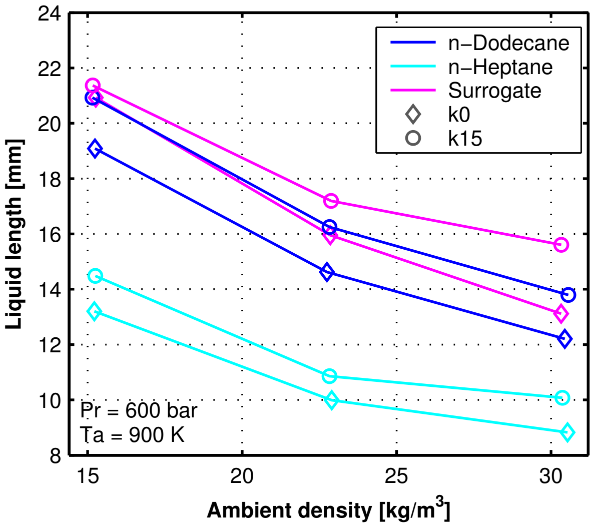

Figure 5.13: Time-averaged liquid length values for all nozzles and fuels along an ambient density sweep.

The effect of ambient density is synthesized in Figure 5.13. As expected, liquid lengths are inversely proportional to ambient density [13]. Note that the trends for nozzle geometry and fuel effects remain, as already discussed.

Properly predicting liquid lengths is of great interest for combustion chamber development. SIEBERS [28] presented a scaling law based in the fundamental physical processes that take place in the evaporative spray, allowing for fast predictions of liquid length for single-component fuels. HIGGINS et al. [17] proposed an alternative model which considers multi-component fuels, through basic thermodynamic properties of each component at reference conditions:

$$x_{liq} = kA^{\alpha}B^{\beta}d_o \tag{5.2}$$

Where k is a proportioning constant, $A = \rho_f/\rho$ is the density ratio, and B is the specific energy ratio, calculated as:

$$B = \frac{\sum_{i=1}^{N} Y_i h_{vap,i} + (T_{b,max} - T_f)\sum_{i=1}^{N} Y_i C_{p,liq,i}}{C_{p,air}(T_a - T_{b,max})\sum_{i=1}^{N} Y_i} \tag{5.3}$$

Where $T_{b,max}$ is the maximum T_b among the N species and Y_i is the mass fraction of species i. Note that A and B are evaluated using the atmospheric properties of the fuel, which is very convenient. Fuel properties utilized for the evaluation of the A and B terms are summarized in Tables 2.2 and 2.3. Fuel temperature at the outlet orifice was estimated from the data collected previously by Payri et al. [2]. Higgins et al. [17] proposed values for k, α and β but these not necessarily apply for any nozzle, fuel, and/or outside the test conditions covered. Moreover, this model would not predict properly the effect of nozzle geometry. The effect of nozzle geometry could be included by introducing the effective diameter instead of the nominal diameter ($d_{eff} = d_o\sqrt{C_a}$), so Eq. (5.2) can be re-written:

$$x_{liq} = kA^{\alpha}B^{\beta}d_o\sqrt{C_a} \tag{5.4}$$

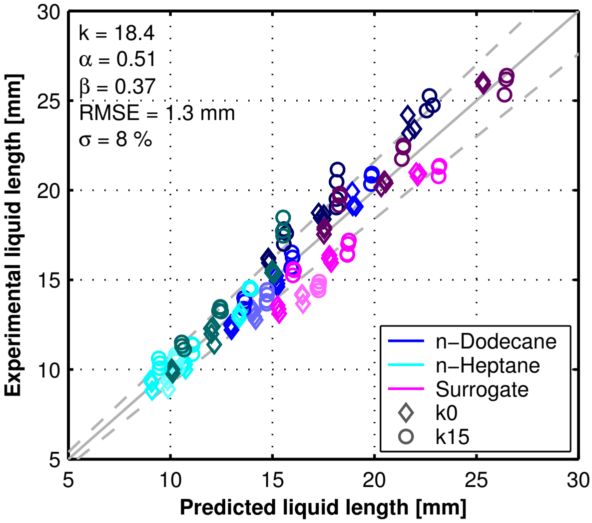

Figure 5.14: Non-linear regression of the model originally presented by Higgins et al. [17], modified to include the effect of nozzle geometry, presented in Eq. (5.4). Dashed lines represent $\pm\sigma$.

Where C_a is the area coefficient, previously measured or all nozzles and fuels and presented in chapter 3 [6]. This model was employed to predict all liquid length values measured, and the results are presented in Figure 5.14. In this figure, nozzles are denoted by symbols while fuels are distinguished by color. Each color is shaded so that ambient temperatures are differentiable, if such is the intent of the reader. The regression coefficients are shown in the top-left corner of the figure, along with the root-mean-square error (RMSE) of the fit. Note how the effect of ambient density is very well captured, with $\alpha = 0.51$ when mixing-limited models predict a value of 0.5 [28]. Considering how little data is needed to use Eq. (5.4) for these fast liquid length predictions, these are acceptable results, with the RMSE low at 1.3 mm. However, Figure 5.14 demonstrates that even though the effect of nozzle geometry is partially captured by the model, there is still an offset from the main diagonal when comparing nozzles at equal conditions. Hence, Eq. (5.4) can be modified further by introducing vapor spray spreading angles (presented in Figure 5.11):

$$x_{liq} = kd_o\sqrt{C_a}A^{\alpha}B^{\beta}\tan^{\phi}(\theta/2) \tag{5.5}$$

For this regression, the coefficient defining the effect of ambient density (α) was fixed to 0.5 to comply with the mixing-limited evaporative spray theory [28] and reduce the degrees of freedom of the regression. The results from this non-linear fit are presented in Figure 5.15. Note that the coefficient for the spreading angle results negative, which is expected since larger angles would produce shorter liquid lengths. Note also that the β coefficient remains the same as in the previous model, but now the effect of nozzle geometry is captured better, which then reduces the RMSE. Still, the behavior of the Surrogate is not completely well captured by the model, even though this fuel is the original reason why the model was implemented. Fuel properties in Tables 2.2 and 2.3 indicate that all fuels tested in this study feature comparable specific heats and enthalpies of vaporization. The significant differences between fuels are actually the boiling points. HIGGINS et al. [17] demonstrated that considering only T_{90}—or simply, the boiling point for single-component fuels—may not be an appropriate approach for some fuels, for instance, methanol. Alcohols in general feature considerably larger enthalpies of vaporization than hydrocarbons [17, 29], which means that, even though their boiling points may be lower, complete evaporation requires far more energy entrained into the spray, which translates into longer length scales [17, 29]. However, HIGGINS et al. [17] also observed a good correlation between predicted liquid lengths and T_{90} for a large group of other fuels. In the case of this study, considering fuel properties in Tables 2.2 and 2.3 and that all fuels are hydrocarbons, it would be reasonable to think that even a simpler model would be equally suited to properly predict liquid lengths.

$$x_{liq} = kd_o\sqrt{C_a}A^{\alpha}T_a^{b}T_{90}^{c}tan^{\phi}(\theta/2) \tag{5.6}$$

A simpler model is presented in Eq. (5.6). This engineering correlation separates the contributions of T_{90} and T_a into two degrees of freedom. Once more, the coefficient for the density ratio A was fixed to 0.5. The regression coefficient for

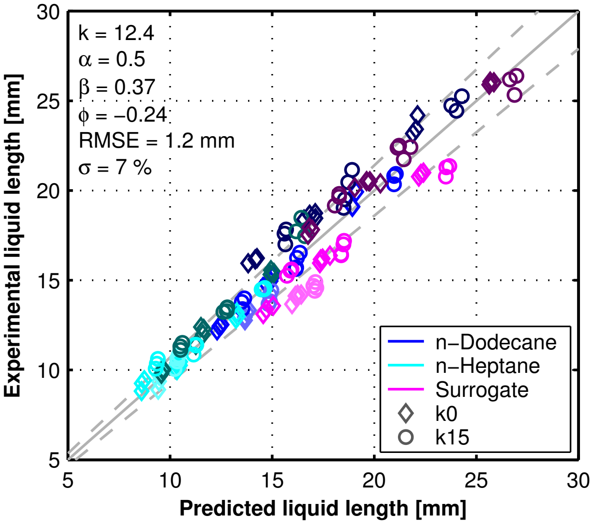

Figure 5.15: Non-linear regression of the model originally presented by Higgins *et al. [17], modified to include the effect of nozzle geometry and vapor spray spreading angle, presented in Eq. (5.5). Dashed lines represent* $\pm\sigma$.

the spreading angle (ϕ) resulted in a value relatively close to the value obtained for the model presented in Eq. (5.5). Note also that the relationship between the predicted liquid length and T_{90} is practically linear, and that liquid length is inversely proportional to the ambient temperature squared. This model, even though simpler, results more suitable for the case of study since it captures better the behavior of the different fuels, while still reproducing reasonably the effect of nozzle geometry. The new model (eq. 5.6) predicts an RMSE of 0.6 mm instead of 1.2 mm of the model presented in eq. 5.5 based on the specific energy ratio.

5.8 Spray boundary fluctuations

Payri et al. [5] presented line-of-sight fluctuation maps of the detected spray boundaries, which clearly marked differences between the cylindrical and conical nozzle for liquid non-evaporative isothermal n-dodecane sprays. Later, Payri et al. [6] presented similar maps for the same non-evaporative sprays, but then showing also the three fuels tested in this study. These maps illustrated how the cylindrical nozzle widens the liquid spray immediately after the fuel has exited the orifice, while the spray produced by the conical nozzle spreads more progressively downstream. Spray boundary fluctuations were also found to be greater for the

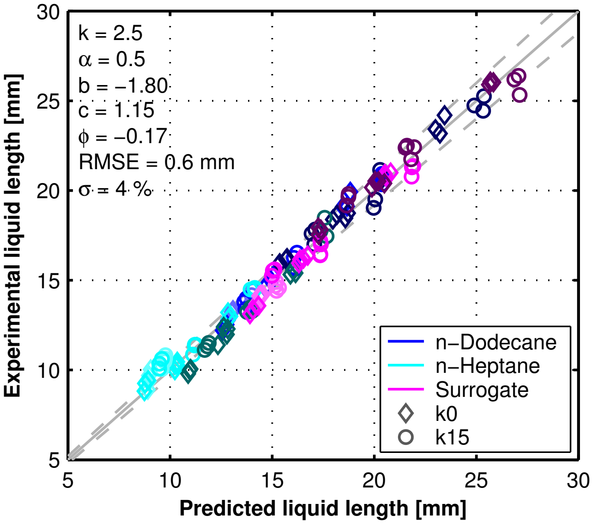

Figure 5.16: Results of the non-linear regression of the engineering correlation presented in Eq. (5.6). Dashed lines represent $\pm\sigma$.

cylindrical nozzle. Moreover, these maps showed that the liquid non-evaporative isothermal n-heptane spray featured larger spreading angle and fluctuations in the boundary region, followed by the Surrogate spray. This section discusses analogous maps which are constructed from the spray boundaries of the liquid and vapor phases separately detected, to asses if the conclusions drawn from the liquid non-evaporative isothermal sprays are carried on to hot evaporative sprays.

Figure 5.17 shows line-of-sight fluctuation maps of liquid sprays produced by the two nozzles and three fuels at a particular case of test conditions. Each map is calculated as the standard deviation between all binary images of the detected sprays from the corresponding test. This calculation is done past 0.5 ms after SOI to guarantee that the spray is in steady state. Therefore, a black pixel corresponds to a non-fluctuating location: the spray never occupies that pixel or the pixel is always considered to be within the spray during the time window considered. On the other hand, the brighter a pixel is, the more likely it is for fluctuations to occur at that location (and/or the stronger fluctuations at that location are) and, as expected, this happens near the spray boundary.

The first important observation that Figure 5.17 provides is that the spray produced by the cylindrical nozzle *k0* spreads immediately after the fuel has exited the orifice, while the spray produced by nozzle *k15* starts thin and spreads progressively downstream, as previously seen in non-evaporative isothermal sprays

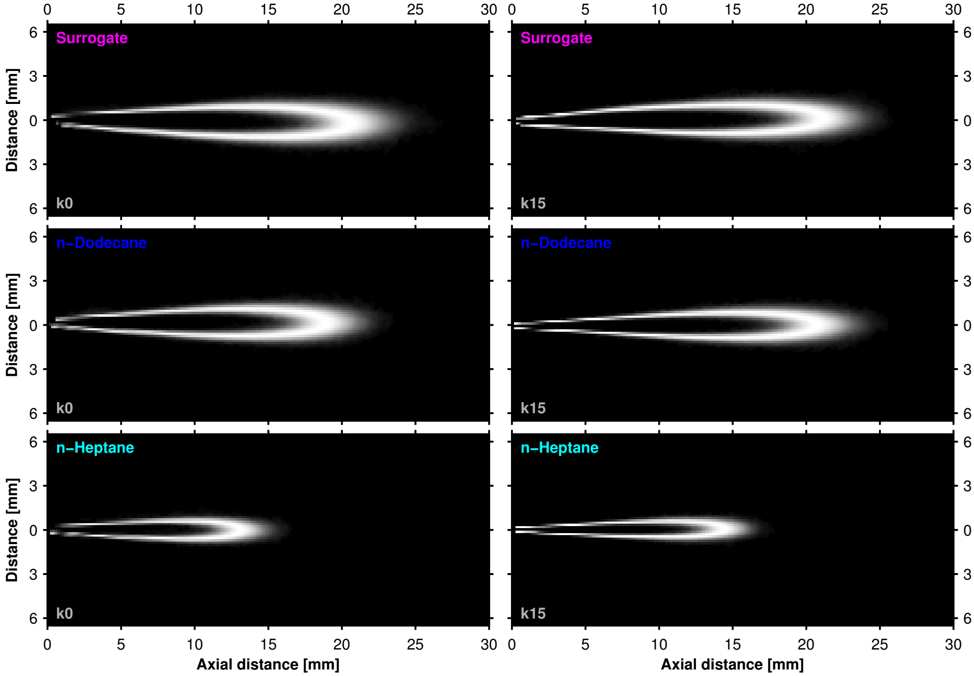

Figure 5.17: Liquid spray fluctuation maps for all nozzles and fuels at a rail pressure of 60.0 MPa, an ambient density of 15.2 kg/m^3, and an ambient temperature of 900 K. Maps comprise all test repetitions and images from 0.5 ms after SOI to the end of the signals.

[5, 6]. This implies that the nozzle geometry has great effect on what BENAJES et al. [30] refer to as transitional length, which is the region after the intact liquid core starts to break but before the spray starts its linear evolution. Furthermore, fluctuation maps for *k0* are more diffuse in the radial direction, which indicates larger fluctuations, that were also seen in the non-evaporative isothermal case presented in chapter 4. Since the evaporative sprays are small relative to the spatial resolution achieved, no important differences could be observed between fuels in terms of fluctuations as presented here.

Still, observing these two-dimensional maps directly complicates the direct comparison between nozzles. If these maps are integrated from 1 mm to 9 mm along the spray axis, a quantitative measurements of the fluctuation strength and area can be synthesized into a single value—which will be referred to as "fluctuation power"—per test condition, nozzle and fuel [5]. Note that the integration excludes the tip region, in order to exclude fluctuations in the liquid length, which are out of the scope of this research [31]. Liquid spray fluctuation power values are displayed in Figure 5.18 for all nozzles and fuels at an ambient temperature of 900 K. PAYRI et al. [5] presented and similar analysis for non-evaporative isothermal sprays, showing that fluctuation power was directly proportional to ambient density, due to the increased turbulence and momentum exchange, and that the cylindrical nozzle featured larger values at equal injection conditions. In the case of evaporative sprays, larger ambient densities are translated into smaller liquid sprays, so fluctuation power values are slightly reduced due to the decrease in line-of-sight area in the radial direction. Still, Figure 5.18 shows that, generally, fluctuation power values are scaled with ambient density, similarly to the non-evaporative isothermal case, even though the higher ambient density sprays are smaller in projected area. Also, the cylindrical nozzle *k0* features larger fluctuation power values all through the test matrix when compared to the conical nozzle *k15* at equal test conditions, which results from a combination of the wider spray produced and a more diffuse fluctuation map. Note that the effect of ambient density over each fuel is not constant. The Surrogate fuel liquid spray seems to be less affected by changes in ambient density, which could be related to its higher density, viscosity and surface tension, all of which help the liquid droplets to conserve momentum. n-Heptane, on the other hand, seems to be more affected by changes in ambient density, with n-dodecane in the middle between fuels, which agrees with the non-evaporative isothermal spray results presented in chapter 4.

A similar analysis can be carried out for the vapor phase, which should agree with the penetration and spreading angle observations already presented, as was the case for non-evaporative isothermal sprays [6]. Line-of-sight fluctuation maps of vapor sprays are shown in Figure 5.19 for all nozzles and fuels at a particular case of test conditions. Plots in the left column demonstrate that the cylindrical nozzle *k0* produces vapor sprays which spread immediately after exiting the orifice, while the conical nozzle produces a thin jet that spreads more progressively downstream, which again suggests that the nozzle geometry is affecting the transitional length [30]. Note that this result is in agreement with the findings for the liquid phase reported here, and those found for non-evaporative isothermal sprays analyzed in chapter 4. As in the liquid phase case, the cylindrical nozzle *k0* produces not only wider sprays but also more diffuse fluctuation maps, which indicates larger fluctuations in the line-of-sight spray boundaries detected. The vapor phase fluctuation maps are not as diffuse—statistically evenly distributed—near the spray boundary as the liquid phase maps or those presented in chapter 4, due to the lower frame rate of the camera in this particular setup, which translates into a smaller total number of frames from which to extract the maps.

Analogous to the liquid phase case, these maps can be integrated from 3.6 mm to 50 mm along the spray axis to synthesize part of these maps into a single fluctuation power value per test conditions. Note that 3.6 mm is selected as the lower

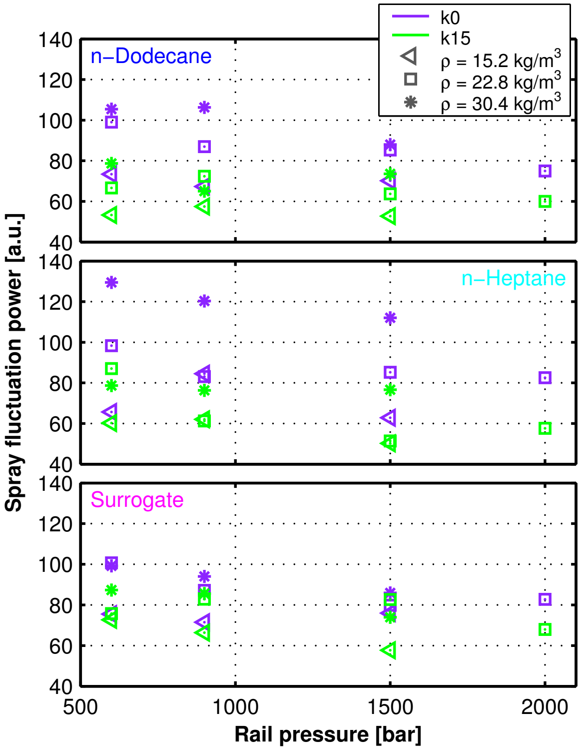

Figure 5.18: Liquid spray fluctuation power from 1 mm to 9 mm along the spray axis, at an ambient temperature of 900 K.

limit since it is the same limit used for the calculation of the vapor spray spreading angles depicted in Figure 5.11. Vapor spray fluctuation power values are presented in Figure 5.20 for all nozzles and fuels at an ambient temperature of 900 K. In general, fluctuation power values for the vapor spray are also scaled with ambient density, and remain larger for the cylindrical nozzle *k0* when compared to the conical nozzle *k15*. In contrast to the liquid phase results in Figure 5.18, the different fuels were not found to respond in significantly different ways—in terms of fluctuations—to changes in ambient density, which is in agreement with the spray tip penetration observations for evaporative sprays presented in this study. Again, this was not the case for the non-evaporative isothermal sprays presented in chapter 4.

Observations summarized in this study, along with previous conclusions gathered for the same nozzles and fuels in chapter 4 suggest that the vapor spray is indeed controlled by momentum and turbulence conditions at the nozzle outlet—

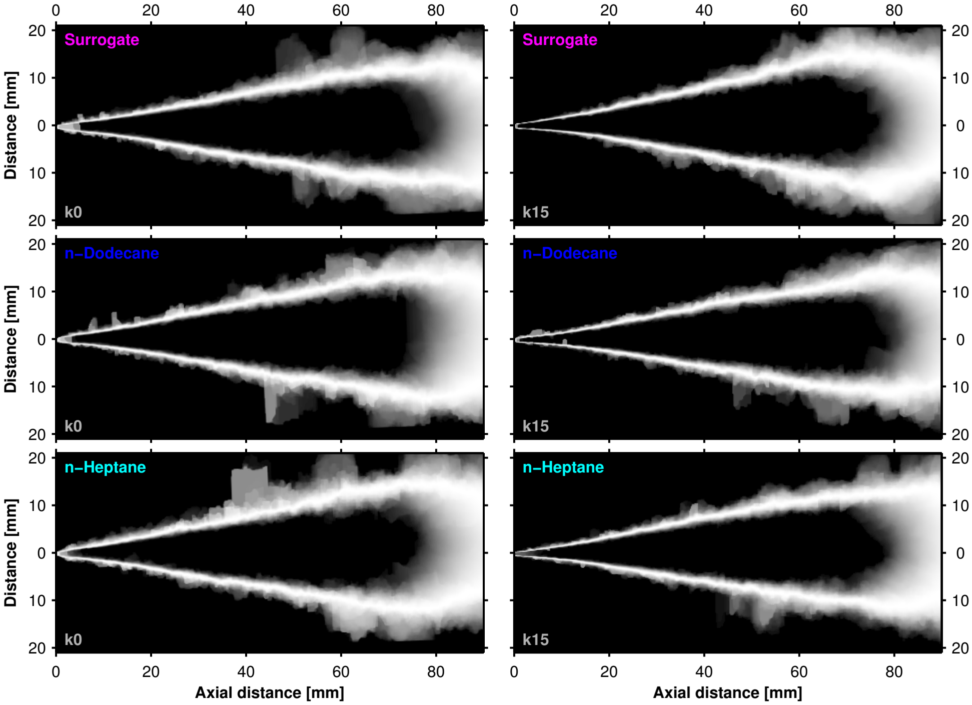

Figure 5.19: Vapor spray fluctuation maps for all nozzles and fuels at a rail pressure of 60.0 MPa, an ambient density of 15.2 kg/m^3, and an ambient temperature of 900 K. The maps comprise all test repetitions and images from 2.5 ms after SOI to the end of the injections.

strongly dictated by nozzle geometry—but the interactions between the vapor phase of the spray and the ambient gas are not strongly affected by fuel properties, which was not found to be the case for the liquid phase spray in both the evaporative case presented here, and the non-evaporative isothermal case presented in chapter 4.

5.9 Conclusions

The influence of internal nozzle flow characteristics over the evaporative spray development is studied experimentally [32]. The macroscopic spray characteristics are obtained by imaging the liquid and vapor phases of the spray simultaneously using independent cameras and optical techniques, and the results are reported in this work. The liquid phase is captured by a fast-pulsed diffused back illumi-

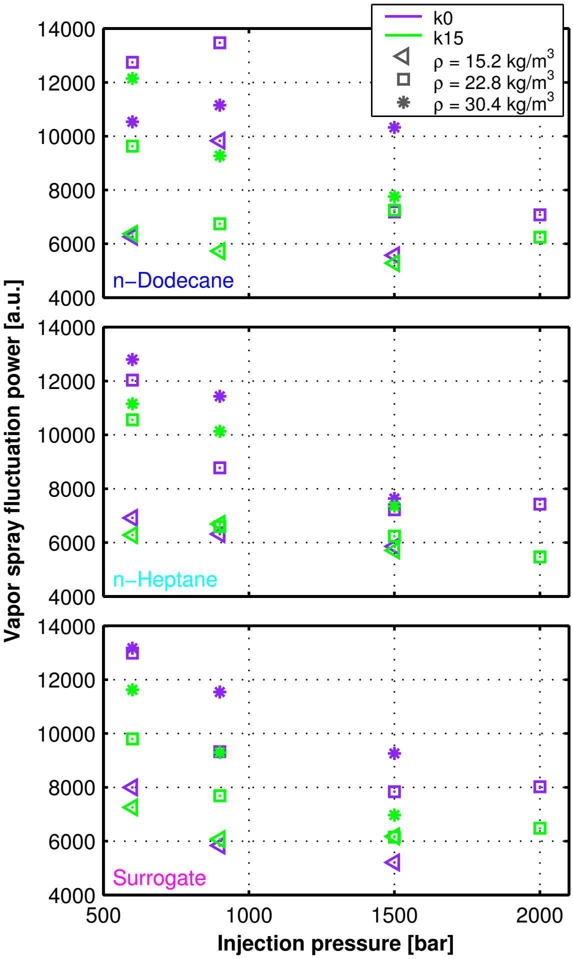

Figure 5.20: Vapor spray fluctuation power from 3.6 mm to 50 mm along the spray axis, at an ambient temperature of 900 K.

nation setup, while the vapor phase is captured by a single-pass Schlieren setup with diaphragm.

For a fixed ambient density, the liquid penetration is controlled by the available energy for vaporization (mainly ambient temperature and ambient density) while the vapor penetration is controlled by momentum (mainly rail pressure and ambient density). The cylindrical nozzle, in spite of higher mass flow rate and momentum flux, shows slower vapor spray tip penetration when compared to the conical nozzle. Also, the cylindrical nozzle consistently produced shorter liquid lengths. The vapor spray spreading angle is found to be inversely proportional to the spray tip penetration, largely influenced by the nozzle geometry and the ambient density. n-Heptane spray shows the shortest liquid lengths, followed by n-dodecane and finally the Surrogate. However, no significant difference in vapor penetration rates was found between fuels, confirming that the vapor spray is controlled by momentum, which is independent of fuel. This was not the case for the non-evaporative isothermal sprays previously studied in chapter 4. Liquid lengths show the expected responses to parametric variations of ambient temperature and density. Two empirical predictive models are presented and utilized to analyze the influence of fuel properties on the liquid length. The primary factor controlling the liquid length between fuels is found to be their volatility. Finally, the cylindrical nozzle exhibits larger line-of-sight contour fluctuations in both the liquid and vapor phases, which in turn contributes to the shorter liquid lengths and slower vapor penetration.

The experimental findings from this work on the macroscopic spray behavior, and the large database obtained (available for download at: `http://www.cmt.upv.es/DD01.aspx`), could be used to validate CFD models that might help the community understand the fundamental driving mechanisms behind these observations.

References

[1] PICKETT, L. M., MANIN, J., GENZALE, C. L., SIEBERS, D. L., MUSCULUS, M. P. B., and IDICHERIA, C. A. “Relationship Between Diesel Fuel Spray Vapor Penetration/Dispersion and Local Fuel Mixture Fraction”. *SAE International Journal of Engines* 4.1 (2011), pp. 764–799.

[2] PAYRI, R., GARCÍA-OLIVER, J. M., BARDI, M., MANIN, J., GARCIA-OLIVER, J. M., BARDI, M., and MANIN, J. “Fuel temperature influence on diesel sprays in inert and reacting conditions”. *Applied Thermal Engineering* 35.March (Mar. 2012), pp. 185–195.

[3] MANIN, J., BARDI, M., and PICKETT, L. M. "Evaluation of the liquid length via diffused back-illumination imaging in vaporizing diesel sprays". *Comodia*. Fukuoka, 2012.

[4] PICKETT, L. M., GENZALE, C. L., and MANIN, J. "Uncertainty quantification for liquid penetration of evaporating sprays at diesel-like conditions". *Atomization and Sprays* 25.5 (2015), pp. 425–452.

[5] PAYRI, R., SALVADOR, F. J., GIMENO, J., and VIERA, J. P. "Experimental analysis on the influence of nozzle geometry over the dispersion of liquid n-dodecane sprays". *Frontiers in Mechanical Engineering* 1 (2015), pp. 1–10.

[6] PAYRI, R., VIERA, J. P., GOPALAKRISHNAN, V., and SZYMKOWICZ, P. G. "The effect of nozzle geometry over internal flow and spray formation for three different fuels". *Fuel* 183 (Nov. 2016), pp. 20–33.

[7] JUNG, Y., MANIN, J., SKEEN, S. A., and PICKETT, L. M. "Measurement of Liquid and Vapor Penetration of Diesel Sprays with a Variation in Spreading Angle". *SAE Technical Paper 2015-01-0946* (2015).

[8] BARDI, M., PAYRI, R., MALBEC, L. M., BRUNEAUX, G., PICKETT, L. M., MANIN, J., BAZYN, T., and GENZALE, C. L. "Engine Combustion Network: Comparison of Spray Development, Vaporization, and Combustion in Different Combustion Vessels". *Atomization and Sprays* 22.10 (2012), pp. 807–842.

[9] FANSLER, T. D. and PARRISH, S. E. "Spray measurement technology: a review". *Measurement Science and Technology* 26.1 (Jan. 2015), p. 012002.

[10] PAYRI, R., GIMENO, J., VIERA, J. P., and PLAZAS, A. H. "Needle lift profile influence on the vapor phase penetration for a prototype diesel direct acting piezoelectric injector". *Fuel* 113 (2013), pp. 257–265.

[11] BENAJES, J., PAYRI, R., BARDI, M., and MARTÍ-ALDARAVÍ, P. "Experimental characterization of diesel ignition and lift-off length using a single-hole ECN injector". *Applied Thermal Engineering* 58.1-2 (2013), pp. 554–563.

[12] PAYRI, R., VIERA, J. P., PEI, Y., and SOM, S. "Experimental and numerical study of lift-off length and ignition delay of a two-component diesel surrogate". *Fuel* 158 (2015), pp. 957–967.

[13] SIEBERS, D. L. "Liquid-phase fuel penetration in diesel sprays". *SAE Paper 980809* (1998).

[14] NING, W., REITZ, R. D., DIWAKAR, R., and LIPPERT, A. M. "An eulerian-lagrangian spray and atomization model with improved turbulence modeling". *Atomization and Sprays* 19.8 (2009), pp. 727–739.

[15] WANG, Y., QIU, L., REITZ, R. D., and DIWAKAR, R. "Simulating cavitating liquid jets using a compressible and equilibrium two-phase flow solver". *International Journal of Multiphase Flow* 63 (2014), pp. 52–67.

[16] IDICHERIA, C. A. and PICKETT, L. M. "Soot formation in Diesel combustion under high-EGR conditions". *SAE Technical Paper 2005-01-3834* (2005).

[17] HIGGINS, B. S., MUELLER, C. J., and SIEBERS, D. L. "Measurements of fuel effects on liquid-phase penetration in DI sprays". *SAE transactions* 108.724 (1999), pp. 630–643.

[18] PAYRI, R., GIMENO, J., VIERA, J. P., and PLAZAS, A. H. "Schlieren visualization of transient vapor penetration and spreading angle of a prototype diesel direct-acting piezoelectric injector". *ICLASS 2012*. 2012, pp. 1–8.

[19] PAYRI, R., GIMENO, J., BRACHO, G., and VAQUERIZO, D. "Study of liquid and vapor phase behavior on Diesel sprays for heavy duty engine nozzles". *Applied Thermal Engineering* 107 (2016), pp. 365–378.

[20] SUN, Z.-Y., LI, G.-X., CHEN, C., YU, Y.-S., and GAO, G.-X. "Numerical investigation on effects of nozzle's geometric parameters on the flow and the cavitation characteristics within injector's nozzle for a high-pressure common-rail DI diesel engine". *Energy Conversion and Management* 89 (2015), pp. 843–861.

[21] SOM, S., RAMÍREZ, A. I., LONGMAN, D. E., and AGGARWAL, S. K. "Effect of nozzle orifice geometry on spray, combustion, and emission characteristics under diesel engine conditions". *Fuel* 90.3 (2011), pp. 1267–1276.

[22] MONTANARO, A., MIGLIACCIO, M., ALLOCCA, L., FRAIOLI, V., LEE, S.-Y., ZHANG, A., and NABER, J. "Schlieren and Mie Scattering Visualization for Single- Hole Diesel Injector under Vaporizing Conditions with Numerical Validation". *SAE Technical Paper 2014-01-1406* 2014-01-14 (2014).

[23] ZHANG, A., MONTANARO, A., ALLOCCA, L., NABER, J., and LEE, S.-Y. "Measurement of Diesel Spray Formation and Combustion upon Different Nozzle Geometry using Hybrid Imaging Technique". *SAE Technical Paper 2014-01-1410* (2014).

[24] KOOK, S. and PICKETT, L. M. "Liquid length and vapor penetration of conventional , Fischer-Tropsch , coal-derived , and surrogate fuel sprays at high-temperature and high-pressure ambient conditions". *Fuel* 93 (2012), pp. 539–548.

[25] BOUDY, F. and SEERS, P. "Impact of physical properties of biodiesel on the injection process in a common-rail direct injection system". *Energy Conversion and Management* 50.12 (2009), pp. 2905–2912.

[26] DELACOURT, E., DESMET, B., and BESSON, B. "Characterisation of very high pressure Diesel sprays using digital imaging techniques". *Fuel* 84.7-8 (2005), pp. 859–867.

[27] MOHAN, B., YANG, W., TAY, K. L., and YU, W. "Macroscopic spray characterization under high ambient density conditions". *Experimental Thermal and Fluid Science* 59 (2014), pp. 109–117.

[28] SIEBERS, D. L. "Scaling liquid-phase fuel penetration in diesel sprays based on mixing-limited vaporization". *SAE Technical Paper 1999-01-0528* (1999).

[29] REDDEMANN, M. A., MATHIEU, F., MARTIN, D., and KNEER, R. "The Influence of Fuel Properties on Spray Propagation , Atomization and Evaporation". *ILASS 2010*. September. 2010, pp. 1–6.

[30] BENAJES, J., SALVADOR, F. J., CARRERES, M., and JARAMILLO, D. "On the relation between the external structure and the internal characteristics in the near-nozzle field of diesel sprays". *Proceedings of the Institution of Mechanical Engineers, Part D: Journal of Automobile Engineering* (2016).

[31] JOHNSON, J., GE, H.-W., NABER, J., LEE, S.-Y., KURTZ, E., and ROBARGE, N. "Investigation of Key Mechanisms for Liquid Length Fluctuations in Transient Vaporizing Diesel Sprays". *SAE Technical Paper 2013-01-1594* (2013), pp. 1202–1212.

[32] PAYRI, R., VIERA, J. P., GOPALAKRISHNAN, V., and SZYMKOWICZ, P. G. "The effect of nozzle geometry over the evaporative spray formation for three different fuels". *Fuel* 188 (2017), pp. 645–660.

Chapter 6

Reactive spray visualization

This chapter describes the reactive spray visualization experiments and observations. Reactive spray visualization in test chambers seek to reproduce combustion conditions and development that occur inside the engine in a controlled environment. These reactive sprays comprise all physical processes that real in-engine sprays have: liquid fuel is injected into the chamber at high pressure, the liquid core shears and breaks-up while heat transfer occurs, similar to the evaporative inert case. Once the mixture has reached ignitable mixture fraction and temperature, ignition takes place and diffusion combustion develops. The ignition process presents a given delay from the start of injection. Once combustion is stabilized, the flame stabilizes upstream at the lift-off length (LOL, the axial distance from the nozzle tip to the upstream flame front), which is one of the main subjects of analysis in this chapter. Quality data of these processes allows for direct analysis of the mechanisms involved, but also facilitates CFD model validation which can then be used to predict combustion performance and emissions [1].

During all tests described and presented in this chapter, energizing times were fixed at 2500 µs. As described also in chapter 5 for the evaporative experiments, the injector body temperature was maintained close to target using a special injector holder designed to have a coolant flowing at a controlled temperature in direct contact with the injector body [2]. The temperature of the coolant is adjusted in function of the discharge chamber gas temperature and density, to guarantee a constant sac inner wall temperature of approximately 110 °C [2].

6.1 Optical setup

The optical setup, shown in Figure 6.1, consisted of two separate cameras and optical arrangements for the visualization of the reactive spray development and lift-off length. Note that both cameras recorded the same injection events, triggered by the same command signal sent to the injector.

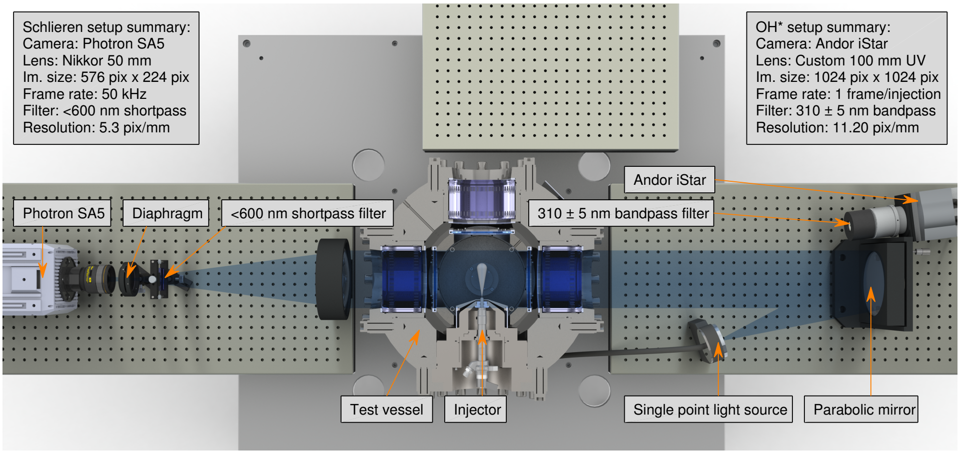

Figure 6.1: Plan view of the optical setup.

Schlieren imaging has been successfully employed several times to identify refractive index gradients in transparent mediums. For vaporizing diesel sprays, this technique is able to capture the line-of-sight boundary between vaporized fuel and ambient gases, as there is an appreciable difference in refractive indices between these [3–5]. Since the rays of light are collimated into a cylindrical beam, small deflections due to refractive index gradients are rendered in the image as shades. In this study, the vapor spray was visualized through a single-pass Schlieren setup [5, 6], which is often applied to axi-symmetrical single hole nozzles. Multi-hole injectors require a two-pass setup and a high temperature mirror as explained by Payri et al. [7, 8]. The final setup is very similar to the setups employed for the CMT experiments in [3, 9–11] and exactly the same setup utilized for the experiments presented in chapter 5 [6]. The camera was a Photron SA5, sampling images of 576 pix × 224 pix at 50 kHz with a spatial resolution of 5.3 pix/mm. This produced a field of view (FOV) along the spray axis of 108 mm, and considering window limits and nozzle location, the maximum penetration length measurable was 96 mm. The exposure time was set to 2.28 µs.

The lift-off length (LOL) was measured capturing the signal from OH* chemiluminescence following the ECN standard methodology [9, 10, 12]. An

ICCD camera (Andor iStar) fitted with a custom 100 mm f/2.8 UV lens and a 310 nm ± 5 nm interferometric filter was used to acquire the chemiluminescence signal. Since this signal is weak, the intensifier of the camera sensor was gated during the steady region of the injection—2.3 ms to 4.8 ms after start of energizing (SOE)—to obtain an on-chip time-averaged signal, minimizing the effect of local turbulent flame behavior. Note that this camera had to be inclined slightly off axis so not to block the collimated Schlieren beam. However, the angle was small at 7°, and the possible effects were accounted for by properly correcting the images. The camera sampled one image per injection event, of 1024 pix × 1024 pix with a spatial resolution of 11.2 pix/mm. This produced a FOV along the spray axis of approximately 90 mm. Further details of the processing algorithm for the LOL estimations can be found in [9, 10].

6.2 Schlieren image processing

Each image is processed using an algorithm that detects the spray boundary and computes its associated properties. The program—similar to what was utilized to process images in the evaporative inert spray visualization presented in chapter 5—consists of two extensively used approaches for the processing of these type of images. Two binarized images are obtained from two different criteria and then merged to maximize sensitivity. The first algorithm was originally developed at Sandia National Laboratories (SNL) and is available for download on the ECN website (`http://www.sandia.gov/ecn/`). The routine detects temporal changes in pixel-wise intensities by taking the temporal derivative of a series of images. This produces a 2D map where pixels with higher intensity represent pixels that are changing their digital values in time. The temporal nature of this algorithm makes it robust to variations between optical setups, and makes it very strong for transparent spray images, for example, of very dilute sprays, low ambient density conditions, light fuels, etc. On the other hand, it does not work properly for spray images with relatively constant intensity levels, for example: images of non-evaporative sprays, diaphragm-cut Schlieren vapor sprays (which are often very dark), combustion-saturated sprays, etc. In these situations, spray tip penetration is still captured correctly while the full spray boundary is not. Therefore, an additional intensity-sensitive algorithm was adapted, explained in detail by Payri et al. [7], enhanced with the dynamic background correction detailed by Benajes et al. [9] and Payri et al. [10]. The two binary maps obtained from each algorithm are combined into a single binary image from which the contour is extracted. This approach maximizes sensitivity since it takes advantage of the robustness of the SNL algorithm for the spray tip region—and dilute regions or sprays—but at the same time allows for good contour detection in the near nozzle region, where the liquid core often generates a very dark image.

The algorithm then extracts macroscopic characteristics from the detected contours. Spray tip penetration is calculated as the distance between the outlet orifice and the furthest point in the detected boundary. The estimation of the second stage ignition (SSI) delay comes from the signal obtained by computing the sum of the pixel-wise intensities within this boundary (from this point forward referred to as *total intensity*). This summation is done over the inverted spray image, so an increase in the total value indicates a darker and/or larger spray. The resulting signal, and its derivative in time (from this point forward referred to as *total intensity increment*), present unique-consistent features that allow for reliable estimation of the SSI, as thoroughly detailed by BENAJES et al. [9] and PAYRI et al. [10].

6.3 Test plan

Table 6.1: Reactive spray visualization test plan, centered on ECN Spray A boundary conditions [3].

Parameter	Value-Type	Units
Ambient density (ρ)	22.8	kg/m^3
Ambient temperature (T_a).	800, 900, 970	K
Rail pressure (P_r)	60, 90, 150, 200	MPa
Oxygen conc.	21	%
Number of points	12/nozzle/fuel	
Ambient density (ρ)	22.8	kg/m^3
Ambient temperature (T_a)	800, 900, 970	K
Rail pressure (P_r)	60, 90, 150	MPa
Oxygen conc.	15	%
Number of points	9/nozzle/fuel	
Ambient density (ρ)	15.2, 30.4	kg/m^3
Ambient temperature (T_a)	900	K
Rail pressure (P_r)	60, 90, 150	MPa
Oxygen conc.	21	%
Number of points	6/nozzle/fuel	
Total number of points	27/nozzle/fuel	

The test plan, presented in Table 6.1, is centered on ECN Spray A boundary conditions [3], with parametric variations around these. Since the time available for experiments was limited, the test matrix does not comprise every combination of the studied variables, but sweeps of certain resolutions depending on the interest of each variable. Table 6.1 is sub-divided into these three groups of points for easier visualization of the test plan. For all conditions the energizing time was fixed at 2.5 ms. All test points were performed for the two nozzles and three fuels, comprising a total of 162 test points in the high temperature/high pressure test rig.

6.4 Reactive spray development

Figure 6.2 presents a sequence of Schlieren images of two independent injection events for two different fuels. This sequence demonstrates the typical behavior of reactive diesel-type sprays: liquid fuel is injected into a hot ambient gas, the interaction between the high velocity liquid jet and the dense ambient gas shears and atomizes the liquid core, while the spray is also entraining the surrounding hot gas which transfers energy to the liquid fuel to eventually vaporize it completely downstream [6, 13]. Note that a similar figure was presented by PAYRI et al. [6] for inert sprays, showing simultaneous contours for the liquid and vapor phases. Once the reactive spray reaches ignitable fuel mixture fractions, ignition and high temperature combustion take place. The reactive spray continues to penetrate, still exchanging momentum with the ambient gas and progressively slowing down. At the same time, the flame stabilizes in the upstream region at the LOL (see the last images shown for the n-dodecane spray in Figure 6.2). In these Schlieren images, the first stage of the ignition process is appreciable as a brief disappearance of the spray, followed by a sudden expansion and darkening, which corresponds to the second stage ignition (SSI, [14]) as explained by BENAJES et al. [9] and PAYRI et al. [10, 11]. In the particular case presented in Figure 6.2, note how the n-dodecane spray (right column) starts the SSI earlier than the n-heptane spray—524 μs and 736 μs respectively—which is expected, since n-dodecane is a heavier *n*-alkane with longer chain, making it more reactive. This difference in ignition delay (ID)causes differences in the corresponding spray tip penetrations, making the n-dodecane spray penetrate farther. These findings will be analyzed in detail in the following sections.

6.5 Reactive spray tip penetration

The effect of reactivity on spray tip penetration for three fuels is presented in Figure 6.3. Reactivity is controlled by the oxygen concentration in the chamber. 0 %

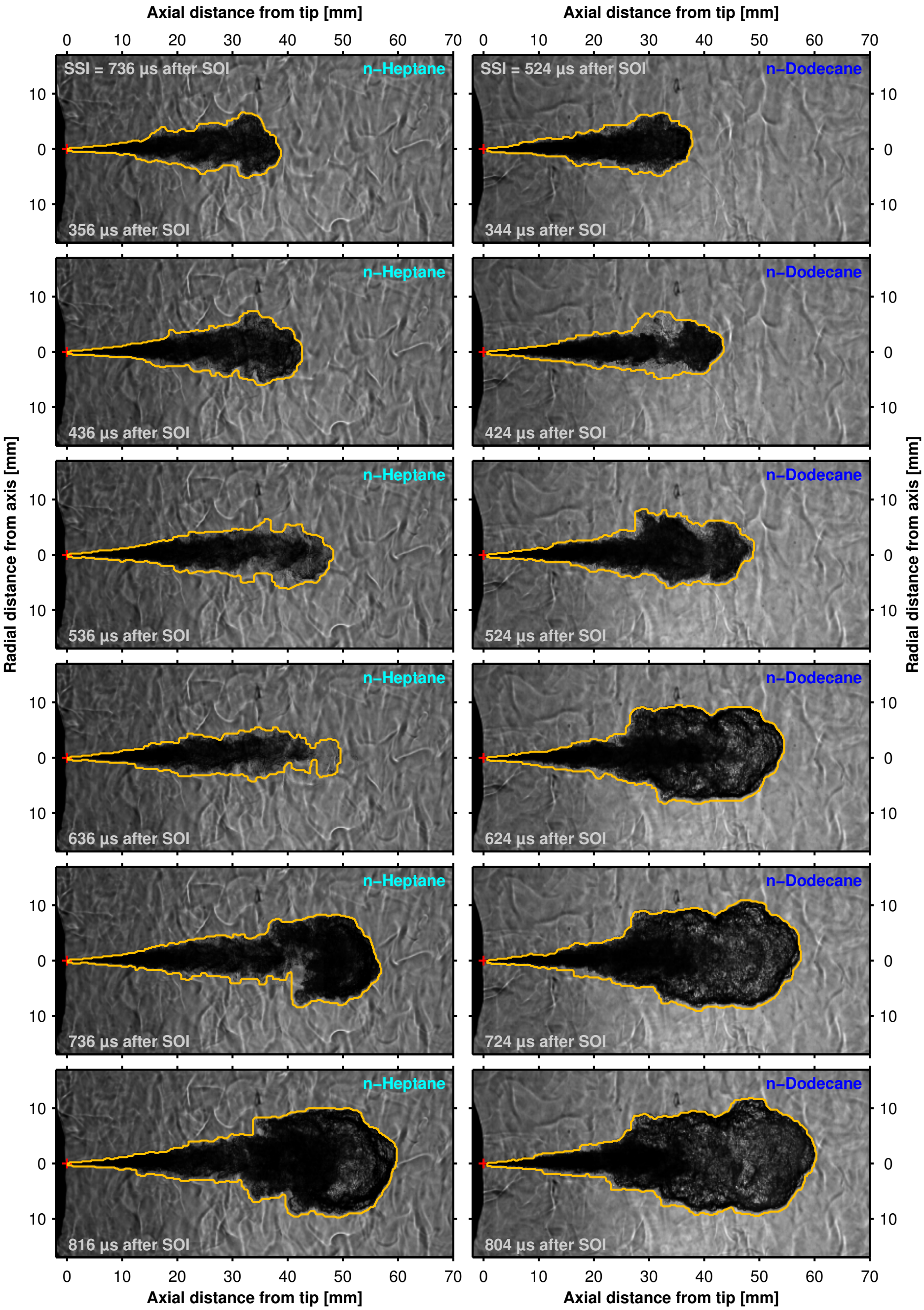

Figure 6.2: Time sequence of Schlieren images of two injection events of n-heptane and n-dodecane sprays. In this case, the nozzle is k15, *rail pressure is 150 MPa, ambient density is 15.2 kg/m^3, ambient temperature is 900 K and the oxygen concentration is 21 %.*

oxygen concentration corresponds to the non-reacting spray presented in chapter 5 while 21 % oxygen concentration corresponds to highest reactivity spray. All three sprays penetrate at the same rate up to a certain time, after which, the penetration curve of the spray with higher reactivity (or oxygen concentration) starts to deviate more and penetrate faster. The faster ignition with higher oxygen concentration translates to higher spray tip penetration, as PASTOR et al. [15] observed for a set of fuels with different reactivities. Figure 6.3 shows that, for all three fuels, higher oxygen concentration leads to earlier spray acceleration or deviation from the non-reacting case.

A similar situation can occur for different ambient temperatures. It is known that ambient temperature is not a determinant variable for non reactive vapor spray penetration if the ambient density is matched [6, 7]. Under reactive conditions however, ambient temperature plays an important role in all the chemical reactions prior to the SSI, and this could result in different spray penetration rates, as Figure 6.4 illustrates. Higher ambient temperatures lead to higher reactivity, shorter ignition delays and thus higher spray tip penetration. The ignition delay does not change significantly above 900 K and hence, when the temperature changes from 900 K to 970 K the spray penetration does not deviate as much as when the temperature is changed from 800 K to 900 K [16, 17].

Figure 6.5 presents the effect of injection pressure on reactive spray tip penetrations. The effect of the injection pressure for non-reacting sprays is clear from the literature [6, 18]. Increasing injection pressure increases spray momentum and thus, the spray tip penetration rate. As will be shown in section 6.7.2, injection pressure does not significantly influence the spray reactivity and ignition delay. Hence, the effect of rail pressure for reacting sprays is very similar to that of a non-reacting spray. The three different fuels show appreciable difference in reactivity and ignition delay and hence, a noticeable effect on spray penetration can be observed. The n-dodecane sprays penetrate faster from an earlier point in time, followed by the Surrogate and n-heptane sprays.

6.6 Lift-off length

Before presenting the results obtained it is interesting to review the parameters affecting LOL as known from the literature. These are fuel composition, ambient temperature, ambient density, ambient oxygen concentration, injection pressure and nozzle geometry [9, 10, 12, 15]. Because of the large data base of the present investigation, select cases will be brought out to illustrate the effect of each variable studied.

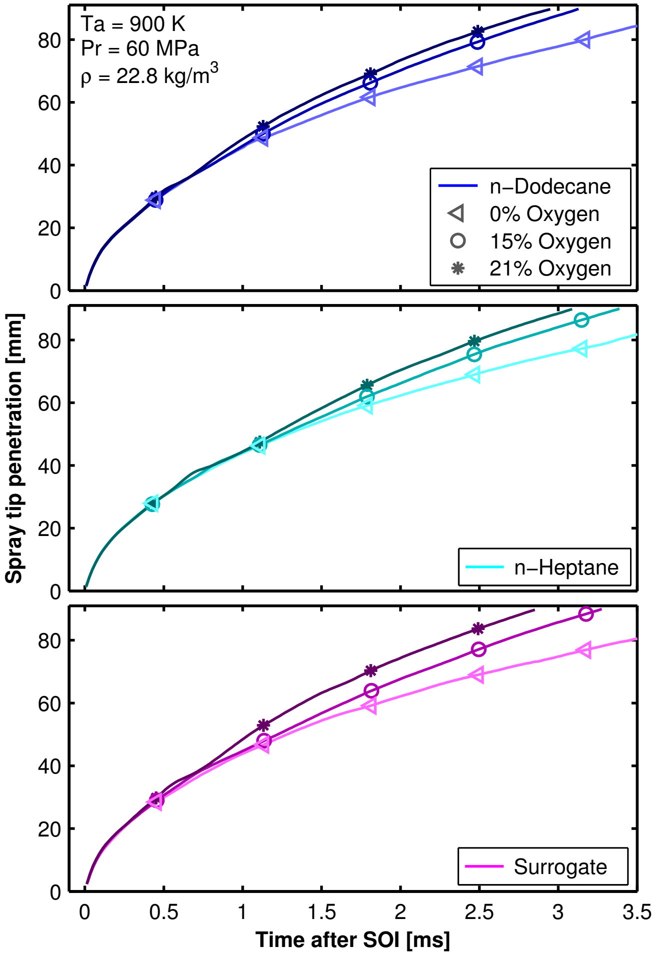

Figure 6.3: Spray tip penetration for all fuels at different oxygen concentrations. In this case, the nozzle is k15*, rail pressure is 60 MPa, ambient density is 22.8 kg/m^3 and ambient temperature is 900 K. Note that inert spray results correspond to results presented in chapter 5.*

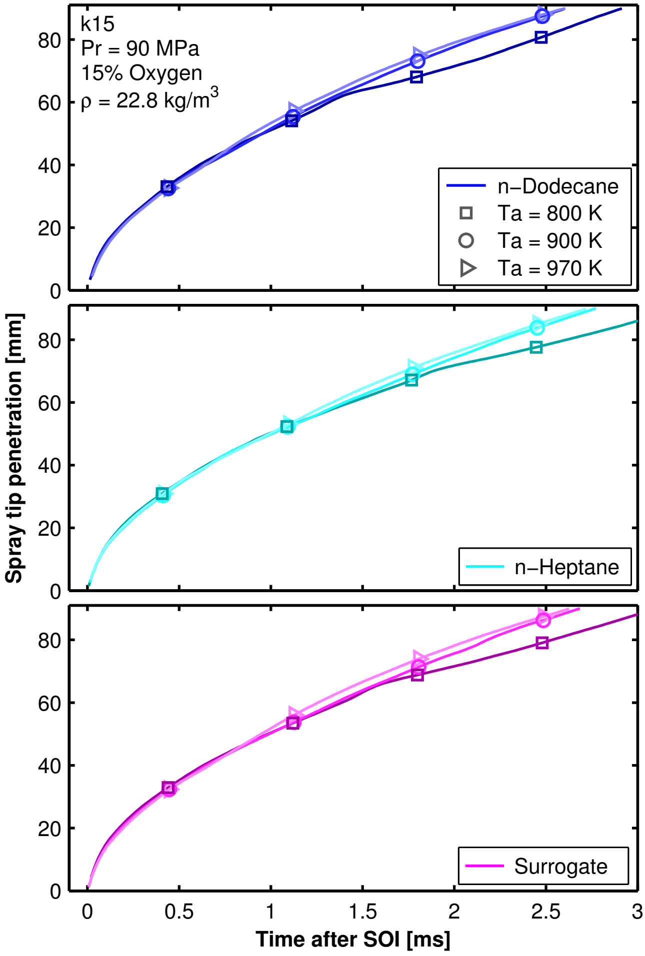

Figure 6.4: Spray tip penetration for all fuels at different ambient temperatures. In this case, the nozzle is k15*, rail pressure is 90 MPa, ambient density is 22.8 kg/m^3 and oxygen concentration is 15 %.*

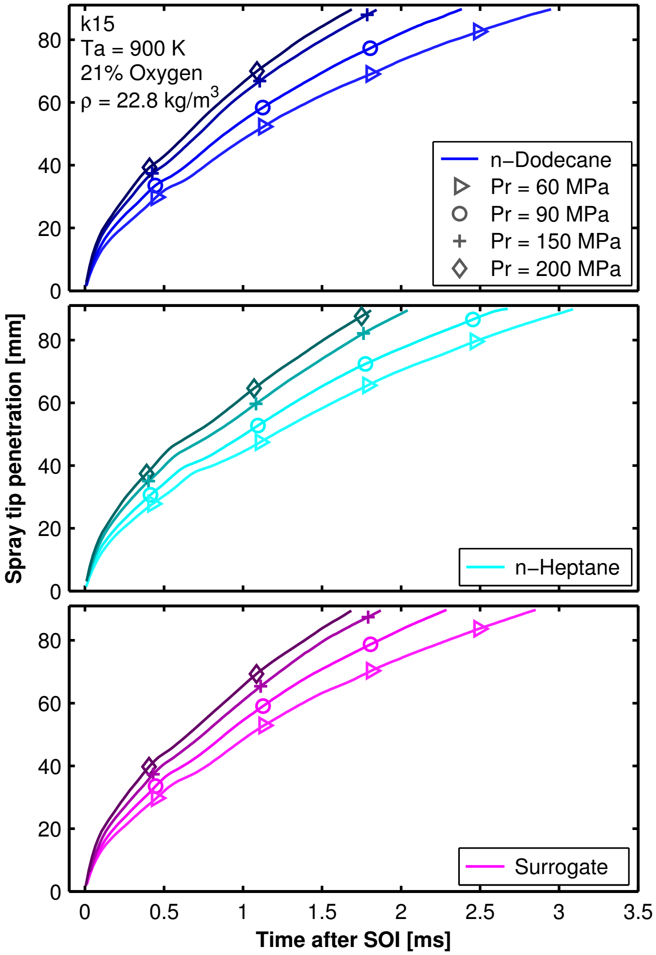

Figure 6.5: Spray tip penetration for all fuels at different rail pressures. In this case, the nozzle is k15*, ambient temperature is 900 K, ambient density is 22.8 kg/m^3 and oxygen concentration is 21 %.*

6.6.1 OH* chemiluminescence signals

Figure 6.6 depicts a comparison of the reactive sprays produced by the two nozzles at particular test conditions. The top and middle parts of Figure 6.6 show ensemble-average OH* chemiluminescence images while the bottom part plots column-wise intensity maximums of the images. The results at these test conditions show that nozzle *k0* produces a spray with shorter LOL when compared to nozzle *k15*, even though its diameter is slightly larger [12, 19], as seen in section 2.5. Signals presented at the bottom part of Figure 6.6 illustrate very similar behaviors between the two nozzles in terms of flame shape and intensity levels. The flame produced by nozzle *k15* shows slightly higher intensity levels downstream which, qualitatively, could be attributed to a more fuel-rich flame, and thus, soot. PAYRI et al. [6, 18, 20] observed that, when compared to the cylindrical nozzle *k0*, the conical nozzle *k15* features smaller spreading angles, so it would be expected for this nozzle to produce a more soot-promoting flame.

Figure 6.7 depicts a comparison of the reactive sprays produced by the three fuels at particular test conditions. Contrary to the comparison shown in Figure 6.6, images and profiles depicted in Figure 6.7 do show significant differences. Images are normalized to the dynamic range of the brighter of the three images, so that they can be visually compared. Note how the OH* chemiluminescence image is brighter and the intensity profile at the bottom plot shows larger values downstream for the Surrogate flame. Qualitatively, the Surrogate fuel produces a flame with more soot in comparison to n-dodecane and n-heptane due to the heavier components and, especially, aromatic content. The LOL results obtained are in agreement with the expected trends discussed: shorter LOL for n-dodecane, followed by Surroage fuel and finally higher LOL for n-heptane.

These particular cases presented in detail show only a small sample of the behaviors observed for the whole test matrix. The trends observed in the full test matrix, however, were very consistent as shown in the following section.

6.6.2 Parametric variations

This section discusses LOL results for a larger window of test conditions and parametric variations. Figure 6.8 presents stabilized LOLs for all nozzles and fuels in a subset of the whole dataset, a sweep of ambient temperature at high and low rail pressures. First, it is easily noticeable how fuels are stratified in terms of LOL. n-Heptane consistently showed the longest LOLs, followed by the Surrogate fuel. PICKETT et al. [21] and later PASTOR et al. [15] observed that LOL was mainly controlled by ignition delay time, rather than flame velocity. Since there is very little reason to suspect significantly different flame velocities among these fuels

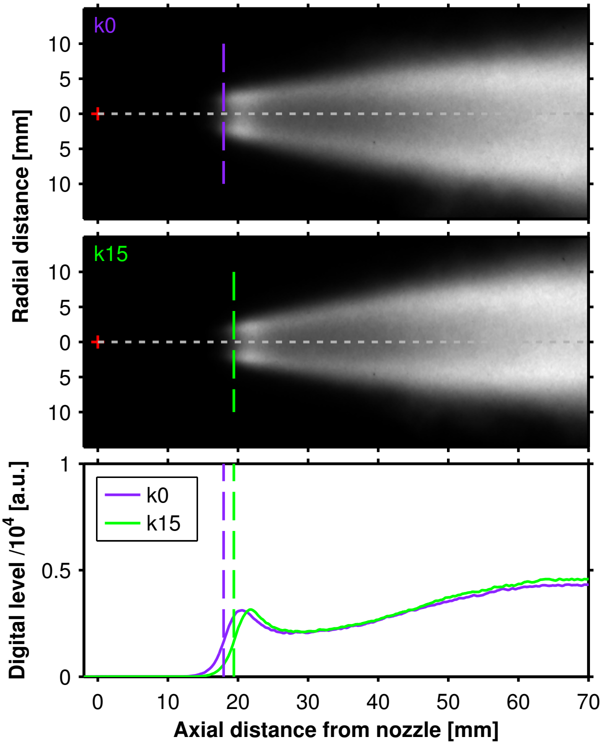

Figure 6.6: Ensemble-average OH chemiluminescence images of the flames produced by the two nozzles at particular test conditions. The intensity profiles shown in the bottom plot depict the column-wise intensity maximum of each image. In this case the fuel is n-heptane, rail pressure is 150 MPa, ambient density is 22.8 kg/m^3, oxygen concentration is 15 % and ambient temperature is 970 K.*

[22, 23], the observations in this study concur with that conclusion: regarding fuel properties, LOL is mainly determined by the reactivity of the fuel.

On another line, note in Figure 6.8 how LOL increases considerably with rail pressure. This is also explained by the relationship between LOL and ignition delay: for larger injection pressures—thus, larger injection velocities [18]—fuel travels a longer distance for that given ignition delay time.

Figure 6.8 also shows the effect of nozzle geometry over LOL. Under virtually all conditions tested, the cylindrical *k0* produced shorter LOLs when compared to the conical nozzle *k15*. All previous chapters showed that differences in the development of the sprays produced by the two nozzles are reduced as rail pressure is increased [6, 18, 20]. Even though differences in hydraulic characteristics indeed increase with rail pressure [18], the higher injection and entrainment velocities

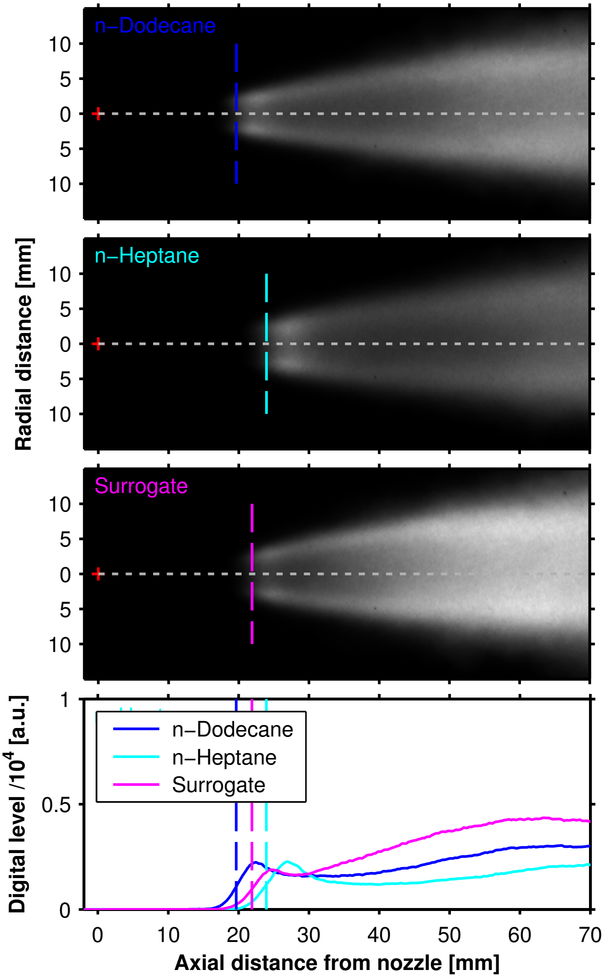

Figure 6.7: Ensemble-average OH chemiluminescence images of the flames produced by the three fuels at particular test conditions. The intensity profiles shown in the bottom plot depict the column-wise intensity maximum of each image. In this case the nozzle is* k15, *rail pressure is 150 MPa, ambient density is 22.8 kg/m^3, oxygen concentration is 15 % and ambient temperature is 900 K.*

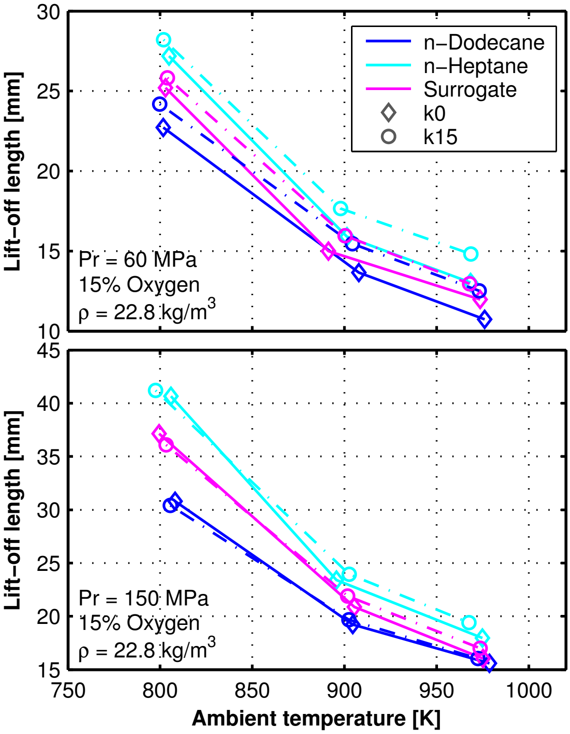

Figure 6.8: Lift-off length as a function of ambient temperature for all nozzles and fuels at an ambient density of 22.8 kg/m^3*, an oxygen concentration of 15 % and rail pressures of 60 MPa (top) and 150 MPa (bottom).*

induced by higher rail pressure suppress the small effects of nozzle geometry over the development of turbulent profiles in the spray and momentum exchange between the spray and the ambient gas [6, 18, 20]. This trend is also observed in the LOL results, where the difference in LOL between nozzles is reduced with increasing rail pressure. This proves consistency in the behavior of these nozzles in terms of isothermal liquid spray formation (chapter 4, [18, 20]), evaporative inert spray formation (chapter 5, [6]) and LOL stabilization of reactive sprays exposed in this chapter [13].

Note that the hydraulic characterization of these nozzles, presented by PAYRI et al. [18], showed that the cylindrical nozzle *k0* features larger outlet flow velocities in comparison to the conical nozzle *k15*, due to the area contraction. Higher velocity should also translate into larger LOL, but in this case the cylindrical nozzle geometry also produces larger spreading angles and fluctuations [6, 18, 20] which dominate over the higher velocity to produce shorter LOL after all.

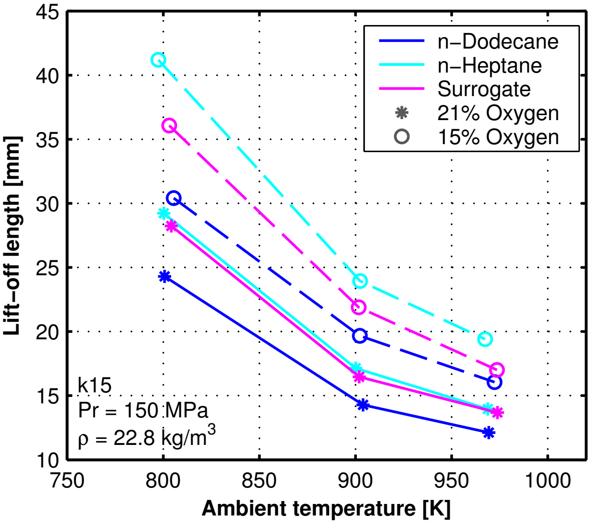

Figure 6.9: Lift-off length as a function of ambient temperature for all fuels and the two oxygen concentrations tested. In this case, the nozzle is k15*, ambient density is 22.8 kg/m^3 and rail pressure is 150 MPa.*

Moreover, Figure 6.9 shows a subset of the the LOL results as a function of ambient temperature, for all fuels, in this case illustrating the effect of oxygen concentration. Note the large differences in LOL due to the oxygen concentrations. Even though laminar flame velocities are indeed strongly affected by equivalence ratio [22, 23], the different LOL values observed here for the two oxygen concentrations are attributed to the corresponding ignition delay times.

Figure 6.10 depicts a subset of the LOL results as a function of ambient density, for all nozzles and fuels. Note that the effect of ambient density is very straight forward: higher density implies that more oxygen is available to oxidize the fuel and thus, shorter ignition delays are expected, which reduce the corresponding LOL [12, 21].

6.7 Ignition delay

Analogous to the LOL results section, it is also interesting to review the parameters affecting ID as known from the literature. These are fuel composition, ambient temperature, ambient density, ambient oxygen concentration, injection pressure and nozzle geometry [9, 10, 12, 15]. Because of the large data base of the present

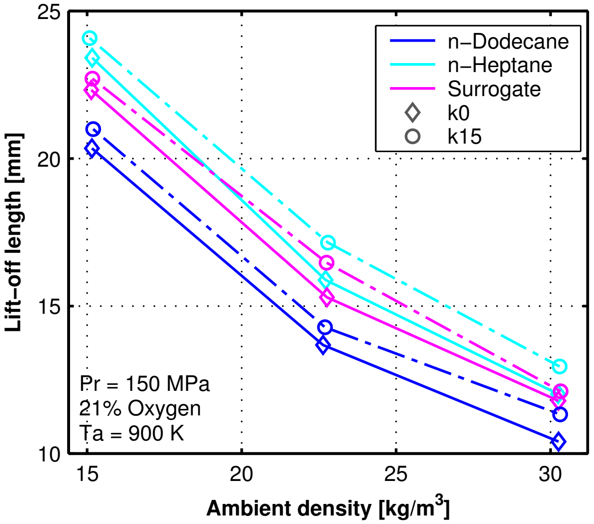

Figure 6.10: Lift-off length as a function of ambient density for all nozzles and fuels at a rail pressure of 150 MPa, an oxygen concentration of 21 % and an ambient temperature of 900 K.

investigation, select cases will be presented to illustrate the effect of each variable studied [13].

6.7.1 Tracer signals

Figures 6.11 through 6.14 display the time evolution of the tracers signals involved in the SSI detection. The top part of each figure shows the result of the pixel-wise intensity sum within the spray boundary (total intensity signal), while the bottom part of each figure shows its derivative (total intensity increment). As Figure 6.2 illustrates, at the first onset of chemical reactions, also known as start of cool flames (SoCF), the spray becomes transparent and the slope of the total intensity values changes suddenly. This transparent phase may not occur in some test conditions where ignition delays are very short, but the rest of the process develops in a very defined fashion. After this first stage, the spray tip appears again in the image and the total intensity values increase rapidly (in the inverted image, while it darkens in the actual image) to then steadily keep increasing with the spray growth. BENAJES et al. [9] and PAYRI et al. [10, 11, 13] demonstrated that it is possible to correlate this rapid increase in total intensity values to the SSI. At the SSI, the total intensity signal slope reaches a maximum, as a result of the high temperature combustion, which causes rapid spray volume expansion but also changes refractive indexes inside the spray, darkening the spray or in fact making it brighter in the inverted image.

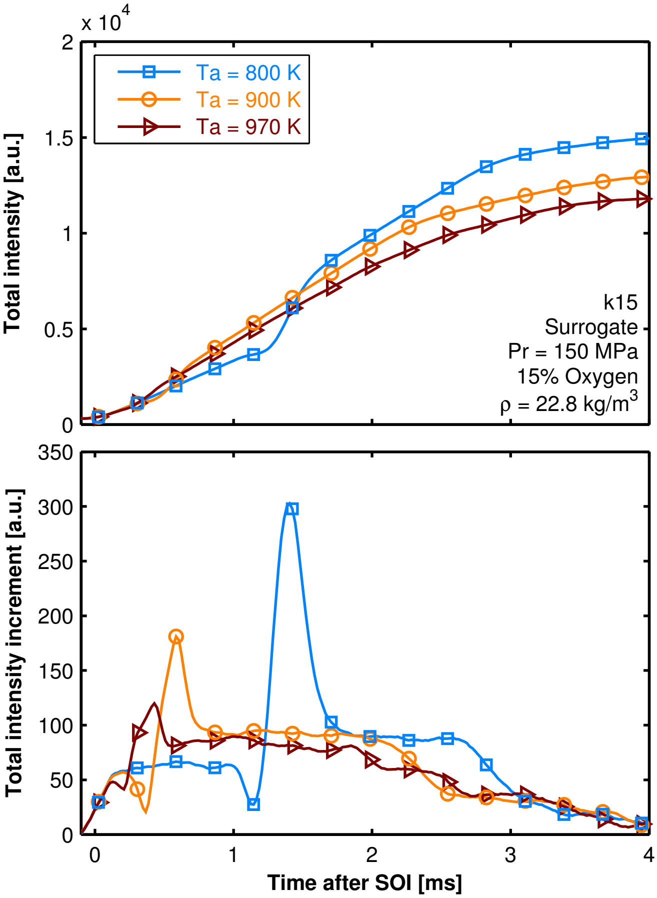

Figure 6.11: Total spray intensity (top) and intensity increment (bottom) tracer signals for a sweep of ambient temperatures. In this case the nozzle is k15*, fuel is the Surrogate, rail pressure is 150 MPa, ambient density is 22.8 kg/m^3 and oxygen concentration is 15 %.*

Figure 6.11 illustrates the effect of ambient temperature on the ignition behavior as traced by the total intensity signal of interest. As the temperature is lower, the ignition event delays in a non-linear fashion and the intensity of the pre-mixed combustion increases, which is qualitatively observed in Figure 6.11. Very similar results were observed by BENAJES et al. [9] and PAYRI et al. [10] on their study for the two-component surrogate of the ECN, where a wider range of ambient temperatures were considered.

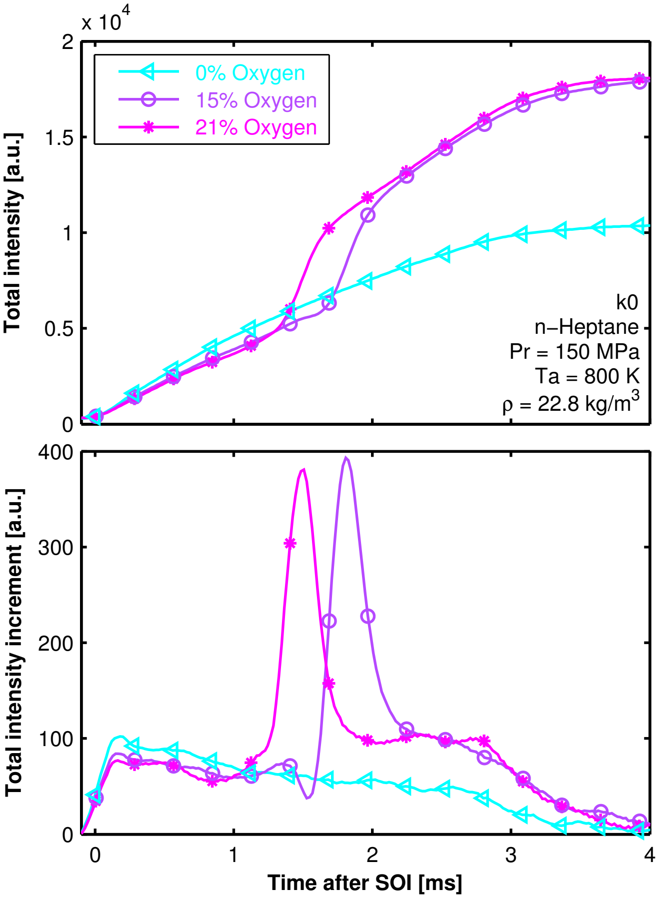

Figure 6.12: Total spray intensity (top) and intensity increment (bottom) tracer signals for a sweep of oxygen concentrations. In this case the nozzle is k0*, fuel is n-heptane, rail pressure is 150 MPa, ambient density is 22.8 kg/m*^{3} *and ambient temperature is 800 K.*

The effect of oxygen concentration is also appreciable on the tracer signals both quantitatively and qualitatively. The observations found here coincide to the results previously reported by BENAJES et al. [9], where the ignition event delays with the decrease of oxygen concentration in a non-linear fashion. The inert case—which comes from the experiments presented in chapter 5—is shown for reference. Note that both Figures 6.11 and 6.12 illustrate the effect of ambient reactivity on the ignition delay. A more reactive ambient facilitates the breakdown of the fuel and accelerates the onset of chemical reactions which trigger the ignition process [10, 14, 16, 17, 24–26].

Figure 6.13 depicts a comparison of these tracer signals produced by the two nozzles at particular test conditions. In chapters 4 and 5, it was seen that sprays produced by the cylindrical nozzle *k0* features larger spreading angles in comparison to those produced by the conical nozzle *k15*. This is translated into larger line-of-sight area which, at the same time, increases the total intensity value and its increments in time. Figure 6.13-bottom shows two maximums which correspond to the two SSI timings of the sprays produced by the two nozzles. Note that the spray produced by the conical nozzle *k15* ignites before the spray produced by nozzle *k0*, while the latter shows a higher maximum which can be associated with a more pre-mixed combustion [9, 10]. Even though this is a single example at particular test conditions, this trend was found to be consistent throughout the complete test matrix, as will be discussed later in this chapter.

Fuels, on the other hand, do not alter the vapor spray spreading angle and penetration significantly [6], so the line-of-sight spray area is similar between fuels, which implies similar total intensity signals before ignition, as depicted by Figure 6.14. In these and virtually all conditions tested, n-dodecane sprays ignite the earliest, followed by Surrogate sprays and last, n-heptane sprays, as will be discussed next. As explained also for Figure 6.13, longer ignition delays imply a more pre-mixed combustion which produces a sharper slope of the total intensity signal and thus, a larger maximum in the total intensity increment signal. After ignition is complete and diffusion takes over, the three signals behave similarly, as shown in both the top and bottom parts of Figure 6.14.

6.7.2 Parametric variations

A larger set of data is scattered in Figure 6.15, with the top and bottom parts showing sub-sets of injections at 60 MPa and 150 MPa respectively. As expected from the literature, increasing ambient temperature increases the reactivity of the ambient gas which decreases IDs [9–11, 14, 15, 17, 21, 27]. Also, as PAYRI et al. [10, 28] observed, IDs decrease with increasing rail pressure, which is the result of faster liquid break-up and mixture preparation.

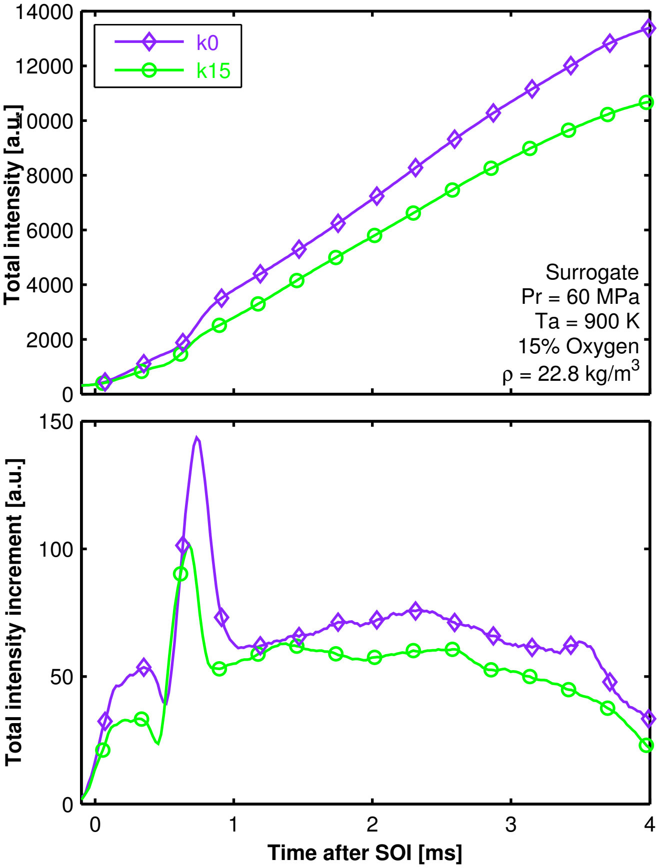

Figure 6.13: Total spray intensity (top) and intensity increment (bottom) tracer signals for the two nozzles at particular test condition. In this case the fuel is the Surrogate, rail pressure is 60 MPa, ambient density is 22.8 kg/m^3, ambient temperature is 900 K and oxygen concentration is 15 %.

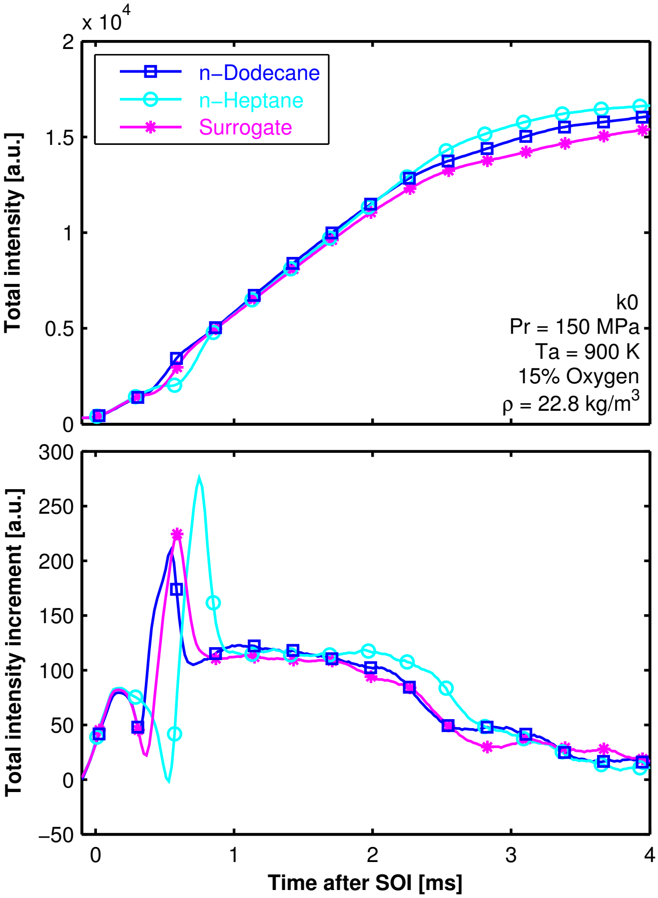

Figure 6.14: Total spray intensity (top) and intensity increment (bottom) tracer signals for the three fuels at particular test conditions. In this case the nozzle is k0*, rail pressure is 150 MPa, ambient density is 22.8 kg/m^3, ambient temperature is 900 K and oxygen concentration is 15 %.*

Furthermore, Figure 6.15 shows that, in all cases, n-dodecane sprays feature the shortest SSI delays, followed by Surrogate sprays and last, n-heptane. Also as stated before, the conical nozzle *k15* produces sprays with slightly shorter SSI delays when compared to the cylindrical nozzle *k0*. This will be discussed further at the end of this section.

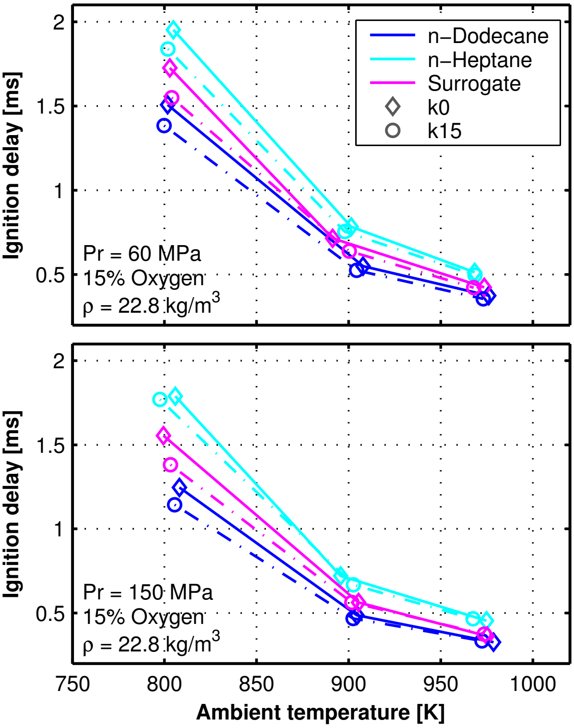

Figure 6.15: Ignition delay after SOI as a function of ambient temperature for all nozzles and fuels at an ambient density of 22.8 kg/m^3, an oxygen concentration of 15 % and rail pressures of 60 MPa (top) and 150 MPa (bottom).

Figures 6.16 and 6.17 illustrate the effect of ambient oxygen concentration and ambient density over the SSI delay. Results are in good agreement with the trends found in the literature, increasing oxygen concentration and ambient density decreases IDs [9, 10, 21]. At these relatively low ambient temperatures, chain-branching reactions are highly dependent on fuel reactivity and oxygen availability for the formation of radicals [15]. These figures also show that the different fuels respond consistently, in terms of ignition performance, to variations in ambient conditions, as is the case for the nozzle geometry.

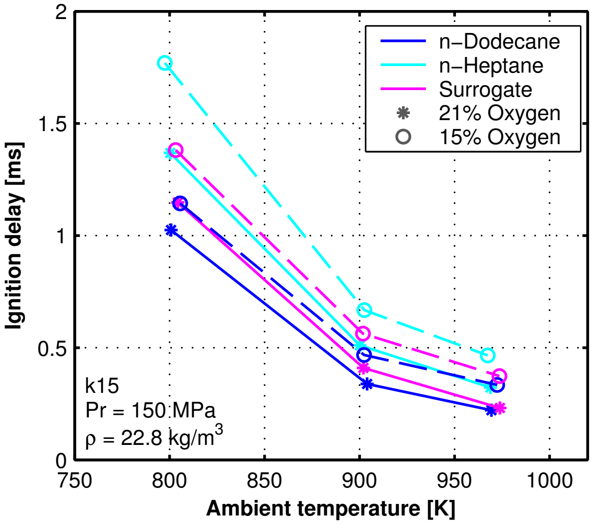

Figure 6.16: Ignition delay after SOI as a function of ambient temperature for all fuels and the two oxygen concentrations tested. In this case, the nozzle is k15*, ambient density is 22.8 kg/m*^{3} *and rail pressure is 150 MPa.*

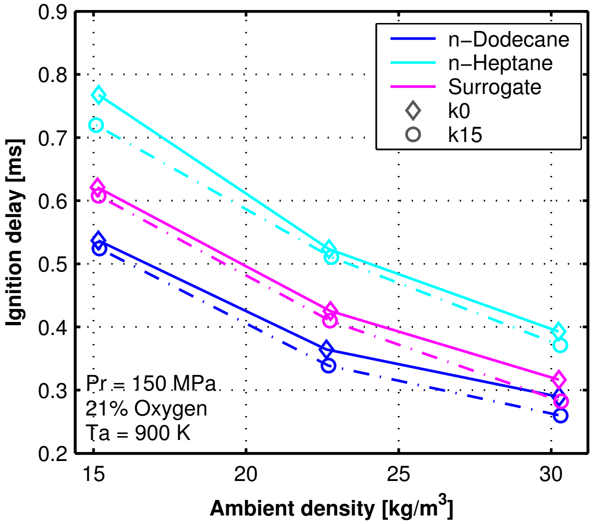

Figure 6.17: Ignition delay as a function of ambient density for all nozzles and fuels at a rail pressure of 150 MPa, an oxygen concentration of 21 % and an ambient temperature of 900 K.

6.7.3 Further discussion on the effect of nozzle geometry over the SSI

The effect of nozzle geometry over the ignition performance of the fuel sprays was found to be very consistent throughout the full test matrix, as Figures 6.15, 6.16 and 6.17 illustrate. The conical nozzle *k15* produces sprays that, in average, feature 5.1 % shorter SSI delays in comparison to those produced by the cylindrical nozzle *k0*. It is important to point out that similar results were previously reported by KONG and BAE [29] and PAYRI et al. [28] from their studies in optically accessible engines, both of which found that conical nozzles produced shorter ignition delays in comparison to cylindrical nozzles, but these results contradict the numerical predictions reported by SOM et al. [19]. This contrast, along the little information found in the literature on the extent of the effect of nozzle geometry over ignition performance of diesel sprays, leave room for further discussions on the subject, and additional analyses—both numerical but also experimental—should be performed to arrive at solid conclusions.

In the case of this study, as the test matrix is so large and the trend between nozzles is so consistent, hypotheses should be discussed. The behavior observed might be unexpected at first, since the cylindrical nozzle *k0* features stronger turbulent velocity profiles at the outlet orifice that produce larger spreading angles and spray boundary fluctuations [6, 18, 20], which consequently lead to shorter liquid lengths [6]. Shorter liquid lengths can mislead one to expect shorter SSI delays because of the often associated faster liquid breakup and mixture preparation. Nevertheless, in these mixing-limited sprays, liquid length is strongly dependent on spreading angle, which the author believes is the dominant parameter for the shorter liquid lengths featured by the cylindrical nozzle *k0*. In their studies, KONG and BAE [29] and PAYRI et al. [28] attribute the shorter ignition delays found for their conical nozzles—in comparison to their cylindrical nozzles—to better atomization and liquid breakup, due to the thinner liquid core produced by the smaller nozzle diameter of the conical nozzles. This could also be the case for the present study. On the same lines, even if the two nozzles in this study were assumed to produce sprays with similar break-up/vaporization times or even shorter for the cylindrical nozzle, at the moment either spray reached vaporized ignitable mixtures the local equivalence ratio at the ignition location of the spray produced by the cylindrical nozzle *k0* would be expected to be lower than that of the spray produced by nozzle *k15*, because of its significantly larger spread volume [6, 30] at virtually similar injected mass [18]. As it is largely known, the reaction paths at low temperatures are dependent on radical species formed directly from the fuel, so richer mixtures oxidize faster [24, 25].

Figure 6.18 presents a sequence of Schlieren images showing particular ignition events for the sprays produced by the two nozzles at equivalent test conditions. Each row is labeled with the corresponding elapsed time after SOI, and the detected contours are shown to illustrate the spray line-of-sight area. The spray produced by the cylindrical nozzle *k0* (left side of Figure 6.18) ignites later than the spray produced by the conical nozzle *k15* (right side of Figure 6.18); the difference in this case is small at 21 μs but still appreciable in the images. It can be seen in this figure that, at the corresponding times of SSI for each nozzle (indicated at the top of each column), the spray produced by the cylindrical nozzle *k0* has spread considerably more, as was expected from the behavior of their inert vapor sprays [6]. The complete SSI delay time is a composition of the liquid break-up, fuel vaporization and chemical kinetic mechanisms. When comparing nozzles in this study, SSI delay results lead to think that the chemical kinetics are the dominant factor to the final outcome of the SSI delay behavior, due to the differences in local equivalence ratios between the sprays produced by the two nozzles. In cases with larger differences in ignition delay between nozzles, the spray produced by the cylindrical nozzle will have penetrated and spread further into the ambient gas, probably igniting at even lower equivalence ratios. This is also observable in both the top and bottom parts of Figure 6.13, since the total intensity signal is also a measurement of the line-of-sight spray area detected, and lines that corresponds to the cylindrical nozzle *k0* stays above lines that corresponds to the conical nozzle *k15*. This trend between nozzles regarding total intensity signals was consistent along the full test matrix. In addition, Figure 6.6 also shows larger intensity profiles downstream of the LOL for the conical nozzle *k15* that could, qualitatively, be associated to a more sooting flame, also indicating richer equivalence ratios near the LOL region.

Finally, even though soot formation is out of the scope of this thesis, the authors point out that a further study should be carried out to analyze soot formation for the three fuels. In particular, the Surrogate fuel is of interest, since it is conceptualized to better mimic the soot-related behavior of real diesel fuel, as its PAH content should increase soot formation in comparison to pure n-alkanes. However, it is also possible that the SSI delay induced by the α-methylnaphthalene content is large enough so to delay ignition to a point where the local equivalence ratio is very low, which would render a less-sooting flame: a similar situation what was found for the secondary fuel of the ECN, which is a mixture of n-dodecane and m-xylene [10, 26].

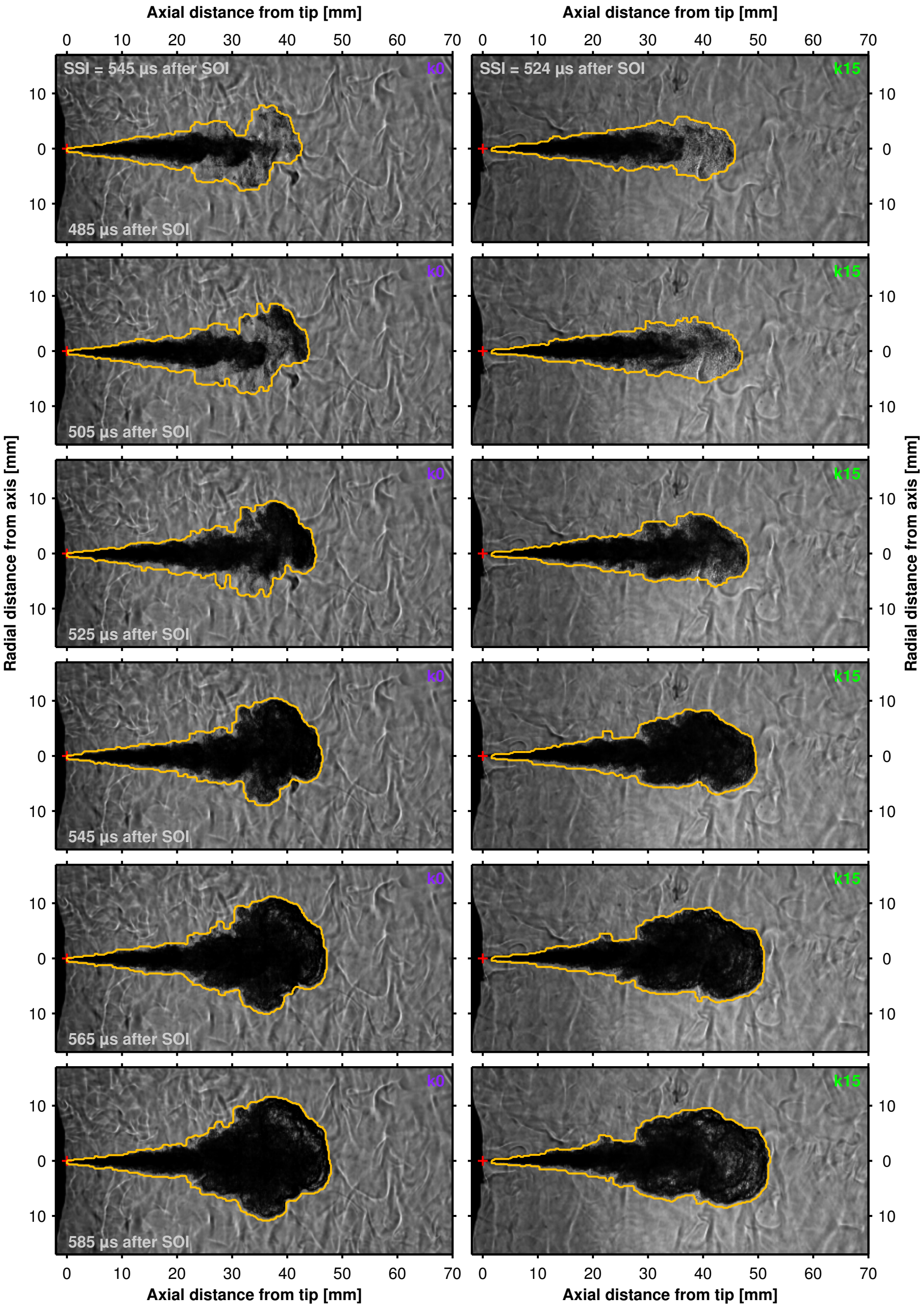

Figure 6.18: Time sequence of Schlieren images of two injection events of the sprays produced by k0 *and* k15 *nozzles. In this case, fuel is n-dodecane, rail pressure is 150 MPa, ambient density is 15.2 kg/m*^{3}*, ambient temperature is 900 K and the oxygen concentration is 21 %.*

6.8 Conclusions

The influence of internal nozzle flow characteristics over ignition delay, and flame lift-off of reacting direct-injection sprays is studied experimentally for three fuels using two different nozzle geometries [13].

Reacting spray is found to penetrate faster than non-reacting spray due to combustion induced acceleration after ignition. Higher oxygen concentration, and ambient temperature enhance the reactivity leading to higher spray tip penetration. Injection pressure does not affect the reactivity significantly and hence, influences spray penetration through momentum—similar to a non-reacting spray.

Both ignition delay and lift-off length are found to be shortest and longest for n-dodecane and n-heptane, respectively, while the surrogate fuel falls in-between the two pure component fuels. Both ignition delay and lift-off length are found to decrease with increase in oxygen concentration, ambient temperature, and density, in agreement with previous works found in the literature. The conical nozzle, in spite of longer lift-off length is found to have shorter ignition delay, when compared to the cylindrical nozzle. This could be due to smaller liquid vain that breaks-up and vaporizes quicker to form a reactive mixture faster than the droplets from cylindrical nozzle, but could also be to the fact that the spray produced by the cylindrical nozzle spreads considerably more, which reduces the local equivalence ratio at the time of ignition. This trend between nozzles was found to be in agreement to previous experimental studies [28, 29] but in contradiction to numerical predictions [19]. Hence, further analysis for a more in-depth understanding of this mechanics involved in this process should be considered.

As was the case of all previous chapters, the database obtained is available for download at: `http://www.cmt.upv.es/DD01.aspx`.

References

[1] Diwakar, R. and Singh, S. “NOx and soot reduction in diesel engine premixed charge compression ignition combustion: a computational investigation”. *International Journal of Engine Research* 9.3 (2008), pp. 195–214.

[2] Payri, R., García-Oliver, J. M., Bardi, M., Manin, J., Garcia-Oliver, J. M., Bardi, M., and Manin, J. “Fuel temperature influence on diesel sprays in inert and reacting conditions”. *Applied Thermal Engineering* 35.March (Mar. 2012), pp. 185–195.

[3] BARDI, M., PAYRI, R., MALBEC, L. M., BRUNEAUX, G., PICKETT, L. M., MANIN, J., BAZYN, T., and GENZALE, C. L. “Engine Combustion Network: Comparison of Spray Development, Vaporization, and Combustion in Different Combustion Vessels”. *Atomization and Sprays* 22.10 (2012), pp. 807–842.

[4] JUNG, Y., MANIN, J., SKEEN, S. A., and PICKETT, L. M. “Measurement of Liquid and Vapor Penetration of Diesel Sprays with a Variation in Spreading Angle”. *SAE Technical Paper 2015-01-0946* (2015).

[5] FANSLER, T. D. and PARRISH, S. E. “Spray measurement technology: a review”. *Measurement Science and Technology* 26.1 (Jan. 2015), p. 012002.

[6] PAYRI, R., VIERA, J. P., GOPALAKRISHNAN, V., and SZYMKOWICZ, P. G. “The effect of nozzle geometry over the evaporative spray formation for three different fuels”. *Fuel* 188 (2017), pp. 645–660.

[7] PAYRI, R., GIMENO, J., VIERA, J. P., and PLAZAS, A. H. “Needle lift profile influence on the vapor phase penetration for a prototype diesel direct acting piezoelectric injector”. *Fuel* 113 (2013), pp. 257–265.

[8] PAYRI, R., GIMENO, J., BRACHO, G., and VAQUERIZO, D. “Study of liquid and vapor phase behavior on Diesel sprays for heavy duty engine nozzles”. *Applied Thermal Engineering* 107 (2016), pp. 365–378.

[9] BENAJES, J., PAYRI, R., BARDI, M., and MARTÍ-ALDARAVÍ, P. “Experimental characterization of diesel ignition and lift-off length using a single-hole ECN injector”. *Applied Thermal Engineering* 58.1-2 (2013), pp. 554–563.

[10] PAYRI, R., VIERA, J. P., PEI, Y., and SOM, S. “Experimental and numerical study of lift-off length and ignition delay of a two-component diesel surrogate”. *Fuel* 158 (2015), pp. 957–967.

[11] PAYRI, R., SALVADOR, F. J., MANIN, J., and VIERA, A. “Diesel ignition delay and lift-off length through different methodologies using a multi-hole injector”. *Applied Energy* 162 (2016), pp. 541–550.

[12] HIGGINS, B. and SIEBERS, D. L. “Measurement of the Flame Lift-Off Location on DI Diesel Sprays Using OH Chemiluminescence”. *SAE Paper 2001-01-0918* (2001).

[13] PAYRI, R., VIERA, J. P., GOPALAKRISHNAN, V., and SZYMKOWICZ, P. G. “The effect of nozzle geometry over ignition delay and flame lift-off of reacting direct-injection sprays for three different fuels”. *Fuel* 199 (2017), pp. 76–90.

[14] HIGGINS, B., SIEBERS, D. L., and ARADI, A. “Diesel-Spray Ignition and Premixed-Burn Behavior”. *SAE Technical Paper 2000-01-0940* 724 (2000).

[15] PASTOR, J. V., GARCIA-OLIVER, J. M., LOPEZ, J. J., and VERA-TUDELA, W. “An experimental study of the effects of fuel properties on reactive spray evolution using Primary Reference Fuels”. *Fuel* 163.X (2016), pp. 260–270.

[16] BATTIN-LECLERC, F. “Detailed chemical kinetic models for the low-temperature combustion of hydrocarbons with application to gasoline and diesel fuel surrogates”. *Progress in Energy and Combustion Science* 34 (2008), pp. 440–498.

[17] RAJU, M., WANG, M., SENECAL, P. K., SOM, S., and LONGMAN, D. E. “A reduced diesel surrogate mechanism for compression ignition engine applications”. *Proceedings of the ASME 2012 Internal Combustion Engine Division Fall Technical Conference ICEF2012*. Vancouver: American Society of Mechanical Engineers, 2012.

[18] PAYRI, R., VIERA, J. P., GOPALAKRISHNAN, V., and SZYMKOWICZ, P. G. “The effect of nozzle geometry over internal flow and spray formation for three different fuels”. *Fuel* 183 (Nov. 2016), pp. 20–33.

[19] SOM, S., RAMÍREZ, A. I., LONGMAN, D. E., and AGGARWAL, S. K. “Effect of nozzle orifice geometry on spray, combustion, and emission characteristics under diesel engine conditions”. *Fuel* 90.3 (2011), pp. 1267–1276.

[20] PAYRI, R., SALVADOR, F. J., GIMENO, J., and VIERA, J. P. “Experimental analysis on the influence of nozzle geometry over the dispersion of liquid n-dodecane sprays”. *Frontiers in Mechanical Engineering* 1 (2015), pp. 1–10.

[21] PICKETT, L. M., SIEBERS, D. L., and IDICHERIA, C. A. “Relationship Between Ignition Processes and the Lift-Off Length of Diesel Fuel Jets”. *SAE Paper 2005-01-3843* 724 (2005).

[22] METGHALCHI, M. and KECK, J. C. “Burning velocities of mixtures of air with methanol, isooctane, and indolene at high pressure and temperature”. *Combustion and Flame* 48 (Jan. 1982), pp. 191–210.

[23] JERZEMBECK, S., PETERS, N., PEPIOTDESJARDINS, P., and PITSCH, H. “Laminar burning velocities at high pressure for primary reference fuels and gasoline: Experimental and numerical investigation”. *Combustion and Flame* 156.2 (Feb. 2009), pp. 292–301.

[24] CURRAN, H., GAFFURI, P., PITZ, W. J., and WESTBROOK, C. “A Comprehensive Modeling Study of n-Heptane Oxidation”. *Combustion and Flame* 114.1-2 (1998), pp. 149–177.

[25] DESANTES, J. M., BERMÚDEZ, V., LÓPEZ, J. J., and LÓPEZ-PINTOR, D. “Experimental validation of an alternative method to predict high and low-temperature ignition delays under transient thermodynamic conditions for PRF mixtures using a Rapid Compression-Expansion Machine”. *Energy Conversion and Management* 129 (Dec. 2016), pp. 23–33.

[26] PEI, Y., MEHL, M., LIU, W., LU, T., PITZ, W. J., and SOM, S. “A Multicomponent Blend as a Diesel Fuel Surrogate for Compression Ignition Engine Applications”. *Journal of Engineering for Gas Turbines and Power* 137.11 (May 2015), p. 111502.

[27] PITZ, W. J. and MUELLER, C. J. “Recent progress in the development of diesel surrogate fuels”. *Progress in Energy and Combustion Science* 37.3 (2011), pp. 330–350.

[28] PAYRI, R., SALVADOR, F. J., GIMENO, J., and DE LA MORENA, J. “Effects of nozzle geometry on direct injection diesel engine combustion process”. *Applied Thermal Engineering* 29.10 (2009), pp. 2051–2060.

[29] KONG, J. and BAE, C. “Effect of a conical nozzle orifice on the combustion and emissions in a direct- injection compression ignition engine under low-load conditions”. *Proceedings of the Institution of Mechanical Engineers, Part D: Journal of Automobile Engineering* 229.1 (Jan. 2015), pp. 3–13.

[30] LEQUIEN, G., SKEEN, S., MANIN, J., PICKETT, L. M., and ANDERSSON, O. “Ignition Quality Effects on Lift-Off Stabilization of Synthetic Fuels”. *SAE International Journal of Engines* 8.2 (Apr. 2015), pp. 2015–01–0792.

Chapter 7

Conclusions

This chapter aims at drawing the main conclusions with respect to the work carried out along this thesis. The main goals reached in this investigation are presented relating the results obtained in the different phases of the investigation and putting them in a wider context.

The last section of this chapter proposes a list of the potential developments of the present work, indicating directions for new studies and possible improvements to the quality of the results presented in this thesis.

7.1 Summary and conclusions

This thesis sought to contribute to the current understanding of the effects of nozzle geometry over the direct injection diesel spray development through an experimental approach. A considerable effort was put into employing, implementing and/or developing state of the art techniques and image processing algorithms, in order to process such a large database in a systematic manner.

Taking advantage from the technology, equipment and facilities available at CMT Motores Térmicos, different aspects of the injection process have been thoroughly studied. In particular, the experiments performed can be divided in four main groups basing on their specific target:

- Hydraulic characterization of the fuel flow inside the nozzles.
- Isothermal liquid spray characterization.

- Evaporative inert spray characterization, considering both liquid and vapor phases.
- Reactive spray characterization, considering ignition and combustion.

All experiments were performed for two different nozzle geometries and three fuels. Two of the fuels are pure components—n-heptane and n-dodecane—while the third fuel consists of a three-component surrogate to better represent the physical and chemical properties of diesel fuel. The experimental campaign consisted in a complete hydraulic characterization—instantaneous injection rate and spray momentum flux measurements—followed by a high-speed visualization of the isothermal liquid spray, through a diffuse back-illumination technique that employs a fast pulsed light source. After, the evaporative spray was studied by simultaneous imaging of the liquid and vapor phases in high temperature and high density conditions, through two separate optical setups synchronized to capture the same injection event. Finally, the reactive spray was analyzed by imaging the vapor phase in high temperature and high density conditions, while also imaging OH* chemiluminescence.

Overall, the cylindrical nozzle *k0* showed strong signs of cavitation in the hydraulic analysis. This effect carries on to the spray development, as was observed in all spray visualizations, where the cylindrical nozzle consistently showed larger spreading angles and stronger fluctuations in the line-of-sight spray contour. Larger spreading angles also imply faster momentum exchange, which renders slower spray tip penetration rates and shorter liquid penetration length, in the case of evaporative sprays. For reactive sprays, larger spray spreading angles also imply shorter lift-off lengths, because of the slower tip penetration rate.

An interesting behavior was observed in the spray visualizations, regarding fuel properties. Isothermal liquid spray visualization showed a strong influence of fuel properties in the spray tip penetration, such as surface tension and viscosity. n-Heptane, which features the lowest density, viscosity and surface tension, produces sprays which consistently penetrate slower than the Surrogate sprays. This effect, however, was not observed in the vapor spray visualization results, which is expected since once fuel is vaporized the spray is mainly driven by momentum. It has been long known that for equivalent densities, isothermal liquid sprays penetrate faster than vapor sprays, but these results also account for fuel properties and this finding is thought to be important for model validations.

Two empirical predictive models were presented and utilized to analyze the influence of fuel properties on the liquid length. The primary factor controlling the liquid length between the fuels of interest was found to be their volatility.

Note that this is not the case to be expected with ethanol, methanol or fuels with a large latent heat of vaporization.

The n-heptane spray featured the shortest liquid lengths and the longest ignition delays (thus, lift-off lengths). The Surrogate spray, on the other hand, featured the longest liquid lengths and considerably shorter ignition delays—n-dodecane sprays featured even shorter ignition delays. This means that the combustions produced by each of these spray are very different, which is crucial for pollutant formation, for example, as expected from the current literature on the relationships between liquid and lift-off lengths, and soot formation.

Another particular behavior was observed for the reactive sprays. The conical nozzle *k15* featured shorter ignition delays when compared to the cylindrical nozzle. This was unexpected at first, but could be related to the narrower spreading angle, which could imply a richer mixture fraction when fuel break-up and mixing have reached an ignitable point. This behavior, even though subtle, was found to be fairly consistent along the large database gathered. Nevertheless, further analysis for a more in-depth understanding of the mechanics involved in this process should be definitely considered.

Recent published models that comprise the full integration of the nozzle geometry internal flow and spray development, along with upcoming developed and expanded versions of these, could be crucial for understanding the mechanisms involved and the whole problem of high injection pressure reactive sprays. But proper validation of these models is necessary. The large database gathered in this work is available online (`http://www.cmt.upv.es/DD01.aspx`) for the community, so that models are validated including the effects of fuels, cavitation, and a large span of different injection conditions.

7.2 Future direction

Even though this database is large, it is by no means complete. Spray development is very complex, comprising a large group of phenomena and processes that take place in a single, very fast event. The diagnostics performed here are just a first step for establishing a large database that contains more information of the complete injection process. A few examples of additional experiments that could certainly enhance the quality of the database are

- A larger number of test repetitions or a longer injection event. These should be considered in case further measurements are done with the purpose of obtaining contour fluctuation maps similar to those presented in this study. Contour fluctuation maps for both the isothermal and liquid phase sprays presented in this work are very diffuse and smooth since they were constructed from a very large set of images, because of the length of the time-window considered and the very high acquisition rate. However, vapor phase fluctuation maps could be improved by either increasing the number of test repetitions or the time-window, which is a function of the total injection time.

- Microscopic visualization of the near-nozzle region for the isothermal liquid sprays. These type of experiments have been performed several times by different researchers with various purposes. Performing these for the same nozzles and fuels, at the same injection conditions could further support the findings of this work, and would be essential for model calibration in the near-field region.

- Microscopic visualization of the near-nozzle region for evaporative sprays. A similar point to the previous mentioned, but this time in a evaporative environment. This has proven to be a challenge because of beam steering and other effects that decrease image quality, but it can still provide valuable information regarding cavitation and fuels.

- Considering other fuels. During the process of these experiments, optical setups and especially image processing algorithms were optimized significantly. This considerably increased the capacity of the research group to perform similar experiments, which is always simpler than developing or implementing a new technique. Performing the same experiments for a new fuel—maybe also repeating a fuel for reference—could bring more useful findings that further support those found in this work.

- Soot measurements of these sprays, considering all nozzles and fuels. As said in the previous section, the experimental test matrix combined with the different fuels produced a large span of very different types of combustion regimes. All macroscopic variables such as liquid length and lift-off length could then be related to soot formation for analysis but also model validation. In particular, the Surrogate fuel is of interest, since it is conceptualized to better mimic the soot-related behavior of real diesel fuel, as its PAH content should increase soot formation in comparison to pure n-alkanes. However, it is also possible that the SSI delay induced by the α-methylnaphthalene content is large enough so to delay ignition to a point where the local equivalence ratio is very low, which would render a less-sooting flame: a similar situation what was found for the secondary fuel of the ECN, which is a mixture of n-dodecane and m-xylene.

- Recently, very high resolution tomographies of the internal nozzle geometry have been achieved and published. These are produced by capturing several high energy synchrotron X-ray images of the nozzle at different angles (with respect to the main axis of the injector). A thresholding and reconstruction algorithm produces a surface which can be used for geometry analysis of the internals of the nozzle, but can also be directly applied to CFD meshes. Currently, similar x-ray tomographies of these nozzles, performed at the Advanced Photon Source synchrotron at Argonne National Laboratory (United States), are being processed for further detail on the real nozzle geometries.

Bibliography

ANDRIOTIS, A. and GAVAISES, M. “Influence of vortex flow and cavitation on near-nozzle diesel spray dispersion angle”. *Atomization and Sprays* 19.3 (2009), pp. 247–261.

ARGUEYROLLES, B., DEHOUX, S., GASTALDI, P., GROSJEAN, L., LEVY, F., MICHEL, A., and PASSEREL, D. “Influence of injector nozzle design and cavitation on coking phenomenon”. *SAE Technical Paper 2007-01-1896* (2007).

BADOCK, C., WIRTH, R., and TROPEA, C. “The influence of hydro grinding on cavitation inside a diesel injection nozzle and primary break-up under unsteady pressure conditions”. *Proc. 15th ILASS-Europe 99, Toulouse, July 5-7*. Toulouse (France), 1999.

BARDI, M. “Partial needle lift and injection rate shape effect on the formation and combustion of the Diesel spray”. PhD thesis. Valencia (Spain): Universitat Politècnica de València, Apr. 2014.

BARDI, M., PAYRI, R., MALBEC, L. M., BRUNEAUX, G., PICKETT, L. M., MANIN, J., BAZYN, T., and GENZALE, C. L. “Engine Combustion Network: Comparison of Spray Development, Vaporization, and Combustion in Different Combustion Vessels”. *Atomization and Sprays* 22.10 (2012), pp. 807–842.

BATTIN-LECLERC, F. “Detailed chemical kinetic models for the low-temperature combustion of hydrocarbons with application to gasoline and diesel fuel surrogates”. *Progress in Energy and Combustion Science* 34 (2008), pp. 440–498.

BATTISTONI, M., GRIMALDI, C., and MARIANI, F. “Coupled Simulation of Nozzle Flow and Spray Formation Using Diesel and Biodiesel for CI Engine Applications”. *SAE Technical Paper 2012-01-1267* (2012).

BATTISTONI, M., XUE, Q., SOM, S., and POMRANING, E. “Effect of Off-Axis Needle Motion on Internal Nozzle and Near Exit Flow in a Multi-Hole Diesel Injector”. *SAE International Journal of Fuels and Lubricants* 7.1 (Apr. 2014), pp. 2014–01–1426.

BENAJES, J., PAYRI, R., BARDI, M., and MARTÍ-ALDARAVÍ, P. “Experimental characterization of diesel ignition and lift-off length using a single-hole ECN injector”. *Applied Thermal Engineering* 58.1-2 (2013), pp. 554–563.

BENAJES, J., SALVADOR, F. J., CARRERES, M., and JARAMILLO, D. “On the relation between the external structure and the internal characteristics in the near-nozzle field of diesel sprays”. *Proceedings of the Institution of Mechanical Engineers, Part D: Journal of Automobile Engineering* (2016).

BLESSING, M., KÖNIG, G., KRÜGER, C., MICHELS, U., and SCHWARZ, V. “Analysis of flow and cavitation phenomena in diesel injection nozzles and its effects on spray and mixture formation”. *SAE Technical Paper 2003-01-1358* (2003).

BOUDY, F. and SEERS, P. “Impact of physical properties of biodiesel on the injection process in a common-rail direct injection system”. *Energy Conversion and Management* 50.12 (2009), pp. 2905–2912.

BRULATOUT, J., GARNIER, F., MOUNAI M-ROUSSELLE, C., and SEERS, P. “Calibration strategy of diesel-fuel spray atomization models using a design of experiment method”. *International Journal of Engine Research* 17.7 (Sept. 2016), pp. 713–731.

CHEN, P.-C., WANG, W.-C., ROBERTS, W. L., and FANG, T. “Spray and atomization of diesel fuel and its alternatives from a single-hole injector using a common rail fuel injection system”. *Fuel* 103 (2013), pp. 850–861.

CRUA, C., HEIKAL, M. R., and GOLD, M. R. “Microscopic imaging of the initial stage of diesel spray formation”. *Fuel* 157 (2015), pp. 140–150.

CURRAN, H., GAFFURI, P., PITZ, W. J., and WESTBROOK, C. “A Comprehensive Modeling Study of n-Heptane Oxidation”. *Combustion and Flame* 114.1-2 (1998), pp. 149–177.

DELACOURT, E., DESMET, B., and BESSON, B. “Characterisation of very high pressure Diesel sprays using digital imaging techniques”. *Fuel* 84.7-8 (2005), pp. 859–867.

DERNOTTE, J., HESPEL, C., FOUCHER, F., HOUILLÉ, S., and MOUNAÏM-ROUSSELLE, C. “Influence of physical fuel properties on the injection rate in a Diesel injector”. *Fuel* 96 (2012), pp. 153–160.

DERNOTTE, J., HESPEL, C., HOUILLE, S., FOUCHER, F., and MOUNAÏM-ROUSSELLE, C. “Influence of Fuel Properties on the Diesel Injection Process in Nonvaporizing Conditions”. *Atomization and Sprays* 22.6 (2012), pp. 461–492.

DESANTES, J. M., BERMÚDEZ, V., LÓPEZ, J. J., and LÓPEZ-PINTOR, D. “Experimental validation of an alternative method to predict high and low-temperature ignition delays under transient thermodynamic conditions for PRF mixtures using a Rapid Compression-Expansion Machine”. *Energy Conversion and Management* 129 (Dec. 2016), pp. 23–33.

DESANTES, J. M. J. M., PAYRI, R., GIMENO, J., and MARTÍ-ALDARAVÍ, P. “Simulation of the First Millimeters of the Diesel Spray by an Eulerian Spray Atomization Model Applied on ECN Spray A Injector”. *SAE Technical Paper 2014-01-1418* (Apr. 2014).

DESANTES, J. M., GARCÍA-OLIVER, J. M., PASTOR, J. M., and RAMIREZ-HERNANDEZ, J. G. “Influence of nozzle geometry on ignition and combustion for high-speed direct injection diesel engines under cold start conditions”. *Fuel* 90.11 (2011), pp. 3359–3368.

DESANTES, J. M., PAYRI, R., GARCIA, A., and MANIN, J. “Experimental Study of Biodiesel Blends’ Effects on Diesel Injection Processes”. *Energy & Fuels* 23.6 (2009), pp. 3227–3235.

DESANTES, J. M., PAYRI, R., SALVADOR, F. J., and DE LA MORENA, J. “Influence of cavitation phenomenon on primary break-up and spray behavior at stationary conditions”. *Fuel* 89.10 (2010), pp. 3033–3041.

DESANTES, J. M., PAYRI, R., SALVADOR, F. J., and GIL, A. “Development and validation of a theoretical model for diesel spray penetration”. *Fuel* 85.7-8 (2006), pp. 910–917.

DESANTES, J. M., PAYRI, R., SALVADOR, F. J., and SOARE, V. “Study of the influence of geometrical and injection parameters on Diesel Sprays characteristics in isothermal conditions”. *SAE Technical Paper 2005-01-0913* (2005).

DESANTES, J. M. et al. “Coupled/decoupled spray simulation comparison of the ECN spray a condition with the Σ-Y Eulerian atomization model”. *International Journal of Multiphase Flow* 80 (2016), pp. 89–99.

DING, H., WANG, Z., LI, Y., XU, H., and ZUO, C. “Initial dynamic development of fuel spray analyzed by ultra high speed imaging”. *Fuel* 169 (2016), pp. 99–110.

DIWAKAR, R. and SINGH, S. “NOx and soot reduction in diesel engine premixed charge compression ignition combustion: a computational investigation”. *International Journal of Engine Research* 9.3 (2008), pp. 195–214.

Fansler, T. D. and Parrish, S. E. "Spray measurement technology: a review". *Measurement Science and Technology* 26.1 (Jan. 2015), p. 012002.

Farrell, J. T., Cernansky, N. P., Dryer, F. L., Law, C. K., Friend, D. G., Hergart, C. A., McDavid, R. M., Patel, A. K., Mueller, C. J., and Pitsch, H. "Development of an Experimental Database and Kinetic Models for Surrogate Diesel Fuels". *SAE Technical Paper 2007-01-0201* (Apr. 2007).

Ganippa, L. C., Andersson, S., Chomiak, J., and Matsson, A. "Combustion characteristics of diesel sprays from equivalent nozzles with sharp and rounded inlet geometries". *Combustion Science and Technology* 175.6 (2003), pp. 1015–1032.

Han, J.-s., Lu, P.-h., Xie, X.-b., Lai, M.-c., and Henein, N. A. "Investigation of Diesel Spray Primary Break-up and Development for Different Nozzle Geometries". *SAE Technical Paper* 2002-01-27 (2002).

He, Z., Guo, G., Tao, X., Zhong, W., Leng, X., and Wang, Q. "Study of the effect of nozzle hole shape on internal flow and spray characteristics". *International Communications in Heat and Mass Transfer* 71 (2016), pp. 1–8.

Herfatmanesh, M. R., Lu, P., Attar, M. A., and Zhao, H. "Experimental investigation into the effects of two-stage injection on fuel injection quantity, combustion and emissions in a high-speed optical common rail diesel engine". *Fuel* 109 (2013), pp. 1–11.

Higgins, B. S., Mueller, C. J., and Siebers, D. L. "Measurements of fuel effects on liquid-phase penetration in DI sprays". *SAE transactions* 108.724 (1999), pp. 630–643.

Higgins, B. and Siebers, D. L. "Measurement of the Flame Lift-Off Location on DI Diesel Sprays Using OH Chemiluminescence". *SAE Paper 2001-01-0918* (2001).

Higgins, B., Siebers, D. L., and Aradi, A. "Diesel-Spray Ignition and Premixed-Burn Behavior". *SAE Technical Paper 2000-01-0940* 724 (2000).

Huang, S., Deng, P., Huang, R., Wang, Z., Ma, Y., and Dai, H. "Visualization research on spray atomization, evaporation and combustion processes of ethanol-diesel blend under LTC conditions". *Energy Conversion and Management* 106 (2015), pp. 911–920.

Idicheria, C. A. and Diwakar, R. "Design of an optimum combustion chamber across multiple speed/load points for a heavy-duty diesel engine: analytical design and experimental validation". *International Journal of Engine Research* 12.2 (2011), pp. 123–143.

IDICHERIA, C. A. and PICKETT, L. M. “Soot formation in Diesel combustion under high-EGR conditions”. *SAE Technical Paper 2005-01-3834* (2005).

JERZEMBECK, S., PETERS, N., PEPIOTDESJARDINS, P., and PITSCH, H. “Laminar burning velocities at high pressure for primary reference fuels and gasoline: Experimental and numerical investigation”. *Combustion and Flame* 156.2 (Feb. 2009), pp. 292–301.

JIANG, G., ZHANG, Y., WEN, H., and XIAO, G. “Study of the generated density of cavitation inside diesel nozzle using different fuels and nozzles”. *Energy Conversion and Management* 103 (2015), pp. 208–217.

JOHNSON, J., GE, H.-W., NABER, J., LEE, S.-Y., KURTZ, E., and ROBARGE, N. “Investigation of Key Mechanisms for Liquid Length Fluctuations in Transient Vaporizing Diesel Sprays”. *SAE Technical Paper 2013-01-1594* (2013), pp. 1202–1212.

JUNG, Y., MANIN, J., SKEEN, S. A., and PICKETT, L. M. “Measurement of Liquid and Vapor Penetration of Diesel Sprays with a Variation in Spreading Angle”. *SAE Technical Paper 2015-01-0946* (2015).

KONG, J. and BAE, C. “Effect of a conical nozzle orifice on the combustion and emissions in a direct- injection compression ignition engine under low-load conditions”. *Proceedings of the Institution of Mechanical Engineers, Part D: Journal of Automobile Engineering* 229.1 (Jan. 2015), pp. 3–13.

KOO, J. Y., HONG, S. T., SHAKAL, J. S., and GOTO, S. “Influence of fuel injector nozzle geometry on internal and external flow characteristics”. *SAE Technical Paper 970354* (1997).

KOOK, S. and PICKETT, L. M. “Liquid length and vapor penetration of conventional , Fischer-Tropsch , coal-derived , and surrogate fuel sprays at high-temperature and high-pressure ambient conditions”. *Fuel* 93 (2012), pp. 539–548.

LEMMON, E. W., MCLINDEN, M. O., and FRIEND, D. G. “Thermophysical Properties of Fluid Systems”. *NIST Chemistry WebBook, NIST Standard Reference Database Number 69*. Ed. by P. J. LINSTROM and W. G. MALLARD. 2011.

LEQUIEN, G., SKEEN, S., MANIN, J., PICKETT, L. M., and ANDERSSON, O. “Ignition Quality Effects on Lift-Off Stabilization of Synthetic Fuels”. *SAE International Journal of Engines* 8.2 (Apr. 2015), pp. 2015–01–0792.

LIU, Z., IM, K.-S., WANG, Y., FEZZAA, K., WANG, J., XIE, X.-B., and LAI, M.-C. “Near-Nozzle Structure of Diesel Sprays Affected by Internal Geometry of Injector Nozzle: Visualized by Single-Shot X-ray Imaging”. *SAE Technical Paper 2010-01-0877* (2010).

LUCKHCHOURA, V., PETERS, N., and DIWAKAR, R. “Computational analysis of injection-rate shapes in a small-bore direct-injection diesel engine”. *International Journal of Engine Research* 12.2 (2011), pp. 145–168.

LUO, J., YAO, M., LIU, H., and YANG, B. “Experimental and numerical study on suitable diesel fuel surrogates in low temperature combustion conditions”. *Fuel* 97 (2012), pp. 621–629.

MAGNO, A., MANCARUSO, E., and VAGLIECO, B. M. “Experimental investigation in an optically accessible diesel engine of a fouled piezoelectric injector”. *Energy* 64 (2014), pp. 842–852.

MANIN, J., BARDI, M., and PICKETT, L. M. “Evaluation of the liquid length via diffused back-illumination imaging in vaporizing diesel sprays”. *Comodia*. Fukuoka, 2012.

MEIJER, M. et al. “Engine Combustion Network (ECN): Characterization and comparison of boundary conditions for different combustion vessels”. *Atomization and Sprays* 22.9 (2012), pp. 777–806.

METGHALCHI, M. and KECK, J. C. “Burning velocities of mixtures of air with methanol, isooctane, and indolene at high pressure and temperature”. *Combustion and Flame* 48 (Jan. 1982), pp. 191–210.

MOHAN, B., YANG, W., TAY, K. L., and YU, W. “Experimental study of spray characteristics of biodiesel derived from waste cooking oil”. *Energy Conversion and Management* 88 (2014), pp. 622–632.

MOHAN, B., YANG, W., TAY, K. L., and YU, W. “Macroscopic spray characterization under high ambient density conditions”. *Experimental Thermal and Fluid Science* 59 (2014), pp. 109–117.

MONTANARO, A., MIGLIACCIO, M., ALLOCCA, L., FRAIOLI, V., LEE, S.-Y., ZHANG, A., and NABER, J. “Schlieren and Mie Scattering Visualization for Single- Hole Diesel Injector under Vaporizing Conditions with Numerical Validation”. *SAE Technical Paper 2014-01-1406* 2014-01-14 (2014).

MORGAN, R., WRAY, J., KENNAIRD, D. A., CRUA, C., and HEIKAL, M. R. “The Influence of Injector Parameters on the Formation and break-Up of a Diesel Spray”. *SAE Technical Paper 2001-01-0529* (2001).

NABER, J. D. and SIEBERS, D. L. “Effects of Gas Density and Vaporization on Penetration and Dispersion of Diesel Sprays”. *SAE Paper 960034*. Vol. 105. 412. Society of Automotive Engineers, Inc., Warrendale, Pennsylvania, USA, Feb. 1996, pp. 82–111.

NATELSON, R. H., KURMAN, M. S., CERNANSKY, N. P., and MILLER, D. L. “Experimental investigation of surrogates for jet and diesel fuels”. *Fuel* 87 (2008), pp. 2339–2342.

NING, W., REITZ, R. D., DIWAKAR, R., and LIPPERT, A. M. “An eulerian-lagrangian spray and atomization model with improved turbulence modeling”. *Atomization and Sprays* 19.8 (2009), pp. 727–739.

NING, W., REITZ, R. D., DIWAKAR, R., and LIPPERT, A. M. “A Numerical Investigation of Nozzle Geometry and Injection Condition Effects on Diesel Fuel Injector Flow Physics”. *SAE Technical Paper 2008-01-0936* (2008).

PARK, Y., HWANG, J., BAE, C., KIM, K., LEE, J., and PYO, S. “Effects of diesel fuel temperature on fuel flow and spray characteristics”. *Fuel* 162 (2015), pp. 1–7.

PASTOR, J. V., GARCIA-OLIVER, J. M., LOPEZ, J. J., and VERA-TUDELA, W. “An experimental study of the effects of fuel properties on reactive spray evolution using Primary Reference Fuels”. *Fuel* 163.X (2016), pp. 260–270.

PAYRI, F., BERMÚDEZ, V., PAYRI, R., and SALVADOR, F. J. “The influence of cavitation on the internal flow and the spray characteristics in diesel injection nozzles”. *Fuel* 83.4-5 (2004), pp. 419–431.

PAYRI, R., GARCÍA-OLIVER, J. M., BARDI, M., MANIN, J., GARCIA-OLIVER, J. M., BARDI, M., and MANIN, J. “Fuel temperature influence on diesel sprays in inert and reacting conditions”. *Applied Thermal Engineering* 35.March (Mar. 2012), pp. 185–195.

PAYRI, R., GARCIA-OLIVER, J. M., SALVADOR, F. J., and GIMENO, J. “Using spray momentum flux measurements to understand the influence of diesel nozzle geometry on spray characteristics”. *Fuel* 84.5 (2005), pp. 551–561.

PAYRI, R., GIMENO, J., BRACHO, G., and VAQUERIZO, D. “Study of liquid and vapor phase behavior on Diesel sprays for heavy duty engine nozzles”. *Applied Thermal Engineering* 107 (2016), pp. 365–378.

PAYRI, R., GIMENO, J., VIERA, J. P., and PLAZAS, A. H. “Schlieren visualization of transient vapor penetration and spreading angle of a prototype diesel direct-acting piezoelectric injector”. *ICLASS 2012*. 2012, pp. 1–8.

PAYRI, R., GIMENO, J., VIERA, J. P., and PLAZAS, A. H. “Needle lift profile influence on the vapor phase penetration for a prototype diesel direct acting piezoelectric injector”. *Fuel* 113 (2013), pp. 257–265.

PAYRI, R., MOLINA, S., SALVADOR, F. J., and GIMENO, J. “A study of the relation between nozzle geometry, internal flow and sprays characteristics in diesel fuel injection systems”. *KSME International Journal* 18.7 (2004), pp. 1222–1235.

PAYRI, R., SALVADOR, F. J., CARRERES, M., and DE LA MORENA, J. "Fuel temperature influence on the performance of a last generation common-rail diesel ballistic injector. Part II: 1D model development, validation and analysis". *Energy Conversion and Management* 114 (Apr. 2016), pp. 376–391.

PAYRI, R., SALVADOR, F. J., GIMENO, J., and BRACHO, G. "A new methodology for correcting the signal cumulative phenomenon on injection rate measurements". *Experimental Techniques* 32.February (2008), pp. 46–49.

PAYRI, R., SALVADOR, F. J., GIMENO, J., and DE LA MORENA, J. "Effects of nozzle geometry on direct injection diesel engine combustion process". *Applied Thermal Engineering* 29.10 (2009), pp. 2051–2060.

PAYRI, R., SALVADOR, F. J., GIMENO, J., and DE LA MORENA, J. "Analysis of Diesel spray atomization by means of a near-nozzle field visualization technique". *Atomization and Sprays* 21.9 (2011), pp. 753–774.

PAYRI, R., SALVADOR, F. J., GIMENO, J., and GARCIA, A. "Flow regime effects over non-cavitating Diesel injection nozzles". *Journal of Automobile Engineering* 226 (2011), pp. 133–144.

PAYRI, R., SALVADOR, F. J., GIMENO, J., and VENEGAS, O. "Study of cavitation phenomenon using different fuels in a transparent nozzle by hydraulic characterization and visualization". *Experimental Thermal and Fluid Science* 44 (2013), pp. 235–244.

PAYRI, R., SALVADOR, F. J., GIMENO, J., and VIERA, J. P. "Experimental analysis on the influence of nozzle geometry over the dispersion of liquid n-dodecane sprays". *Frontiers in Mechanical Engineering* 1 (2015), pp. 1–10.

PAYRI, R., SALVADOR, F. J., GIMENO, J., and ZAPATA, L. D. "Diesel nozzle geometry influence on spray liquid-phase fuel penetration in evaporative conditions". *Fuel* 87.7 (2008), pp. 1165–1176.

PAYRI, R., SALVADOR, F. J., MANIN, J., and VIERA, A. "Diesel ignition delay and lift-off length through different methodologies using a multi-hole injector". *Applied Energy* 162 (2016), pp. 541–550.

PAYRI, R., VIERA, J. P., GOPALAKRISHNAN, V., and SZYMKOWICZ, P. G. "The effect of nozzle geometry over the evaporative spray formation for three different fuels". *Fuel* 188 (2017), pp. 645–660.

PAYRI, R., VIERA, J. P., GOPALAKRISHNAN, V., and SZYMKOWICZ, P. G. "The effect of nozzle geometry over internal flow and spray formation for three different fuels". *Fuel* 183 (Nov. 2016), pp. 20–33.

PAYRI, R., VIERA, J. P., GOPALAKRISHNAN, V., and SZYMKOWICZ, P. G. “The effect of nozzle geometry over ignition delay and flame lift-off of reacting direct-injection sprays for three different fuels”. *Fuel* 199 (2017), pp. 76–90.

PAYRI, R., VIERA, J. P., PEI, Y., and SOM, S. “Experimental and numerical study of lift-off length and ignition delay of a two-component diesel surrogate”. *Fuel* 158 (2015), pp. 957–967.

PEI, Y., MEHL, M., LIU, W., LU, T., PITZ, W. J., and SOM, S. “A Multicomponent Blend as a Diesel Fuel Surrogate for Compression Ignition Engine Applications”. *Journal of Engineering for Gas Turbines and Power* 137.11 (May 2015), p. 111502.

PICKETT, L. M., GENZALE, C. L., and MANIN, J. “Uncertainty quantification for liquid penetration of evaporating sprays at diesel-like conditions”. *Atomization and Sprays* 25.5 (2015), pp. 425–452.

PICKETT, L. M., GENZALE, C. L., MANIN, J., MALBEC, L.-M., and HERMANT, L. “Measurement Uncertainty of Liquid Penetration in Evaporating Diesel Sprays”. *ILASS Americas, 23rd Annual Conference on Liquid Atomization and Spray Systems*. May. Ventura, CA (USA): ILASS-Americas, 2011.

PICKETT, L. M., MANIN, J., GENZALE, C. L., SIEBERS, D. L., MUSCULUS, M. P. B., and IDICHERIA, C. A. “Relationship Between Diesel Fuel Spray Vapor Penetration/Dispersion and Local Fuel Mixture Fraction”. *SAE International Journal of Engines* 4.1 (2011), pp. 764–799.

PICKETT, L. M., MANIN, J., PAYRI, R., BARDI, M., and GIMENO, J. “Transient Rate of Injection Effects on Spray Development”. *SAE Technical Paper 2013-24-0001* (2013).

PICKETT, L. M., SIEBERS, D. L., and IDICHERIA, C. A. “Relationship Between Ignition Processes and the Lift-Off Length of Diesel Fuel Jets”. *SAE Paper 2005-01-3843* 724 (2005).

PITSCH, H., BARTHS, H., and PETERS, N. “Three-dimensional Modeling of NOx and soot formation in DI-diesel engines using detailed chemistry based on the interactive flamelet approach”. *SAE Technical Paper 962057* (1996).

PITZ, W. J. and MUELLER, C. J. “Recent progress in the development of diesel surrogate fuels”. *Progress in Energy and Combustion Science* 37.3 (2011), pp. 330–350.

QIU, T., SONG, X., LEI, Y., DAI, H., CAO, C., XU, H., and FENG, X. “Effect of back pressure on nozzle inner flow in fuel injector”. *Fuel* 173 (2016), pp. 79–89.

RAJU, M., WANG, M., SENECAL, P. K., SOM, S., and LONGMAN, D. E. “A reduced diesel surrogate mechanism for compression ignition engine applications”. *Proceedings of the ASME 2012 Internal Combustion Engine Division Fall Technical Conference ICEF2012*. Vancouver: American Society of Mechanical Engineers, 2012.

REDDEMANN, M. A., MATHIEU, F., MARTIN, D., and KNEER, R. “The Influence of Fuel Properties on Spray Propagation , Atomization and Evaporation”. *ILASS 2010*. September. 2010, pp. 1–6.

REYES, M., TINAUT, F. V., ANDRÉS, C., and PÉREZ, A. “A method to determine ignition delay times for Diesel surrogate fuels from combustion in a constant volume bomb: Inverse Livengood-Wu method”. *Fuel* 102 (2012), pp. 289–298.

SALVADOR, F. J., GIMENO, J., PASTOR, J. M., and MARTÍ-ALDARAVÍ, P. “Effect of turbulence model and inlet boundary condition on the diesel spray behavior simulated by an eulerian spray atomization (ESA) model”. *International Journal of Multiphase Flow* 65 (2014), pp. 108–116.

SALVADOR, F. J., PLAZAS, A. H., GIMENO, J., and CARRERES, M. “Complete modelling of a piezo actuator last-generation injector for diesel injection systems”. *International Journal of Engine Research* 15.1 (Jan. 2014), pp. 3–19.

SIEBERS, D. L. “Liquid-phase fuel penetration in diesel sprays”. *SAE Paper 980809* (1998).

SIEBERS, D. L. “Scaling liquid-phase fuel penetration in diesel sprays based on mixing-limited vaporization”. *SAE Technical Paper 1999-01-0528* (1999).

SOM, S., AGGARWAL, S. K., EL-HANNOUNY, E. M., and LONGMAN, D. E. “Investigation of nozzle flow and cavitation characteristics in a diesel injector”. *Journal of Engineering for Gas Turbines and Power* 132.4 (2010), p. 042802.

SOM, S. and AGGARWAL, S. K. “Modeling Diesel Spray Flame Lift-off using Detailed Chemistry and a New Primary Breakup Model”. *47th AIAA Aerospace Sciences Meeting including The New Horizons Forum and Aerospace Exposition*. 2009, pp. 1–14.

SOM, S. and AGGARWAL, S. K. “Effects of primary breakup modeling on spray and combustion characteristics of compression ignition engines”. *Combustion and Flame* 157.6 (2010), pp. 1179–1193.

SOM, S., RAMÍREZ, A. I., AGGARWAL, S., KASTENGREN, A. L., EL-HANNOUNY, E., LONGMAN, D. E., POWELL, C. F., and SENECAL, P. K. “Development and validation of a primary breakup model for diesel engine applications”. *SAE Technical Paper 2009-01-0838* (2009).

SOM, S., RAMÍREZ, A. I., LONGMAN, D. E., and AGGARWAL, S. K. “Effect of nozzle orifice geometry on spray, combustion, and emission characteristics under diesel engine conditions”. *Fuel* 90.3 (2011), pp. 1267–1276.

STUMPP, G. and RICCO, M. “Common Rail - An attractive fuel injection system for passenger car DI Diesel engines”. *SAE Technical Paper 960870* (1996).

SUH, H. K. and LEE, C. S. “Effect of cavitation in nozzle orifice on the Diesel fuel atomization characteristics”. *International Journal of Heat and Fluid Flow* 29.4 (2008), pp. 1001–1009.

SUN, Z.-Y., LI, G.-X., CHEN, C., YU, Y.-S., and GAO, G.-X. “Numerical investigation on effects of nozzle’s geometric parameters on the flow and the cavitation characteristics within injector’s nozzle for a high-pressure common-rail DI diesel engine”. *Energy Conversion and Management* 89 (2015), pp. 843–861.

TANG, J., PISCHINGER, S., LAMPING, M., KÖRFER, T., TATUR, M., and TOMAZIC, D. “Coking Phenomena in Nozzle Orifices of Dl-Diesel Engines”. *SAE International Journal of Fuels and Lubricants* 2.1 (Apr. 2009), pp. 2009–01–0837.

TINAUT, F. V., GIMÉNEZ, B., IGLESIAS HOYOS, D., and LAWES, M. “Experimental determination of the burning velocity of mixtures of n-heptane and toluene in engine-like conditions”. *Flow, Turbulence and Combustion* 89.2 (2012), pp. 183–213.

WANG, Y., QIU, L., REITZ, R. D., and DIWAKAR, R. “Simulating cavitating liquid jets using a compressible and equilibrium two-phase flow solver”. *International Journal of Multiphase Flow* 63 (2014), pp. 52–67.

XUE, Q., BATTISTONI, M., POWELL, C. F., LONGMAN, D. E., QUAN, S., POMRANING, E., SENECAL, P. K., SCHMIDT, D. P., and SOM, S. “An Eulerian CFD model and X-ray radiography for coupled nozzle flow and spray in internal combustion engines”. *International Journal of Multiphase Flow* 70 (2015), pp. 77–88.

XUE, Q., SOM, S., BATTISTONI, M., QUAN, S., SENECAL, P. K., POMRANING, E., and SCHMIDT, D. P. “Eulerian CFD Modeling of Coupled Nozzle Flow and Spray with Validation Against X-Ray Radiography Data”. *Int. J. of Engines* 7.2 (2014), pp. 1061–1072.

YAO, C., GENG, P., YIN, Z., HU, J., CHEN, D., and JU, Y. “Impacts of nozzle geometry on spray combustion of high pressure common rail injectors in a constant volume combustion chamber”. *Fuel* 179 (Sept. 2016), pp. 235–245.

ZHANG, A., MONTANARO, A., ALLOCCA, L., NABER, J., and LEE, S.-Y. “Measurement of Diesel Spray Formation and Combustion upon Different Nozzle Geometry using Hybrid Imaging Technique”. *SAE Technical Paper 2014-01-1410* (2014).